

SIGNIFICANCE OF MECHANICAL BEHAVIOR AND STRESS  
HETEROGENEITY IN A DEEP GEOTHERMAL RESERVOIR

Zur Erlangung des akademischen Grades eines  
DOKTORS DER NATURWISSENSCHAFTEN

von der Fakultät

Bauingenieur-, Geo- und Umweltwissenschaften

des Karlsruher Instituts für Technologie (KIT)

genehmigte

DISSERTATION

von

David Prambudi Sahara, M.Sc.

aus Trenggalek, Indonesien

Tag der mündlichen

Prüfung: 3 Juni 2016

Referent: Prof. Dr. Thomas Kohl

Korreferent: Prof. Dr. Friedemann Wenzel

Karlsruhe 2016



This document is licensed under the Creative Commons Attribution 3.0 DE License (CC BY 3.0 DE): <http://creativecommons.org/licenses/by/3.0/de/>

# Abstract

The International Energy Agency predicts geothermal deliver about 3.5% of the total electricity production by 2050 [IEA, 2013]. It can be realized by capitalizing the large potency of the Enhanced Geothermal System (EGS). To achieve this goal, it is important to accelerate our ability to ensure the stability of wellbore and to engineer a volume of rock consisting of a network of fractures that provides sufficient fluid flow pathways. Such an effort must rely on rock mechanics principles conditioned to geothermal settings. Therefore, rock mechanics study constitutes an integral part of a comprehensive approach to geothermal reservoir characterization and development.

The goal of this thesis is an improved quality of the characterization of the mechanical and stress distribution of the deep crystalline reservoir in Soultz-sous-Forêts (France). One of the most important applications of in-situ stress characterization in geo-reservoirs is associated with wellbore instability. Current investigations of stress magnitude are based on various methods including hydraulic fracturing, borehole breakouts, drilling-induced tensile fractures (DITF), focal mechanism inversion and others. Particularly, existing borehole breakout assessments in Soultz were revised, and the mechanisms of breakouts were studied further. The background on the importance of rock mechanics for reservoir engineering is presented in a special chapter. This thesis consists of four principal studies, i.e. mechanical properties, in-situ stress field, hydraulic stimulation and numerical modeling.

I infer the impact of fracture networks on the development of wellbore failures from a detailed analysis of 1221 and 887 compressional and tensional failure pairs, respectively, in the vicinity of 1871 natural fractures observed in the crystalline section of the GPK4 well. It is found that the orientation of breakouts is strongly influenced by the fracture orientation; a direct relationship between fracture and breakout orientations is found and, in a zone with several fracture families occurred, breakout orientations are especially heterogeneous. Subsequently, I show the first and second order of breakout orientation heterogeneities which correspond to the stress-related and fracture-related breakouts, respectively. The detailed analysis of breakout geometry performed in this study enables us to distinguished both type of breakouts. Using stress-related breakouts only, the regional in-situ stress field and its local heterogeneity in the vicinity of major faults is then estimated.

Neural network clustering scheme is used to identify inherent structures present in a set of geophysical log data, i.e. magnetic susceptibility, fracture, alteration, and breakout. Three zones with different rock characteristics and mechanical properties are proposed i.e. porphyritic, transition and two-mica granite. On the top of this, the slip tendency of all fractures in each zone is estimated. With the limitation of available deep core data, this integrated analysis presents a procedure for assessing mechanical properties of the deep geothermal reservoir.

Using the Young modulus, Poisson's ratio, and compressional strength distribution estimated in this study, I am able to model the distribution of the wellbore failures in

the GPK4 well. The impact of the in-situ stress on wellbore failures is less pronounced in the deviated section of the GPK4 well, i.e. the limitation of tensile failures in part of the well inclined by less than  $10^\circ$ , and the delay of compressional failures occurrence by about 700 m in a  $25^\circ$  inclined well. The significant reduction of the compressional strength in a highly fractured granite, by approximately 30%, promote the development of a cluster of wellbore failures at a shallower depth.

In a broader scale, the in-situ stress state and the mechanical heterogeneities in a crystalline rock play a key role in governing the response of the reservoir to the injection. The dynamic responses of reservoir to the increasing pore pressure during fluid injection with respect to its mechanical properties are observed, e.g. an episodic fracture reactivation from two-mica to porphyritic granite, an anti-correlation between clay content and microseismic events, a significantly higher number of microseismic events in the weaker two-mica granite and an extensive damage area in the porphyritic granite. Furthermore, the pattern of the microseismicity in each zone is also matched with the different injection scheme, suggesting that an adapted injection strategy might be developed based on the geomechanical model proposed in this study.

To gain a better insight into the wellbore failures in a complex medium, I developed a numerical modeling to model the development of breakouts in an inhomogeneous elastoplastic material. A continuum damage mechanics (CDM) concept that takes into account the tensile and compressive modes is applied. Using CDM, I am able to reproduce several characteristics of the failure processes during the breakout development as observed in experimental tests, e.g. localized crack distribution in the vicinity of the borehole wall, damage evolution which exhibits a widening process in the beginning followed by subsequent growth in depth, and shear fracturing-dominated breakout growth in sandstone. The CDM concept implemented in this simulation, furthermore, allows us to reproduce breakout geometries obtained through laboratory experiments.

I concluded that the wellbore stability problems and the dynamic behavior of the Soultz reservoir during the hydraulic stimulation are highly related to its mechanical and stress characteristic. The impact of the fracture network on mechanical properties is very pronounced in crystalline rock. Hence, we could attribute the mechanical and stress heterogeneities to the occurrence of fractures and accompanying alteration only. As most of the EGS target the crystalline rock, the finding of the lithological and petrographical controls on wellbore stability and induced seismicity in granitic rock is crucial for the future development of the EGS. The breakout numerical code allows us furthermore to perform a variation of the conditions that could not be achieved in the laboratory experiments, e.g. high temperature and pressure condition, at a greater scale comparable to the reservoir.

The database for the studies formed several geophysical logs and a catalog of induced seismicity courtesy of GEIE Heat Mining in Soultz. The PhD project was funded by the Indonesia Directorate General of Higher Education (DIKTI), the German Academic Exchange Service (DAAD), Energie Baden-Wuerttemberg (EnBW) and Helmholtz Funding Program.

# Zusammenfassung

Die International Energy Agency prognostiziert, dass im Jahre 2050 ca. 3,5% der gesamten Stromerzeugung von Geothermie gedeckt wird. Dies kann nur durch einen Ausbau des großen Potenzials von Enhanced Geothermal Systems (EGS) realisiert werden. Um dieses Ziel zu erreichen, ist es wichtig, unsere Fähigkeiten, die Bohrlochsicherheit zu gewährleisten und ein Gesteinsvolumen mit einem ausgedehnten Kluftnetzwerk zu erschließen, das genügend Fließpfade aufweist. Aus diesem Grund stellt die Felsmechanik einen integralen Bestandteil eines umfassenden Ansatzes zur Reservoircharakterisierung und Erschließung dar.

Das Ziel dieser Arbeit ist eine verbesserte Charakterisierung der Mechanik und der Spannungsverteilung des tiefen kristallinen Reservoirs in Soultz-sous-Forêts (Frankreich). Eine der wichtigsten Anwendungen von in situ Spannungs-Beschreibung in Georeservoiren ist verbunden mit Bohrlochinstabilität. Zeitgenössischen Untersuchungen der Spannungsmagnitudo liegen verschiedene Methoden zugrunde, darunter hydraulic fracturing, Bohrlochrandausbrüche, bohrungsinduzierte Zugrisse (DITF), Inversion der Herdflächenlösung und weitere. Insbesondere wurden bestehende Untersuchungen von Bohrlochrandausbrüchen in Soultz überarbeitet und die zugrundeliegenden Mechanismen wurden weiter untersucht. Der Hintergrund für die Bedeutung der Felsmechanik für das Reservoir-Engineering wird in einem separaten Kapitel beleuchtet. Diese Arbeit besteht aus vier grundlegenden Studien: mechanische Eigenschaften, in situ Spannungsfeld, hydraulische Stimulation und numerische Modellierung.

Der Einfluss von Kluftnetzwerken auf die Entstehung von Bohrlochrandausbrüchen wird auf Grundlage einer detaillierten Untersuchung von 1221 kompresseren sowie 887 Zugbrüchen in der Nähe von 1871 natürlichen Klüften im Kristallin der Bohrung GPK4 abgeleitet. Es zeigt sich ein starker Einfluss der Kluftorientierung auf die Orientierung der Bohrlochrandausbrüche. Eine große Heterogenität der Orientierung der Bohrlochrandausbrüche kann in einem Bereich mit mehreren Kluftfamilien beobachtet werden. Anschließend werde ich die Heterogenitäten erster und zweiter Ordnung der Bohrlochrandausbruchorientierungen die den spannungsabhängigen und den Kluft abhängigen Bohrlochrandausbrüchen entsprechen. Die detaillierte Analyse der Geometrie der Bohrlochrandausbrüche, die in dieser Arbeit dargestellt wird, ermöglicht eine Unterscheidung zwischen diesen beiden Arten von Bohrlochrandausbrüchen. Auf Grundlage der spannungsabhängigen Bohrlochrandausbrüche wird das regionale in situ Spannungsfeld und seine lokale Heterogenität in der Nähe von großen Kluftzonen abgeschätzt.

Mit Hilfe von Neural Network Clustering wurden inhärente Strukturen in einer Reihe von geophysikalischen Logs untersucht: magnetische Suszeptibilität, Kluftdaten, Alteration und Bohrlochrandausbrüche. Es werden drei Zonen unterschiedlicher Gesteinscharakteristika unterschieden. Das gehäufte Auftreten von Bohrlochrandausbrüchen und Klüften im Zweiglimmergranit weist auf eine

geringere Festigkeit dieses Gesteinstyps im Gegensatz zum porphyrischen Granit hin. Die Übergangzone zwischen den beiden Gesteinseinheiten ist durch einen hohen Tongehalt gekennzeichnet. Für alle Klüfte in den definierten Zonen wurde außerdem eine Slip Tendency Analyse durchgeführt. Unter der Voraussetzung einer vollständigen Datengrundlage stellt dieses integrierte Verfahren eine Möglichkeit dar, die mechanischen Eigenschaften des tiefen geothermischen Reservoirs abzuschätzen.

Unter Verwendung des Young Moduls, der Poisson Rate und der Verteilung der Druckfestigkeit, die in dieser Studie abgeschätzt wird, ist es möglich, die Verteilung von Bohrlochausbrüchen in der Bohrung GPK4 zu modellieren. Die deutliche Verringerung von ca. 30% der Druckfestigkeit in stark zerklüftetem Granit begünstigt die Bildung einer Anhäufung von Bohrlochrandausbrüchen in einer geringeren Tiefe von ca. 3000 m. Der Einfluss der in situ Spannungen auf Bohrlochausbrüche ist im abgelenkten Bohrungsabschnitt der Bohrung GPK4 geringer. Dies äußert sich in einem begrenzten Auftreten von Zugrisen in den Abschnitten die  $<10^\circ$  geneigt sind sowie in einem versetzten Auftreten von kompressiven Ausbrüchen von etwa 700 m in einer  $25^\circ$  geneigten Bohrung.

Auf größerem Maßstab spielen die in situ Spannung und die Heterogenität der mechanischen Eigenschaften eine zentrale Rolle als beeinflussende Faktoren für die Antwort des Reservoirs auf Fluidinjektion. Die dynamische Reaktion des Reservoirs auf ansteigenden Porendruck während der Fluidinjektion in Bezug auf seine mechanischen Eigenschaften werden zum Beispiel anhand einer episodischen Kluftraktivierung von Zweiglimmergranit zu porphyrischem Granit, einer Antikorrelation zwischen Tongehalt und Mikroseismizität, einem vermehrten Auftreten von Mikroseismizität im weicheren Zweiglimmergranit und in einem extensiven Schadenbereich im porphyrischen Granit beobachtet. Darüber hinaus kann das Muster der Mikroseismizität in jeder der Zonen mit den verschiedenen Injektionsschemata in Verbindung gebracht werden. Dies deutet darauf hin, dass auf dem geomechanischen Modell, das in dieser Studie entwickelt wurde, eine Injektionsstrategie entwickelt werden könnte.

Um einen besseren Einblick in Bohrlochrandausbrüche in einem komplexen Medium zu bekommen wurde im Zuge dieser Arbeit ein numerisches Modell erstellt, um die Entstehung von Breakouts in einem inhomogenen elastoplastischen Material zu modellieren. Es wird ein Konzept angewandt, das auf Kontinuumsmechanik basiert (CDM) und das die Zug- und Kompressionsmoden berücksichtigt. Mit Hilfe von CDM können mehrere Charakteristika des Versagensprozesses von Gestein während der Breakout-Bildung nachgebildet werden, wie sie auch in Laborversuchen beobachtet werden: lokalisierte Bruchverteilung in der Nähe der Bohrlochwand, Bruchentwicklung, die einen Aufweitungs-Prozess zu Beginn zeigt, sich anschließend jedoch in die Tiefe ausbreitet, und Scherbruch-dominiertes Breakout Wachstum in Sandstein. Das CDM Konzept, das in diese Simulation implementiert wurde, ermöglicht es außerdem, die Breakout Geometrien nachzubilden, die in Laborversuchen entstanden sind.

Daraus wird geschlossen, dass die Bohrlochstabilität und das dynamische Verhalten des Reservoirs in Soultz während der hydraulischen Stimulation eng mit den mechanischen und Spannungseigenschaften zusammenhängt. Der Einfluss des Klufnetzwerkes auf die mechanischen Eigenschaften ist im Kristallingestein sehr ausgeprägt. Daher können die mechanischen und Spannungsheterogenitäten allein auf das Auftreten von Klüften und Alteration zurückgeführt werden. Da die meisten EGS Systeme auf Kristallingestein zielen, ist das Ergebnis dieser Arbeit, das den überragenden Einfluss der petrografischen und lithologischen Eigenschaften auf die Bohrlochstabilität und induzierte Seismizität in Granit zeigt von zentraler Bedeutung für die weitere Entwicklung von EGS. Der entwickelte numerische Code erlaubt es weiterhin, eine Variation der Bedingungen vorzunehmen, die unter Laborbedingungen nicht erreicht werden können, so z.B. hohe Temperaturen und Druck auf einer größeren Skala, vergleichbar mit dem Reservoir.

Die Grundlage dieser Studie waren mehrere geophysikalische Logs und ein Katalog induzierter Seismizität der GEIE Heat Mining in Soultz. Die Doktorarbeit wurde vom Indonesia Directorate General of Higher Education (DIKTI), dem Deutschen Akademischen Austauschdienst (DAAD), der Energie Baden-Württemberg (EnBW) sowie vom Helmholtz Förderprogramm finanziert.

# Acknowledgements

I have to be thankful to many people for their support during the work on this thesis.

The PhD research was funded by the Indonesia Directorate General of Higher Education (DIKTI), the German Academic Exchange Service (DAAD). Additional support from the Energie Baden-Wuerttemberg (EnBW) and the Helmholtz Association of German Research Centres is appreciated.

Thank you to my supervisor Thomas Kohl who gave me a lot of trust and freedom to develop my own ideas but also encouraged and demanded me to take on new challenges. I could be sure of his absolute support in good and in difficult times.

I am thankful to Friedemann Wenzel for taking the responsibility of being co-examiner, and for stimulating discussions on science and seismicity.

Thanks to Frank Schilling and Thomas Seelig for inspiring discussions and for advice throughout my work.

Special thanks to Martin Schoenball and Carola Meller for careful reviews of my research and for reflections from a broad perspective of numerics and geology. Working with you was (and hopefully will be) a pleasure!

Thanks to Albert Genter and Thomas Kölbel for letting me work on the Soultz dataset and for his support in analyzing it. Also to Emmanuel Gaucher for so many good discussions, for sharing your experience and your proofreading skills.

I thank all members of the Petrotherm working groups for an awesome working atmosphere, which kept me motivated when science was less motivating! Thanks to Manu and Robin for the IT support. To Fabian, Jorg, Sebastian, Niklas for taking me to the football games, well at least I experienced the run to catch the long ball you passed to me. To Xavier for so many sports, biking, and hiking trip we did together.

Thanks also to the big Indonesian families in Karlsruhe for making me a little less homesick, e.g. Yodha et al, Nurdin et al, Ikhwan et al, Oding, Hendro among many others.

A big thank you is due to Silke Schlichting, who kept the working groups running!

Many thanks to my wife, Anisha, for accompanying me through the highs and lows of the last years. Finally, I thank my mother and my sister Tiara Sahara and brother Yuslim Sahara for their unconditional support in all aspects.



# Table of contents

<b>Abstract</b>	<b>i</b>
<b>Zusammenfassung</b>	<b>iii</b>
<b>Acknowledgements</b>	<b>vi</b>
<b>Introduction</b>	<b>1</b>
1.1 Enhanced geothermal systems	2
1.2 Motivation	3
1.3 Thesis structure	5
<b>Rock mechanics in reservoir engineering</b>	<b>8</b>
2.1 Basic constitutive laws	8
2.1.1 Linear elasticity	9
2.1.2 Poroelasticity and effective stress	10
2.1.3 Rock deformations	11
2.2 Mechanical properties of the rock	12
2.2.1 Rock strength	13
2.2.2 Static and dynamic elastic moduli	14
2.3 State of stress in the reservoir	16
2.3.1 Crustal stress model	16
2.3.2 In-situ stress field in the reservoir	16
2.4 Numerical methods of rock deformations	18
2.4.1 Continuum damage mechanics	18
2.4.2 Damage propagation	20
<b>Impact of fracture networks on borehole breakout heterogeneities in crystalline rock</b>	<b>21</b>
Abstract	21
3.1 Introduction	22
3.2 State of stress in the Soultz-sous-Forêts geothermal field	23
3.2.1 Geological context	23
3.2.2 Principal horizontal stress orientation inferred from breakout observation	26
3.2.3 Detailed breakout shape analysis and its correlation with fracture densities	27

3.3 Breakout heterogeneity and its connection with fracture networks	30
3.3.1 Influence of fracture zones	30
3.3.2 Influences of natural fractures	33
3.4 Discussions	35
3.5 Conclusions	37
<b>Analysis of state of stress in a deep fractured crystalline rock</b>	<b>39</b>
Abstract	39
4.1 Introduction	40
4.2 Soultz-sous-Forêts geothermal field	41
4.2.1 Geological setting	42
4.2.2 Geomechanical properties of the crystalline rock	43
4.3 State of stress in Soultz-sous-Forêts	44
4.3.1 Wellbore failures in an inclined well	46
4.3.2 Estimation of the in-situ stress field and its heterogeneities	48
4.4 Wellbore failure in a heterogeneous fractured material	52
4.5 Discussions	55
4.6 Conclusion	57
<b>Characterization of the mechanical heterogeneity and their role in induced seismicity in Soultz-sous-Forêts fractured crystalline reservoir</b>	<b>59</b>
Abstract	59
5.1 Introduction	60
5.2 Soultz-sous-Forêts geothermal field	61
5.3 Deep reservoir characterization from borehole observation	64
5.3.1 Input data	65
5.3.2 Neural network clustering	65
5.3.3 Stress and mechanical properties	68
5.3.4 Fracture reactivation	69
5.4 Induced seismicity due to hydraulic stimulation	71
5.5 Discussion	73
5.6 Conclusion	78
<b>Analysis of borehole breakout development using continuum damage mechanics</b>	<b>81</b>
Abstract	81

6.1	Introduction	82
6.2	Theoretical framework	83
6.2.1	Fracturing and damage	83
6.2.2	Continuum damage mechanics (CDM)	84
6.3	Numerical Modeling of CDM	86
6.3.1	Numerical procedure and borehole model	87
6.3.2	CDM synthetic borehole breakout modeling	88
6.3.3	Sensitivity test	91
6.4	Analysis of borehole breakout	92
6.4.1	The effect of far field stress	93
6.5	Discussion and conclusion	95
	<b>Conclusions and outlook</b>	<b>98</b>
	<b>References</b>	<b>103</b>



---

## Introduction

The source of geothermal energy is the vast heat stored within the earth. The Earth's thermal energy flows to the surface under ambient conditions at a rate of 960 EJ/year [Pollack *et al.*, 1993]. This energy rate is almost twice the current energy consumption from all primary sources (560 EJ/year in 2013) [IEA, 2013]. Yet, it was not until the early 20<sup>th</sup> century that geothermal was harnessed for industrial and commercial purposes. In 1904, electricity was first produced using geothermal steam at the hydrothermal field in Lardarello, Italia. Since then, other developments have led to an installed electrical capacity of about 11.7 GW<sub>e</sub> and direct use of more than 70 GW<sub>t</sub> at 2015 [Lund and Boyd, 2015]. Geothermal energy has low environmental impact and CO<sub>2</sub> emissions, able to provide base load powers and has ubiquitous resources. Therefore, the International Energy Agency (IEA) envisions geothermal to supply a substantial part of future energy production. IEA projects that geothermal could contribute about 5.8 EJ per year by 2050 [IEA, 2013].

According to REN21 [2013], the total capacity of geothermal is currently contributing to only ~2.4% of the total installed capacity of renewables. This small share is mainly originated from the high conductive heat flow area near the tectonic plate boundaries. In such area, the high enthalpy geothermal reservoir can be easily found in few hundreds meter depth, e.g. in Iceland, New Zealand, the Philippines, and Indonesia. However, often the high enthalpy zone are clustered in a small part of the country. For instance, in Indonesia, the utilization of the geothermal energy is centered only in Java and Sumatra islands while the mid enthalpy and a magmatic geothermal system in the eastern part is much less developed (Figure 1.2).

Therefore, to exploit vast quantities of geothermal energy from a wider area, a new concept of the Enhanced Geothermal System (EGS) is introduced. The idea is to exploit geothermal energy from a body of rock containing commercially-sufficient energy, the recoverability of which has been increased by artificial means such as hydraulic stimulation [AGRCC, 2010]. The advantage of this concept, compared to the conventional volcanic geothermal, is that it can be applied to almost every crustal rock. Due to its enormous potential, IEA sees EGS as a major pillar of geothermal

energy production in the future, with more than half of projected increase of installed capacity being of EGS-type by 2050. Hence, a lot of research and development, particularly in EGS, has to be done to reach the IEA goal.

## 1.1 Enhanced geothermal systems

For the most of the continental crust, such as in central Europe, geothermal resources need to be harnessed from deep crystalline basement rocks, typically from 3 to 5 km, which provides much less natural permeability. The EGS concept is to drill two or more boreholes to depths where temperatures are of commercial interest and extract the heat from the rock mass between them by circulating fluid around the loop (Figure 1.2). In some fields, fault systems are the main target for circulation water since they are expected to yield high production rates that are needed for economical operation of the power plant.

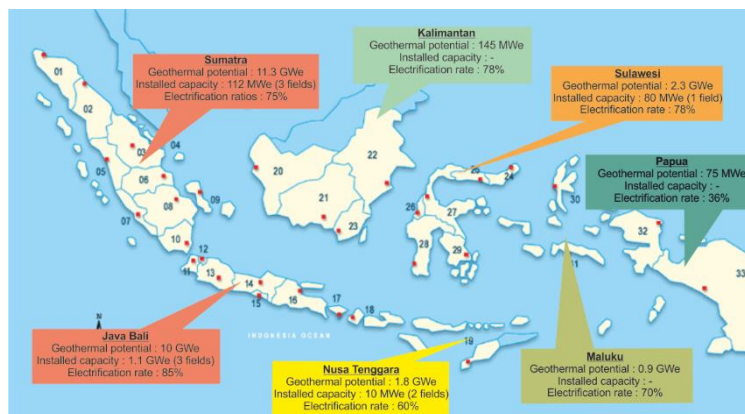
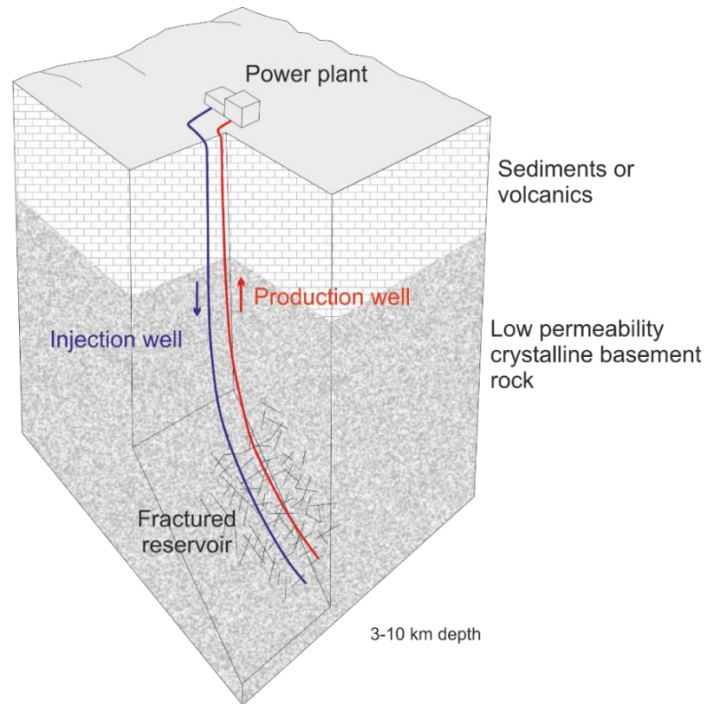


Figure 1.1: Distribution of geothermal potential and electrification ratios in Indonesia (data from Poernomo et al. [2015]). The eastern part of Indonesia is characterized by low geothermal potential but lack of other types of energy (low electrification ratios).

Often the natural permeability of the deep crystalline rocks is too low to provide the required flow between the wells and thus must be enhanced. Hydraulic stimulation, in which a large volume of fluid is injected into the rock mass at high flow rates, serves as a potential mean for improving the connection between the borehole and the natural fracture system. Hydraulic stimulations have been performed at various EGS reservoirs and have produced mixed results in increasing the hydraulic connectivity between the wells [Murphy et al., 1999]. Large induced microseismic events, Mw > 2.0, have been reported during and after the stimulation at commercial-scale EGS sites, e.g. Soultz (France) [Baria et al., 1999], the Cooper Basin (Australia) [Baisch et al., 2006], and Basel (Switzerland) [Mukuhira et al., 2013; Majer et al., 2007]. Even in Basel, they cause considerable damage to buildings, with damage claims amounted to more than US\$9.0 million [Giardini, 2009]. This made the Basel project was then suspended and was finally discontinued in 2009. Problems of wellbore stability that might arise during the drilling of several geothermal wells could also cause substantial additional cost, which endangered the whole project

Apart from its technical problem, there are also social and political issues such as lack of public awareness, an inappropriate regulatory environment, and the difficulties of competing with conventional energy sources [Pasqualetti, 2011; Barbier, 2002; Rybach, 2003]. Cost projections for EGS are also difficult to be calculated since current projects are still pilot-scale with a large amount of research and development, particularly in the drilling and the stimulation phases of the projects [IEA, 2013]. Nevertheless, geothermal is the only renewable energy sources that could serve as base load due to its abundant energy sources availability and its low externality costs.



**Figure 1.2:** Schematic of a conceptual two-well Enhanced Geothermal System in hot rock in a low-permeability crystalline basement formation [modified from *US Department of Energy*, 2006].

To date, it can be concluded that EGS systems are not in regular use yet because the technology to develop fully “engineered reservoir” is still under development. Success in the development of EGS technology will greatly increase both the scale of the usable resource and the number of countries that can benefit from this vast energy resources. Specifically, research and technology development is needed in the following areas: more cost-effective drilling, reservoir characterization, and monitoring, improved numerical reservoir modeling and reservoir management techniques.

## 1.2 Motivation

Extracting a heat energy from a deep EGS reservoir is a challenging task, in particular because of the high in-situ stress acting on a deep fractured crystalline rock. Hydraulic stimulation and wellbore stability have become constant issues frequently encountered during the life geo-reservoir projects [Fjaer *et al.*, 2008; Zoback, 2007].

Especially, in the last few years, hydraulic stimulation campaign has been heavily criticized by the community due to its potential in creating large magnitude events. For future use of this technique, the geomechanical aspects of induced seismicity have to be better understood to increase the success ratio of the permeability enhancement and facilitate future mitigation of felt seismicity. Authorities, politics, and the society demand guaranteed safety and minimal nuisance by the exploitation to be able to accept the application of these technologies.

A comprehensive geomechanical model of a reservoir could provide a basis for addressing a broad range of rock-mechanics-related problems that might encounter during the life of a geo-reservoir. Although significant progress has been made in oil and gas industry, technical challenges unique to the geothermal area, e.g. high temperature and pressure, crystalline basement, and fewer data collection, have limited the use of geomechanics in the development of the geothermal reservoir. As the geothermal industry move to develop more challenging resources using the concept of EGS, the need for improving the geomechanical model and developing specific technologies for geothermal reservoir has become critical.

Rock mechanics research can impact areas related to in-situ stress characterization, initiation and propagation of artificial and/or nature fractures, and the effect of coupled hydro-thermo-chemo-mechanical processes on induced seismicity. This has an important role in optimizing reservoir design and heat extraction strategies for sustainable geothermal energy development. The quality of such model is, however, dependent on the nature of the reservoir geology. The limited availability of relevant data is also part of the problem. For that reason, it is essential that we are aware of the high potential of the technique, together with the actual limitations.

Over the past 25 years, a number of European research teams have worked on putting together a detailed picture of the deep crystalline rock at the site of the Soultz EGS project. This project is arguably the most comprehensive research project in the field of EGS, which has been developed so far. It has now a long history which is broadly documented, e.g. *Baria et al.* [1999], *Gérard et al.* [2006], and benefits from a vast amount of field observations in numerous domains (geology, geochemistry, geophysics, petrophysics, hydrogeology, etc.) gathered during the exploration, drilling, stimulation, circulation, production phases. Over the development phases of the EGS, five wells have been drilled and stimulated to create underground heat exchangers in the granitic formation. Due to its long-term operation experience and its immense geodatabase, the Soultz-sous-Forêts site is predestined for the development and testing techniques applicable to characterize the geo-mechanical properties of crystalline reservoirs, and it was therefore selected as a basis for this thesis.

### 1.3 Thesis structure

---

This thesis is presented as a cumulative dissertation comprising of four individual studies on the characterization of the stress and mechanical properties of deep Soultz-sous-Forêts reservoir. Two studies are published in or submitted to international



journals, one study is published as a reviewed conference paper of the World Geothermal Congress in 2015, and one is currently prepared for publication in an international journal. The studies are ordered such that a systematic description of rock mechanics studies of deep EGS can be drawn.

As drilling and hydraulic stimulation are the major challenges for EGS campaign, the main goals of this thesis are an increased understanding of most prominent aspects of rock mechanics in characterizing the mechanical behavior of reservoir as disturbed by drilling and massive fluid injection. The present thesis aims at presenting novel approaches of geomechanical studies at various scale from minor-fracture-scale to the reservoir scale (Figure 1.3).

Approaches developed in this thesis are based on an integrated analysis of borehole data measured from the most inclined well GPK4 in Soultz-sous-Forêts. Hydraulic data is used to analyze the characteristics of induced seismicity with respect to the stress and mechanical heterogeneities in the reservoir. On top of this, numerical modeling is performed to analyze the inelastic deformation that leads to the development of wellbore failures.

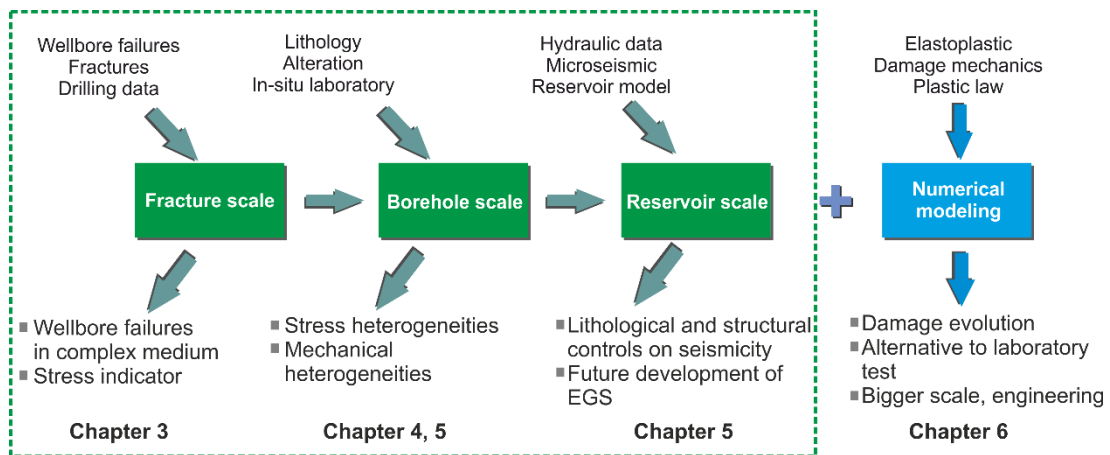


**Figure 1.3:** Work flow of the various scale studies developed in this thesis. The green boxes within the dashed line represent the studies that are based on field observation and analysis, while the blue box represent the numerical modeling.

The basic of rock mechanic in reservoir engineering is presented in **Chapter 2**. Then, the studies are presented in separate chapters, as outlined in the followings.

### The impact of fracture network

This thesis starts with an analysis of the impact of fracture networks on the development of borehole breakouts (**Chapter 3**). This is inferred from a detailed analysis of 1221 borehole elongation pairs in the vicinity of 1871 natural fractures observed in the crystalline section of the GPK4 well of the Soultz-sous-Forêts geothermal field (France). Details of stress perturbations associated with small natural fractures, not only with major fracture zones, are studied for a better understanding of the impact of the natural fracture network on breakout heterogeneities in granite rock. Herein, I first identify all faults and fractures

accompanied by stress-induced breakouts in the crystalline section of the GPK4 well at the Soultz-sous-Forêts geothermal field. Then, I investigate the possible relationship between the breakouts and the mechanical perturbation due to the presence of faults and fractures. The influence of fracture density to the material heterogeneity, inferred from the detailed analysis of breakout shape, is outlined. Furthermore, the importance of material heterogeneity resulting from fracture occurrence to breakout development is examined.

### **Stress state in a fractured crystalline reservoir**

In addition to the breakouts and fractures data from the previous chapter, 827 drilling-induced tensile failures are included to infer the in-situ stress field and its heterogeneity in the Soultz geothermal field (**Chapter 4**). The distribution of the compressional strength of the crystalline rock used for stress inversion are determined based on previous in-situ laboratory measurements, sonic log run in the shallower section of GPK2 well and the petrographic log. The different characteristics of wellbore failures that might represent the stress field and its local heterogeneity are discussed. The stress profile is estimated based on the selected wellbore failures input data. Then, using the in-situ stress field profile and the compressional strength profile obtained in this study, the impact of wellbore trajectory on the wellbore stability in the most deviated GPK4 well is estimated.

### **Mechanical properties and hydraulic stimulation**

The limitation of the deep core data necessitates tools to characterize the mechanical properties indirectly from borehole data. In **Chapter 5**, I apply a neural network clustering scheme to identify inherent structures present in a set of geophysical logs of the GPK4 well, i.e. magnetic susceptibility, fracture, alteration, and breakout. The variation of the frictional strength in the reservoir is identified based on the characteristic of rocks observed from borehole data. On the top of this, the slip tendency of all minor and major fractures in each zone is estimated. Hydraulic stimulation data performed in the same well are then used to infer the patterns of the microseismic events in the different zone proposed from borehole data, i.e. the occurrence time and density of microseismic events as well as the stimulated area. The role of each parameter in affecting the failure mechanism due to hydraulic stimulation is discussed. This integrated analysis can provide key information on the lithological controls on induced seismicity due to stimulation.

### **Numerical modeling of borehole breakouts**

To improve the understanding of the mechanism of wellbore failures observed in the previous studies, a numerical modeling that implicitly account the complex fracturing process and inelastic deformation is developed (**Chapter 6**). A continuum damage mechanics (CDM) concept that takes tensile and compressive failure mechanisms into account is implemented to model the development of the borehole breakout in an inhomogeneous elastoplastic material. This investigation allows us to account for both tensile and compressive failure. I use the single constitutive law by *Lee and Fenves* [1998] in our modeling scheme. The plastic law obtained by *Busetti et*

*al.* [2012b] is used as a basis for the non-linear deformation involved in the simulation. A sensitivity study is performed to analyze the significance of each parameter possibly affecting the dimensions of borehole breakouts. I compare the numerical results to available experimental data [*Haimson and Lee, 2004*]. In general, a good match between modeling and laboratory experiment results is achieved

---

## Rock mechanics in reservoir engineering

The Committee on Rock Mechanics of the Geological Society of America defines rock mechanics as “the theoretical and applied science of the mechanical behavior of rock; it is that branch of mechanics concerned with the response of the rock to the force fields” [Jaeger *et al.*, 2007]. This illustrates the importance of rock mechanics in the life of geo-reservoir.

The large tectonic forces caused the crustal rocks to be pre-stressed [Zang *et al.*, 2010]. These stresses are acting as we extract/inject materials from/to the crust in boreholes, mines, and underground constructions. In a critically stressed area, failure is likely to occur, e.g. a fault reactivation due to a hydraulic stimulation [Barton *et al.*, 1995; Rutqvist *et al.*, 2015], rock burst in deep mining [Brady and Brown, 2005] and casing collapse in a high overburden stress area [Moos *et al.*, 2003]. The inhomogeneity of the mechanical properties of rock could also play a role in such failures [Amadei, 1996]. As those failures could bring damage to the geo-project operation as well as to the community, this necessitates an estimation of the pertinent parameters required to properly characterize the geomechanical aspects of the targeted formation.

In the following section, I give a brief overview of some most important aspects of rock mechanics to characterize the mechanical behavior of reservoirs as disturbed from its initial condition, e.g. drilling and hydraulic stimulation, which are the focus of this thesis. The introduction of geomechanical aspects follows the monographs of Zoback [2007], Brady and Brown [2005], Fjaer *et al.* [2008], Jaeger *et al.* [2007], Scholz [2002], and Shen *et al.* [2014]. Then, the fundamental of mechanical properties and in-situ stress for reservoir engineering are presented. This is followed by a brief description of a numerical method for rock mechanics, with a focus on continuum damage mechanics technique.

### 2.1 Basic constitutive laws

---

A constitutive law describes the deformation of a rock in response to an applied stress or vice versa. A rock specimen starts to deform when it is submitted to a load; the higher the stress level, the more strain the rock experiences. A concept of rock mechanics test is presented in **Figure 2.1** to illustrate how a rock exhibits different characteristic over different range of applied stresses. Deformation begins with a

small degree of crack closure upon initial application of stress followed by linear elastic behavior over a significant range of stresses. Then, deformation involves many inelastic processes, e.g. microfracturing, formation of shear zones, compaction bands, and tight folds, prior to eventual failure of the sample [Katz and Reches, 2004; Reches and Lockner, 1994].

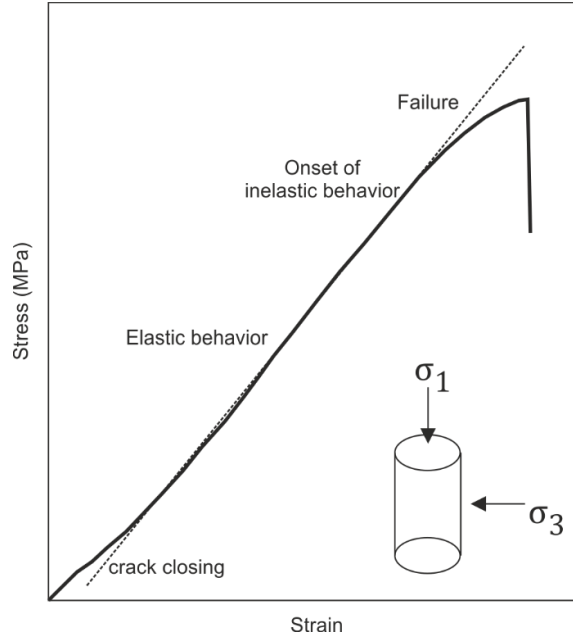


**Figure 2.1:** Typical laboratory stress–strain data for a rock sample being deformed. Different deformation stage are presented (modified after Paterson and Wong [2005])

### 2.1.1 Linear elasticity

In a linear elastic material stress and strain are proportional and deformation is reversible. The description of elastic constitutive laws begins with a definition of deformation by considering the components of the strain tensor  $\varepsilon_{ij}$  as a function of displacement field  $\vec{u}$

$$\varepsilon_{ij} = \frac{1}{2} \left( \frac{\delta u_i}{\delta x_j} + \frac{\delta u_j}{\delta x_i} \right) \quad (2.1)$$

The general formulation that relates stress to strain is

$$\sigma_{ij} = c_{ijkl} \varepsilon_{ij} \quad (2.2)$$

where  $c_{ijkl}$ , the elastic stiffness matrix, is a fourth-rank tensor. Since the strain and stress tensors are symmetric,  $c_{ijkl}$  must be symmetric in  $(k,l)$  and  $(i,j)$ , respectively. Furthermore, the strain energy function requires  $c_{ijkl} = c_{klij}$  [Scholz, 2002]. In a homogeneous and isotropic material, principal stresses and principal strains act in the same directions. Stress can be expressed in terms of strain by a generalized Hooke's law

$$\sigma_{ij} = \lambda \delta_{ij} \sum_{i=1}^3 \varepsilon_{ii} + 2G \varepsilon_{ij} \quad (2.3)$$

where  $\lambda$  is Lamé's constant and  $G$  is shear modulus and the Kronecker delta,  $\delta_{ij}$ , is given by

$$\begin{aligned}\delta_{ij} &= 1 \quad \text{if } i = j \\ \delta_{ij} &= 0 \quad \text{if } i \neq j\end{aligned}\tag{2.4}$$

**Table 2. 1:** Relationships among elastic moduli in an isotropic material [from *Zoback, 2007*]

$E$	$\nu$	$\frac{G}{E}$	$\frac{K}{E}$	$\frac{\lambda}{E\nu}$
—	—	$2(1 + \nu)$	$3(1 - 2\nu)$	$(1 + \nu)(1 - 2\nu)$
—	$\frac{E - 2G}{2G}$	—	$\frac{EG}{3(3G - E)}$	$\frac{G(E - 2G)}{3G - E}$
—	$\frac{3K - E}{6K}$	$\frac{3KE}{9K - E}$	—	$\frac{3K(3K - E)}{9K - E}$
$2G(1 + \nu)$	—	—	$G \frac{2(1 + \nu)}{3(1 - 2\nu)}$	$G \frac{2\nu}{1 - 2\nu}$
$3K(1 - 2\nu)$	—	$3K \frac{1 - 2\nu}{2 + 2\nu}$	—	$3K \frac{\nu}{1 + \nu}$
$\lambda \frac{(1 + \nu)(1 - \nu)}{\nu}$	—	$\lambda \frac{1 - 2\nu}{2\nu}$	$\lambda \frac{1 + \nu}{3\nu}$	—
$\frac{9KG}{3K + G}$	$\frac{3K - 2G}{6K + 2G}$	—	—	$\frac{3K - 2G}{3}$
$\frac{G(3\lambda + 2G)}{\lambda + G}$	$\frac{\lambda}{2(\lambda + G)}$	—	$\frac{3\lambda + 2G}{\lambda}$	—
$9K \frac{K - \lambda}{3K - \lambda}$	$\frac{\lambda}{3K - \lambda}$	$3 \frac{K - \lambda}{2}$	—	—

The bulk modulus  $K$  of a volume  $V$  due to pressure  $P$  is obtained from

$$K = -V \frac{dP}{dV} = \lambda + \frac{2}{3}G\tag{2.5}$$

Finally, Young's modulus  $E$  and Poisson's ratio  $\nu$  are found from

$$E = G \frac{3\lambda + 2G}{\lambda + G}\tag{2.6}$$

$$\nu = \frac{\lambda}{2(\lambda + G)}\tag{2.7}$$

An important aspect of the theory of elasticity in homogeneous, isotropic material is that only two of the elastic moduli ( $\lambda, G, K, E, \nu$ ) are needed to describe material behavior. Hence, it is often convenient to express elastic moduli with respect to each other (**Table 2. 1**)

### 2.1.2 Poroelasticity and effective stress

Pore fluids in the reservoir rock play an important role because they support a portion of the total applied stress. Hence, only a portion of the total stress, namely, the effective stress component, is carried by the rock matrix (**Figure 2.2**). Obviously, this effective stress changes over the life of the reservoir. In addition, the mechanical behavior of the porous rock modifies the fluid response. Two basic mechanisms highlight this coupled behavior [*Detournay and Cheng, 1988*]:

- An increase of pore pressure induces rock dilation.
- Compression of the rock produces a pore pressure increase if the fluid is prevented from escaping from the porous network.

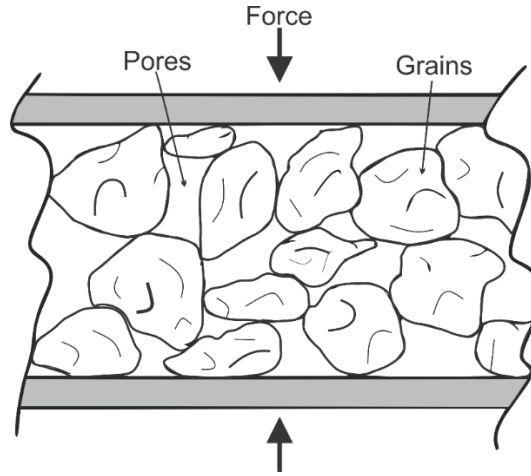


**Figure 2.2:** Load sharing by pore pressure. Total stress is the total of pore pressure and effective stress carried by the grains.

*Terzaghi* [1923] first introduced the effective stress,  $\sigma_{ij}$ , concept for one-dimensional consolidation and proposed the following relationship

$$\sigma_{ij} = S_{ij} - \delta_{ij}P_p \quad (2.8)$$

which means that pore pressure influences the normal components of the stress tensor,  $\sigma_{11}$ ,  $\sigma_{22}$ ,  $\sigma_{33}$  and not the shear components  $\sigma_{12}$ ,  $\sigma_{23}$ ,  $\sigma_{13}$ . Thus, to consider the effect of pore fluids on stress we can re-write (2.3) as follows

$$\sigma_{ij} = \lambda \delta_{ij} \sum_{i=1}^3 \sigma_{ii} + 2G \varepsilon_{ij} - \delta_{ij}P_p \quad (2.9)$$

Empirical data have shown that the effective stress law is a useful approximation which works well for a number of rock properties, e.g. intact rock strength and the frictional strength of fault [*Lockner and Byerlee, 1993; Byerlee, 1978*].

### 2.1.3 Rock deformations

The deformation of most rock materials is a process of crack initiation and propagation. Based on its displacement plane, the propagation of cracks can be categorized into three modes (**Figure 2.3**). Mode I is tensile, or opening, mode in which the crack wall displacements are normal to the crack. Mode II, or in-plane shear mode, exhibits the displacements in the plane of the crack wall normal to the crack edge. Mode III, or anti-plane shear mode, when the displacements are in the plane of crack and parallel to the edge. Observations and experiments show that the deformation of rocks is the combination of those three modes [*Shen et al., 2014*].

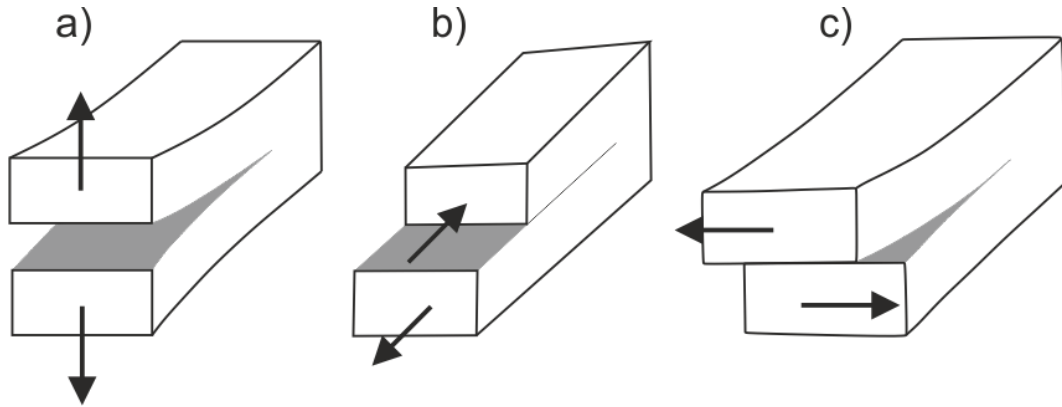


**Figure 2.3:** The three deformation mode. a) Opening mode, b) in-plane shear mode and c) anti-plane shear mode

It has been shown in **Figure 2.1** that most rocks exhibit nonreversible deformations or at least a non-linear relationship between stress and strain during its deformation. This means that rocks are not perfectly elastic materials, and a number of theories have been developed to model such behaviors, e.g. continuum damage mechanics [Lubliner *et al.*, 1989; Chaboche, 1981] and time-dependent analysis (creep) [Kachanov, 1958; Rabotnov, 1968].

In the incremental theory of plasticity, the strain tensor  $\varepsilon$  is decomposed into the elastic part  $\varepsilon_e$  and the plastic part  $\varepsilon_p$ , which for linear elasticity is given by

$$\varepsilon = \varepsilon_e + \varepsilon_p \quad (2.10)$$

Predicting the plastic strain increment requires a yield criterion that indicates whether plastic deformation occurs, a flow rule that describes how the plastic strain develops and a hardening law. The yield criterion is a relationship between stresses that is used to define conditions under which plastic deformation occurs. In three dimensions, this is represented by a yield function that is a function of the state of stress and a hardening parameter:

$$f(\sigma_1, \sigma_2, \sigma_3, h) = 0 \quad (2.11)$$

with  $h$  is the hardening parameters which represents the increasing microcrack density with increasing load which governs the evolution of the yield curve.

## 2.2 Mechanical properties of the rock

The information of the mechanical properties of reservoir are of major concern for reservoir engineer. Often deformation initiated at points of low rock strength area and inhibited from propagating into adjacent of higher strength [e.g. Zoback [2007], Borg and Handin [1966], Kaiser *et al.* [1985]]. This is particularly essential for deep CO<sub>2</sub> storage, underground mining and hydraulic fracturing, in which the mechanical properties of the target formation and the surrounding rock must be known precisely.

This section briefly describes some important aspects of the estimation of the mechanical properties of rock from typical laboratory and geophysical logging tools.



The example of characterization of mechanical properties of the deep crystalline reservoir from an integrated analysis of borehole data is presented in chapter 6.

### 2.2.1 Rock strength

The first parameter to be determined from the test is the strength of a rock, which is the stress at which the rock fails or loses its integrity. The failure of rock in compression is a complex process that involves the creation of small tensile cracks and frictional sliding on grain boundaries [Brace *et al.*, 1966]. Eventually, there is a coalescence of these microscopic failures into a major shear plane [Katz and Reches, 2004; Reches and Lockner, 1994]. In brittle rock, the failure occurs abruptly with the material essentially losing all of its strength (sudden stress drop in stress-strain curves like that shown in Figure 2.1. While in ductile rock, it occurs more gradually. The compressional strength of the rock is the peak stress before this failure occurred. The uniaxial compressive strength (UCS) of massive granites vary from around 100 MPa to 200 MPa [Paterson and Wong, 2005].

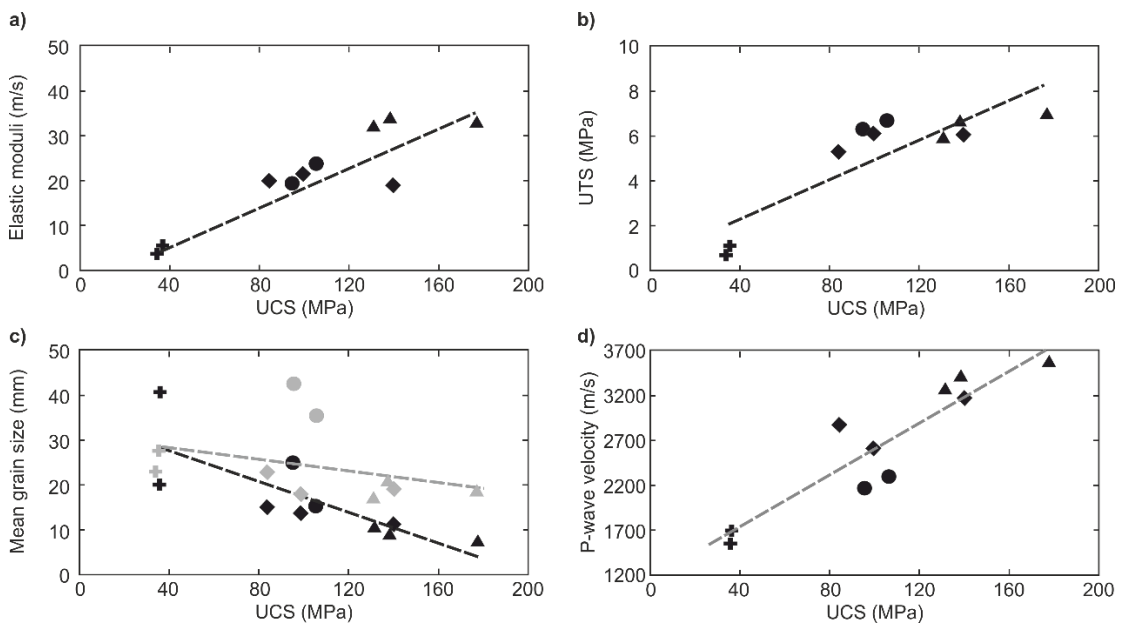


**Figure 2.4:** Relationship between uniaxial compressive strength of granite samples from Himalayan area with elastic Young's modulus (a), uniaxial tensile strength (UTS) (b), mean mineral grain size (c), and P-wave velocity (d). Symbol are same for all subfigures. Color in (c) indicates different mineral: grey for quartz and black for plagioclase (modified from Sajid *et al.* [2016]).

The tensile strength of most rocks is quite low, on the order of just a few MPa [Moore and Lockner, 1995]. Especially, when pre-existing cracks exist in rock, e.g. in the case when considering tensile fractures creation in borehole [Peška and Zoback, 1995], tensile strength would be expected to be near zero.

Laboratory measurements of granites from Himalayan regime show that the strength of the rock highly affected by the petrographic features of the rock [e.g. Sajid *et al.* [2016], Copeland *et al.* [1990], Le Fort *et al.* [1980]]. The level of fracture and alteration and the size of mineral grain are found to have a negative correlation with

UCS (**Figure 2.4**). Studies from other regions are also supported this finding [e.g. *Alm et al.* [1985], *Sousa* [2012], *Rigopoulos et al.* [2013]]. The explanation might be that those existing cracks promote the initiation of deformation at much lower stress [*Heap and Faulkner*, 2008]. In addition, the process of alteration is usually accompanied by an enrichment of clay minerals in the veins and rock matrix. In this case, clay might act as a zone of weakness in either the rock matrix or the fracture core and, hence, reduce the strength of the rock as well [*Julia et al.*, 2014; *Tembe et al.*, 2010; *Sausse*, 2002]. Different schemes recommended for classification of granites based on their degree of weathering and alterations are presented in **Table 2. 2**.

A number of other factors, e.g. occurrence of shale layers [*Kohli and Zoback*, 2013], high differential stress [*Nur and Simmons*, 1969], aligned minerals (such as mica and clay) along bedding planes [*Thomsen*, 1986; *Sayers*, 1994a] can also affect the mechanical properties of the reservoir.

**Table 2. 2:** Weathering classification systems of granitic rocks [modified from *Brown*, 1981; *Norbury et al.*, 1995]

Grade	Rock type	Rock description	P-wave velocity (m/s)
I	Fresh rock	No visible sign of rock material weathering	3320 - 4315
II	Slightly altered	Slight discoloration and weakening. Schmidt hardness >45	2000 - 2450
III	Moderately altered	Considerable weakening. Penetrative. Discoloration. Schmidt hardness 25-45	
IV	Highly altered	Large pieces broken by hand. Schmidt hardness 0-25	518 - 900
V	Completely altered	All rock materials are decomposed and/or disintegrated to soil. The original mass structure is still largely intact	

### 2.2.2 Static and dynamic elastic moduli

Elastic property measurement can be made under static conditions or under dynamic conditions. Static elastic properties are usually measured using the laboratory measurement. Whereas, sonic measurements conducted in the laboratory can be used to determine the elastic properties under dynamic conditions. To obtain them, a mechanical pulse is imparted to the rock specimen, and the time required for the pulse to traverse the length of the specimen is determined [*Maoko and Nolen-Hoeksema*, 1994; *D. Goldberg and B. Zinszner*, 1989]. Elastic wave theory shows that the velocities of P-waves and S-waves ( $V_p$  and  $V_s$ , respectively) obtained in this measurements are related to the elastic constants through the following relationships [*Fjaer et al.*, 2008]:

$$V_p = \left[ \frac{K_{dyn} + \frac{4}{3}G_{dyn}}{\rho} \right]^{\frac{1}{2}} = \left[ \frac{E_{dyn}(1-\nu_{dyn})}{\rho(1+\nu_{dyn})(1-2\nu_{dyn})} \right]^{\frac{1}{2}} \quad (2.12)$$

$$V_s = \left[ \frac{G_{dyn}}{\rho} \right]^{\frac{1}{2}} = \left[ \frac{E_{dyn}}{2\rho(1+\nu_{dyn})} \right]^{\frac{1}{2}} \quad (2.13)$$

where  $\rho$  refers to the mass density of the rock specimen.

An alternative is to determine the properties downhole, through sonic log measurement. The concept of this sonic log is that a pressure pulse is created in a wellbore filled with fluid which result in the propagation of several types of waves into the formation [Roever *et al.*, 1974]. Using (2.16) and (2.17), the dynamic elastic properties of the rock can also be determined from sonic data.

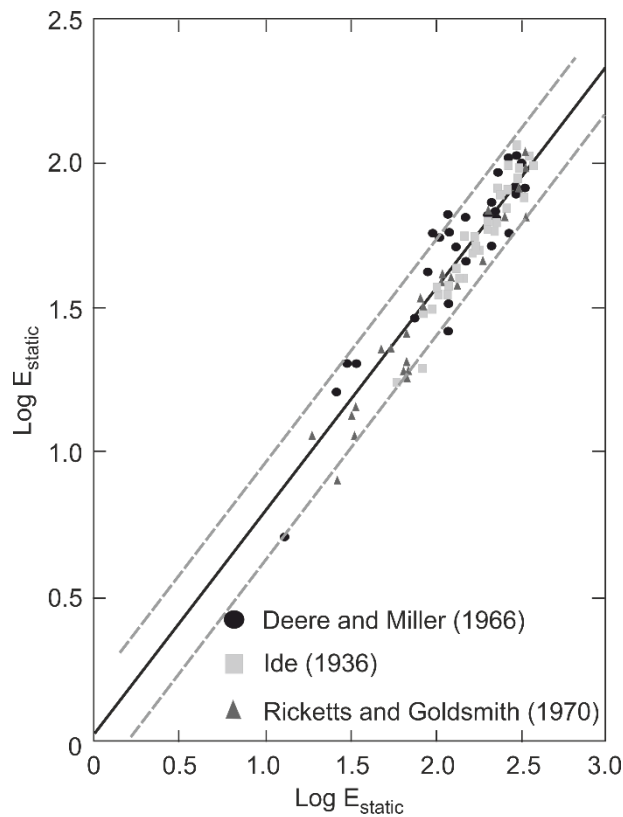


**Figure 2.5:** Correspondence between static and dynamic Young's modulus of rocks. The linear regression line with its 90% confidence limit are plotted in black and grey dashed line, respectively. (Source: Eissa and Kazi [1988], King [1983], Ricketts and Goldsmith [1970])

The ratio of the dynamic to static moduli may vary from 0.8 to about 3 and is a function of rock type and confining stress [Eissa and Kazi, 1988; Simmons and Brace, 1965; King, 1983]. **Figure 2.5** shows the typical correlations between static and dynamic moduli for sedimentary rock. These correlations allow an estimation of static in-situ elastic moduli values from log data where core data are not available.

## 2.3 State of stress in the reservoir

Long term geological processes like plate tectonics are driven by mechanisms that generate different types of stresses in the earth's crust. These stresses are acting as we extract materials from the crust in boreholes, mines and underground constructions. To better manage the underground reservoir, therefore, there is an obvious need for a good understanding of mechanical stresses in the earth's crust.

### 2.3.1 Crustal stress model

The stress field of the earth's crust is often described by three compressive principal stress components, namely the minimum horizontal stress ( $S_{hmin}$ ), the maximum horizontal stress ( $S_{Hmax}$ ) and the vertical stress ( $S_v$ ). The stress regime in a given environment depends on regional considerations, e.g. tectonics, topography, and local considerations, e.g. lithology, fracture characteristic, alteration [Zang *et al.*, 2010]. Understanding the interaction between regional and local considerations is important as it controls the state of stress in the reservoir.

It is generally assumed that the vertical stress is given by the weight of the overburden.

$$S_v = \int_0^z \rho(z)g dz \quad (2.14)$$

with ( $z$ ) is the depth-dependent density of the rock formation. The magnitude of the horizontal stresses determined by the tectonic setting and constrained by faulting as outlined in the following.

Faults form in the upper part the earth crust and are defined as planar discontinuities along which displacement (slip) occurs [Knipe, 1992]. Anderson [1951] developed the modern mechanical concepts of the origin of faults and defined the three principal stress regimes according to the relative magnitudes of the principal stresses. The three types of *Andersonian faulting* are summarized in **Figure 2.6**, i.e. reverse or thrust faulting, normal faulting and strike slip faulting.

Deep drilling and induced seismicity experiments at several locations worldwide indicate that, in general, the brittle crust in intraplate regions is critically stressed and pore pressures are close to hydrostatic, e.g. Zang *et al.* [2010]. This restricts possible magnitude of principal stresses for each faulting type even further. Using the Mohr-Coulomb faulting theory, the upper and lower bound of the magnitude of the in-situ stress state can be determined, and a stress polygon of allowed stress states can be drawn [Zoback, 2007].

### 2.3.2 In-situ stress field in the reservoir

Reservoir stress model starts with a rough estimates of the stress profile as a function of depth and rock properties. Later studies show that rock heterogeneities may induce local deviations from these linear trends [Cornet and Röckel, 2012]. The widespread use of hydraulic fracturing and wellbore imaging, especially in the oil and gas industries, has been a critical development that makes realization of the reservoir stress model possible.

Hydraulic fracturing techniques are commonly used to measure the minimum stress [Haimson, 1978]. This technique uses the pressure response obtained during initiation, propagation and closure of a hydraulically induced fracture to accurately determine the state of stress.

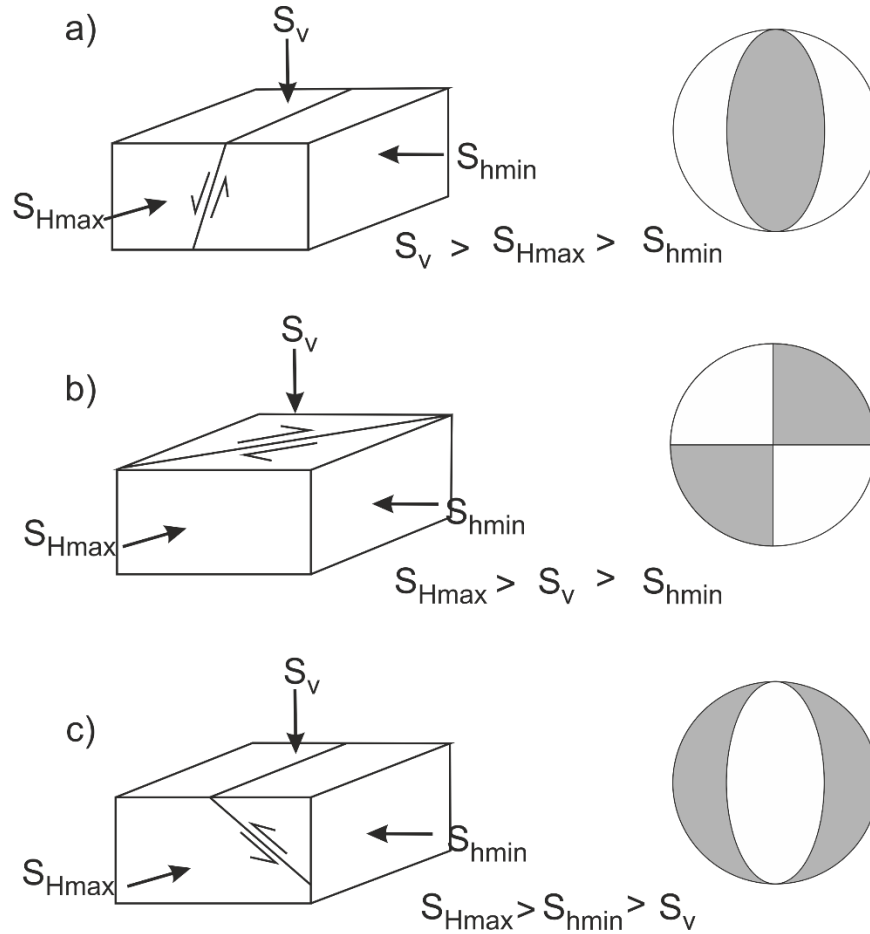


**Figure 2.6:** Anderson's classification scheme for the magnitude of principal stresses in normal (a), strike-slip (b) and reverse (c) faulting regions and its corresponding earthquake focal mechanisms.

The compressive and tensile failures, especially in arbitrarily inclined wellbores, are used to determine the orientation and magnitude of the principal horizontal stresses [Barton *et al.*, 1997; Brudy and Zoback, 1999; Zoback *et al.*, 2003]. The principal assumptions in those analyses are that the rock is isotropic and that it deforms elastically to the point of failure [Guenot, 1989; Cheatham Jr, 1993]. The magnitude of the stresses in the vicinity of borehole can be estimated using following equations,

$$\sigma_{rr} = \frac{1}{2}(S_{Hmax} + S_{hmin} - 2P_p) \left(1 - \frac{R^2}{r^2}\right) + \frac{1}{2}(S_{Hmax} - S_{hmin}) \times \left(1 - \frac{4R^2}{r^2} + \frac{3R^4}{r^4}\right) \cos 2\theta + \frac{P_p R^2}{r^2} \quad (2.15)$$

$$\sigma_{\theta\theta} = \frac{1}{2}(S_{Hmax} + S_{hmin} - 2P_p) \left(1 + \frac{R^2}{r^2}\right) - \frac{1}{2}(S_{Hmax} - S_{hmin}) \quad (2.16)$$

$$\tau_{r\theta} = \frac{1}{2}(S_{Hmax} - S_{hmin}) \left(1 + \frac{2R^2}{r^2} - \frac{3R^4}{r^4}\right) \sin 2\theta \quad (2.17)$$

where  $\theta$  is measured from the azimuth of  $S_{Hmax}$  and  $P_p$  is pore pressure.  $\sigma^{\Delta T}$  represents thermal stresses arising from the difference between the mud temperature and formation temperature (T).

Experimental tests [e.g. *Haimson et al., 2010*] and numerical models [e.g. *Sahara et al., submitted*] reveal that the development of breakouts involves complex fracturing process and inelastic deformation. The results of those studies give more constraints in using wellbore failures as stress indicator; only one far field principal stress component can be estimated from breakout geometry if the other two principal stresses are known and sufficient data on the plastic parameters are available. Therefore, geological features, e.g. fractures, alterations, and lithologies, have to be taken into account as it might affect the mechanical properties of the rock.

## 2.4 Numerical methods of rock deformations

Field and experimental studies display inelastic deformation of complex networks of fractures that cannot be explained by elastic analysis. This motivated the application of numerical methods in geoscience and engineering. Since beginning of 80's advances in the use of numerical methods in rock mechanics have been impressive [*Jing and Hudson, 2002*].

The Finite Elements Method (FEM) is perhaps the most widely applied numerical method across the geoscience and engineering fields. Since its origin in the early 1960s, much FEM development work has been specifically oriented towards rock mechanics problems [*Jing, 2003*]. The complex behavior of fractures initiation and growth, however, remains the main limiting factor in the application of the FEM and other numerical methods for rock mechanics problems. Special algorithms have been developed in an attempt to overcome this disadvantage, e.g. the 'enriched FEM' and 'generalized FEM' approaches [*Belytschko and Black, 1999; Strouboulis et al., 2001*] and implicitly model the crack using continuum damage mechanics approach [*Sahara et al., submitted; Lee and Fenves, 1998*].

### 2.4.1 Continuum damage mechanics

The continuum damage mechanics (CDM) approach does not prescribe the microcracks that causes the damage, it rather uses a damage parameter to define the effect of damage on the free energy of the system [*Chaboche, 1988*]. In this concept damage  $D$  and effective stress  $\sigma_{eff}$  represent the degradation of the elastic stiffness  $E$

$$\sigma_{eff} = E_0(\varepsilon - \varepsilon^p) \quad (2.18)$$

$$\sigma_{eff} = \sigma \frac{E_0}{E} = \frac{\sigma}{1-D} \quad (2.19)$$

$$D = 1 - \frac{E}{E_0} \quad (2.20)$$

The yield surface evolves with the damage and effective stress variable and limits the current admissible stresses. To account for the different damage responses of rock in tension and compression, a yield function which has more than one variable to describe the evolving yield surface, is used. Two state variables  $f_c$  and  $f_t$  are used to represent the uniaxial tensile strength and compressive strength of the material, respectively. Then the yield function is constrained by the following condition:

$$\tilde{F}(\sigma, f_c, f_t) \leq 0 \quad (2.21)$$

It is assumed that  $\tilde{F}$  is a first-degree homogeneous function with respect to all three variables. Also, it is assumed that  $\tilde{F}$  itself is an isotropic function in the stress space. The yield function remains isotropic even though its hardening behavior provides a more general evolution than the simple expansion or contraction of the yield surface.

$$f_t = [1 - D_t(\kappa_t)]\bar{f}_t(\kappa_t); \quad f_c = [1 - D_c(\kappa_c)]\bar{f}_c(\kappa_c) \quad (2.22)$$

where  $0 \leq D_t < 1$  and  $0 \leq D_c < 1$  are tensile and compressive degradation damage responses, respectively; and  $f_t$  and  $f_c$  are functions that represent the effective-stress responses in the uniaxial tensile and compressive stress functions, respectively. Because  $D_t$ , (or  $D_c$ ) is a function of only  $\kappa_t$ , (or  $\kappa_c$ ), the single degradation damage variable  $D$  can be used to describe both tensile and compressive degradation responses if it is defined as

$$D = D(\boldsymbol{\kappa}) = 1 - (1 - D_t)(1 - D_c) \quad (2.23)$$

The yield function in (2.21) can be rewritten as a function of stress and damage variables  $F(\bar{\boldsymbol{\sigma}}, \boldsymbol{\kappa}) = \tilde{F}(\bar{\boldsymbol{\sigma}}, \bar{f}_c, \bar{f}_t)$

$$F(\bar{\boldsymbol{\sigma}}, \boldsymbol{\kappa}) \leq 0 \quad (2.24)$$

in which  $F$  also is an isotropic, first-degree homogeneous scalar function with multiple-hardening evolution. With this framework, the elastoplastic responses in the present plastic-damage model are described only in terms of  $\bar{\boldsymbol{\sigma}}$  and  $\boldsymbol{\kappa}$ . The present constitutive system can be implemented effectively for numerical computation, because the solution for the elastoplastic response is separate from the degradation damage.

Following *Lee and Fenves* [1998], in term of stress invariants, the yield function takes the form

$$F = \frac{1}{1-\alpha} (\sqrt{3J_2} + \alpha I_1 + \beta \sigma_{max} - \gamma \sigma_{max}) - \sigma_c(\varepsilon_c^p) = 0 \quad (2.25)$$

with

$$\alpha = \frac{\frac{\sigma_{b0}-1}{\sigma_{c0}}}{2\left(\frac{\sigma_{b0}}{\sigma_{c0}}\right)-1}; \quad 0 \leq \alpha \leq 0.5 \quad (2.26)$$

$$\beta = \frac{\sigma_c(\varepsilon_c^p)}{\sigma_t(\varepsilon_t^p)} (1 - \alpha) - (1 + \alpha) \quad (2.27)$$

$$\gamma = \frac{3(1-K_c)}{2K_c-1} \quad (2.28)$$

where  $I_1 = tr(\sigma)$  is the first stress invariant,  $J_2 = \frac{1}{2}tr(s^2)$  is the second invariant of the deviatoric stress tensor  $s$ ,  $\sigma_{max}$  is the maximum principal stress;  $\frac{\sigma_{b0}}{\sigma_{c0}}$  is the ratio of initial equibiaxial compressive yield stress to initial uniaxial compressive yield stress;  $K_c$  is the stress intensity factor;  $\sigma_t(\varepsilon_t^p)$  is the tensile cohesion stress; and  $\sigma_c(\varepsilon_c^p)$  is the compressive cohesion stress.

A flow rule, which is assumed to be a non-associated potential plastic flow rule, is then used to evaluate the plastic strain. The flow rule can be written as:

$$G = \sqrt{(e \sigma_{t0} \tan\theta)^2 + J_2^{-2}} - I_1 \tan\theta \quad (2.29)$$

where  $\theta$  is the dilation angle measured in the  $I_1 - J_2$  plane at high confining pressure,  $\sigma_{t0}$  is the uniaxial tensile stress at failure; and  $e$  is the eccentricity

### 2.4.2 Damage propagation

Hillerborg's concept [Hillerborg *et al.*, 1976] is used in modeling the crack formation and growth during the damaging process. They proposed that when the crack opens the stress is not assumed to fall to zero at once, but to decrease with increasing crack width  $w$  (Figure 2.7). At the crack width  $w < w_t$  the stress has fallen to zero. As there is a stress to be overcome in opening the crack, energy is absorbed. A propagation criterion based on the Hillerborg's concept is easily implemented in finite element modeling. With this approach the rock's brittle behavior is defined by a stress-displacement response rather than a stress-strain response. This concept is implemented by defining a characteristic length associated with an integration point.

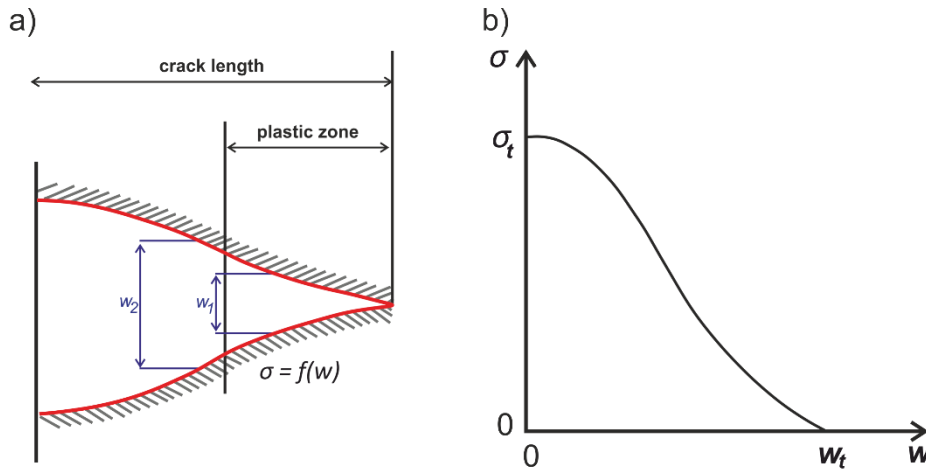


**Figure 2.7:** a) The Hillerborg model ] for stress intensity in the vicinity of crack tip. b) Assumed variation of stress  $\sigma$  with crack width  $w$ , in general case [modified from Hillerborg *et al.*, 1976.



---

## Impact of fracture networks on borehole breakout heterogeneities in crystalline rock

This chapter is published in International Journal of Rock Mechanics and Mining Sciences, doi:10.1016/j.ijrmms.2014.07.001.

### Abstract

Breakouts are commonly used as principal indicator of stress orientation. However, variation of breakout orientation with depth, especially in the vicinity of fracture zones, is frequently observed. This study describes a systematic analysis of breakout occurrence, variation of breakout orientation and fracture characteristics. We infer the impact of fracture networks on the development of breakouts from detailed analysis of 1221 borehole elongation pairs in the vicinity of 1871 natural fractures observed in the crystalline section of the GPK4 well of the Soultz-sous-Forêts geothermal field (France). Breakout orientation anomalies are found to concentrate in the immediate vicinity of fault cores and to decrease with distance to the fault core. Patterns of breakout orientation in the vicinity of natural fractures suggest that the breakout rotation, relative to the mean  $S_{\text{hmin}}$  direction, is strongly influenced by the fracture orientation. Even a direct relationship between fracture and breakout orientations is found in some depth intervals. In highly fractured zones, with different fracture families present, breakout orientations are especially heterogeneous, resulting from the overlapping effects of the fracture network. Additionally, breakouts are typically found to be asymmetrical in zones with high fracture density. Borehole breakout heterogeneities do not seem to be related to the principal stress heterogeneity only, but also to the effect of mechanical heterogeneities like weak zones with different elastic moduli, rock strength and fracture patterns. Consequently, care has to be taken when inferring the principal stress orientation from borehole breakout data observed in fractured rock.

### 3.1 Introduction

---

To ensure wellbore stability is one of major problems for drilling in hydrocarbon and geothermal industries, depending on the state of stress and the rock strength [Moos *et al.*, 2003a]. The present day state of stress has a key influence on fluid flow through fractured geo-reservoirs. For example, hydraulically active fractures tend to be critically stressed in the contemporary stress field [Barton *et al.*, 1995]. Current investigations of stress orientations and magnitudes are based on various methods including analysis of hydraulic fracturing, borehole breakouts [Bell and Gough, 1979], drilling induced tensile fractures (DITF), focal mechanism inversion and many others.

Borehole breakouts are cross-sectional elongations in the minimum horizontal stress direction, which are caused by localized failure around a borehole due to stress concentrations [Zheng *et al.*, 1989; Zoback *et al.*, 1985]. Breakouts are one of the direct indicators of the contemporary tectonic stress field [Heidbach *et al.*, 2008]. However, breakout orientations can vary and differ from the mean minimum horizontal stress orientation. We call these localized breakout orientations which differ significantly from the mean minimum horizontal stress “orientation anomalies”. Those orientation anomalies are commonly observed in the vicinity of fracture zones [Barton and Zoback, 1994].

Paillet and Kim [1987] suggested that slip on active faults penetrated by boreholes was the source of breakout anomalies. Barton and Zoback [1994], Shamir [1990] and Shamir and Zoback [1992] compute the local stress perturbation in the vicinity of fractures, which is required to distort the breakout orientation based on slip on the fault plane. In their studies near complete stress drop on the fracture plane (around 26 MPa at 5400 m depth) is required to match the observed breakout orientation anomalies by this model.

In this paper we consider the changes in mechanical properties affecting the breakout orientation, in particular in the Young's modulus and the Poisson's ratio, induced by the high microcrack density of the fault zone. Fault zones have a high microcrack density near the fault core. This microcrack density decreases exponentially with distance from the fault core [Janssen *et al.*, 2001; Vermilye and Scholz, 1998]. Changes of rock mechanical parameters due to changing crack density could lead to local heterogeneous zones around the fault core [Heap and Faulkner, 2008; Heap *et al.*, 2010]. Faulkner *et al.* [2006] showed that crack density influences the elastic properties of rock and, hence, the stress state of surrounding faults. Furthermore, they found that the mean stress as well as the magnitude of the highest principal stress decrease and the least principal stress increase as the fault core is approached, resulting in overall decrease in the differential stress. Thus, the breakout orientation anomalies might also be attributed to varying crack density. Zang *et al.* [1989] investigated the petrophysical properties of drill cores of the Continental Deep Drilling Program (KTB) and the relation of foliation, microcrack and stress anisotropy.

Valley [2007] analyzed breakouts and drilling-induced tensile fracture (DITF) patterns in two 5 km deep wells of the enhanced geothermal system in Soultz-sous-Forêts (France). He clearly identified a breakout orientation rotation by  $50^\circ$  with a wavelength of about 250 m in the vicinity of a fracture zone supposed to be 400 m in width and length intersecting the well [Sausse *et al.*, 2010]. However, the origin of this deviation remains unclear. He suggests that it might be related to fracture zones that intersect the wells or to lithology changes. In other publications, it is also suggested that such heterogeneity might also be related to lithology changes [Teufel, 1991], or to fluid pressure [Chang and Haimson, 2006]. Crack closure pressures have been examined by Zang *et al.* [1996] using ultrasonic P-wave velocities and helped to identify the SH orientation at the KTB site in addition to breakout investigation by Mastin *et al.* [1991].

Following the work from Valley [2007], details of stress perturbations associated with small natural fractures, not only with major fracture zones, are studied for a better understanding of the impact of the natural fracture network on breakout heterogeneities in granite rock. Herein, we first identify all faults and fractures accompanied by stress-induced breakouts in the crystalline section of the GPK4 well at the Soultz-sous-Forêts geothermal field. Then, we investigate the possible relationship between the breakouts and the mechanical perturbation due to the presence of faults and fractures. We outlined the influence of fracture density to the material heterogeneity, inferred from the detailed analysis of breakout shape. Furthermore, the importance of material heterogeneity resulting from fracture occurrence to breakout development is examined.

## 3.2 State of stress in the Soultz-sous-Forêts geothermal field

### 3.2.1 Geological context

The Upper Rhine Graben (URG) forms the central part of the European Cenozoic rift system, which consists of a rift-related sedimentary basin bounded by the Rhenish Massif and Vogelsberg volcano in the north and the frontal thrust of Jura Mountains in the south [Ziegler, 1994]. Major faults in the intra-graben and the shoulder areas, which were derived mainly from 2D seismic interpretation [Peters, 2007], are shown in **Figure 3.1**

The intra-graben faults predominantly strike in  $N10^\circ E$  direction parallel to the main border faults, whereas faults in the shoulder areas are bimodal with a main strike orientation towards  $N45^\circ E$  and  $N115^\circ E$ . These fracture trends are known as the Variscan and Hercynian, respectively. The kinematics of the intra-graben faults is predominantly extensional [Cardozo and Behrmann, 2006; Ford *et al.*, 2007], which suggests that the current maximum principal horizontal stress is oriented parallel to the orientation of those faults (NNE). This is confirmed by the world stress map on a regional scale [Heidbach *et al.*, 2008]. Furthermore, it is suggested that the stress regime in the URG varies from normal faulting in the northern part to strike slip faulting in the south [Larroque *et al.*, 1987; Rotstein and Schaming, 2011].

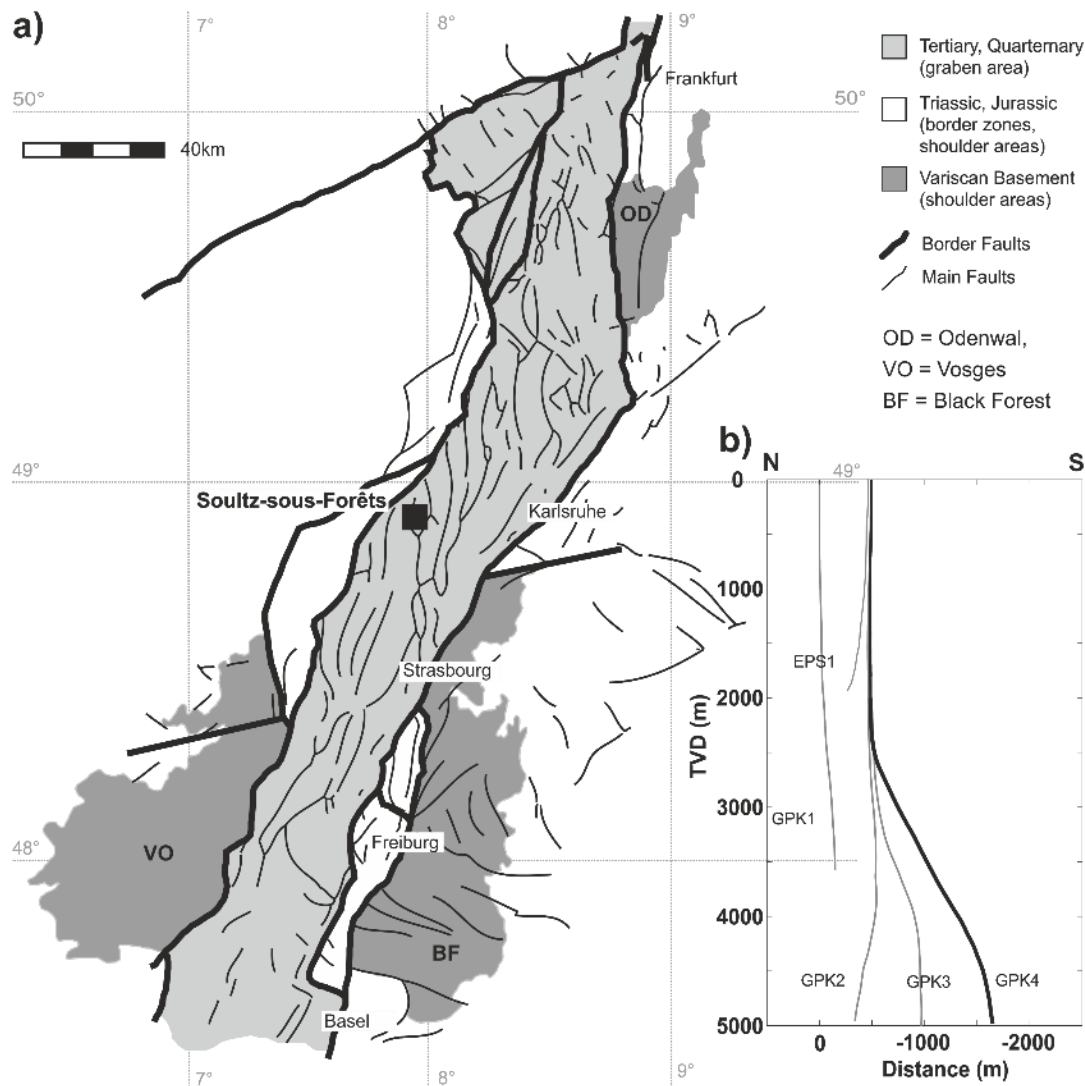


**Figure 3.1:** a) Geological map and major fault map of the Upper Rhine Graben rift system modified from Peters (2007). b). N-S cross section of the five wells in the Soultz-sous-Forêts geothermal field.

Soultz-sous-Forêts is located in the URG and hosts a deep Enhanced Geothermal System (EGS) test site (**Figure 3.1.a**). Its reservoir is in crystalline rocks which are characterized by low matrix porosity. Natural and forced fluid circulation takes place through the fracture network. At its current state of development, the EGS consists of five boreholes, including three deep wells which extend to more than 5000 m depth (**Figure 3.1.b**). More information about the Soultz-sous-Forêts EGS can be found in Gérard *et al.* [2006].

In-situ stress orientation and magnitude of the Soultz-sous-Forêts geothermal field were inferred from borehole log and hydraulic methods in previous studies. Cornet *et al.* [2007] reviewed various reports and analyses on hydraulic tests, borehole images and induced seismicity. Furthermore, breakouts and drilling-induced tensile fracture (DITF) patterns in GPK3 and GPK4 were analyzed by Valley [2007]. In

general, the mean maximum horizontal stress orientation values fall within the range of N164°E to 185°E.

The natural fracture data of the GPK4 well used in this study were obtained from the French Geological Survey (BRGM) on the GPK4 image logs. Azimuth and dip angle were determined for a total of 1871 fractures along the depth range between 2800 and 5000 m TVD. It can be summarized that most of the fractures appear to be members of a nearly vertical system of a conjugated fracture set with a symmetry axis striking NNW-SSE.

In addition to the BRGM dataset, major fracture zones derived from the geological analysis, induced microseismicity and vertical seismic profiles modeled by *Dezayes et al.* [2010] and *Sausse et al.* [2010] are also incorporated in this analysis. Their notations derived from measured depth are used throughout this study. All fractures and breakouts are presented in TVD (True Vertical Depth), as a result of which the depth of the major fractures plotted in the figure might differ from the depth indicated by their name. Hereinafter, all the natural fractures observed on borehole images and the modeled major structures will be referred to as fractures and fracture zones, respectively.

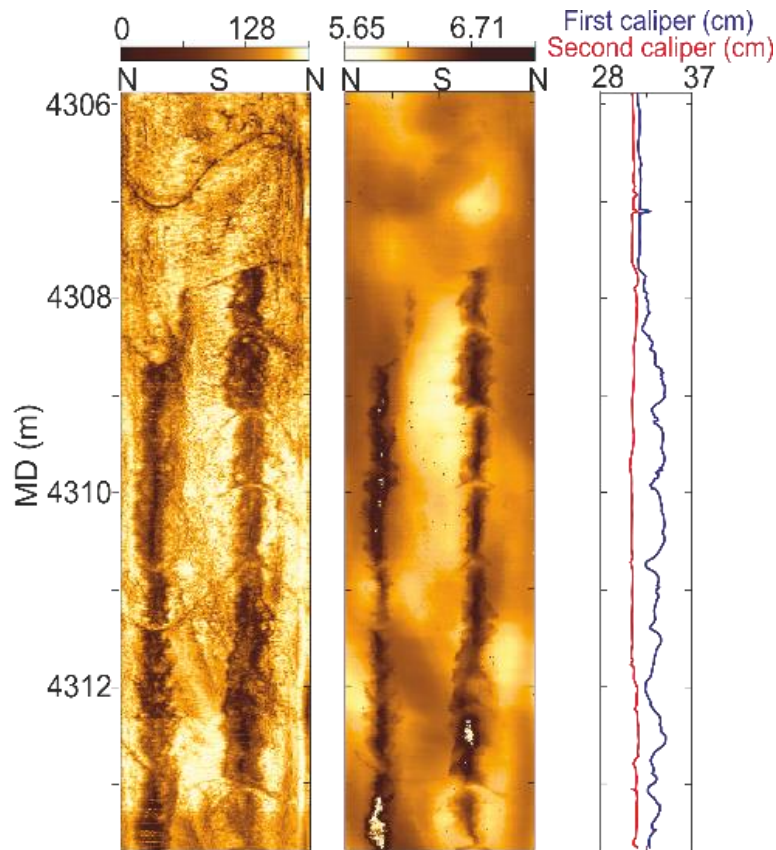
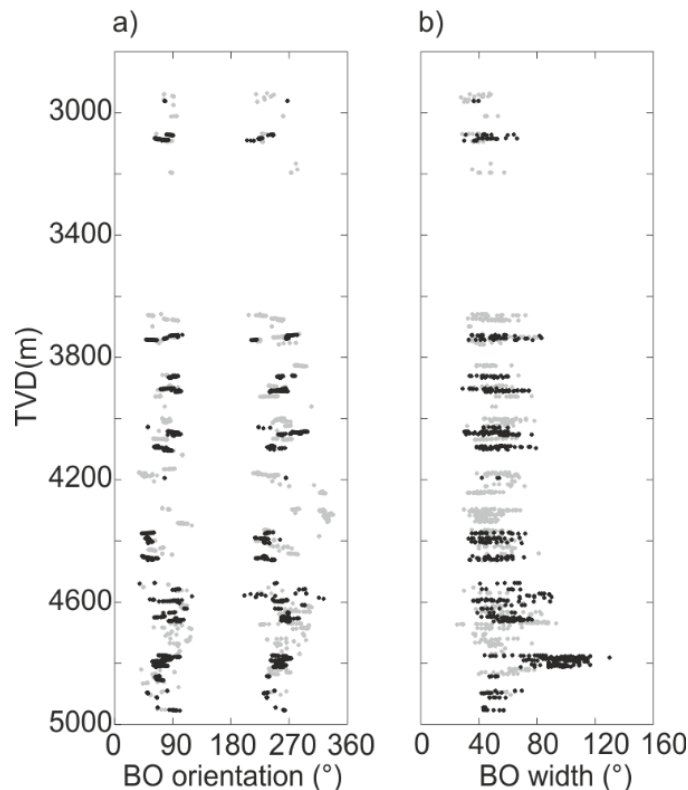


**Figure 3.2:** Typical breakout observed in UBI images. Breakouts appear as pair of broad zones of low amplitude (dark zones) on the amplitude log (left) and increased borehole radius (dark zones) on opposite sides of the borehole on the travel time log (mid). Caliper data were also used to measure the depth of the borehole elongation (right).

### 3.2.2 Principal horizontal stress orientation inferred from breakout observation

To identify breakouts, we examined the high-quality acoustic borehole televiewer (UBI) log that was run in the granite section of the deep well GPK4. GPK4 is the most deviated well in the Soultz-sous-Forêts geothermal field, its deviation from vertical exceeds  $15^\circ$  in the depth range of 2490–4740 mTVD and reaches a maximum deviation of  $35^\circ$  at 4220 m depth. The UBI tool provides detailed images of the ultrasonic reflectivity of the borehole wall along with the borehole geometry at an angular resolution of  $2^\circ$  inferred from the travel time. The logs were acquired in two runs 15 hours and 18 hours after the completion of drilling, respectively. Hence, the effect of time-dependent breakout growth [Schoenball *et al.*, 2014b] was probably still insignificant.

On the UBI image, breakouts appear as broad zones of increased borehole radius on the travel time log and low amplitude on opposite sides of the borehole on the amplitude log. Typical breakouts observed on the UBI image are shown in **Figure 3.2**. Median filtering with a kernel half width of 7 samples (corresponding to  $14^\circ$ ) was applied to remove noise in the image data through a one-dimensional linear filter. Stress-induced borehole elongations are not always observed symmetrically in opposite directions. In some cases, they might be confused with key seat or washout phenomena [Plumb and Hickman, 1985]. Elongation pairs separated by at least  $130^\circ$  with an increase of the borehole radius of more than 2% were picked as breakouts.



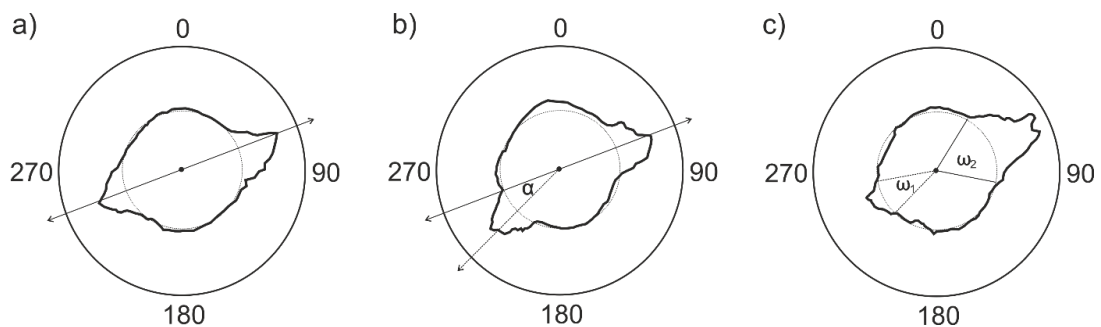
**Figure 3.3:** Stress-induced borehole elongation observations from the GPK4 UBI log. a) Breakout orientations. b) Breakout widths. Black and gray circles denote high and low confidence intervals, respectively.



Figure 3.3 shows an overview of the borehole breakout observation as discussed subsequently. Breakouts were observed starting at a depth of 2900 mTVD. The orientation and width of borehole elongation trends seen on UBI images were then measured every 20 cm. Both sides of the breakouts were picked. A total of 1221 borehole elongation pairs were identified. Each elongation pair is then considered an individual breakout with a uniform length of 20 cm. This approach enabled us to examine the detailed breakout shape on both sides and its correlation with the occurrence of fractures.

Two breakout data qualities were distinguished. Good breakouts picked from good quality image data are drawn in black. On average, they have picking uncertainty of  $5^\circ$  and  $8^\circ$  in orientation and width, respectively. Gray dots indicate lower quality that is mainly due to logging artefacts or intersections with a dense fracture zone, which made the selection of the breakouts more difficult. Consequently, they have a higher uncertainty of  $8^\circ$  and  $10^\circ$  for orientation and width, respectively (Figure 3.3). The high quality breakouts are then given double weights for the following analyses.

Most breakout widths are less than  $110^\circ$ , with 90% of the values lying in the range of  $38^\circ$ - $97^\circ$ , although wider breakouts were observed in some depth intervals (Figure 3.3.b). The breakouts reveal that the average orientation of the minimum horizontal stress (ASH) is  $N78^\circ \pm 17^\circ E$ . This result is in agreement with the results obtained in previous studies [Cornet *et al.*, 2007; Valley, 2007].



**Figure 3.4:** Typical breakout shapes observed on the GPK4 UBI log. a) Ideal symmetrical shape with a pair of identical elongations in opposite directions. b) One elongation side is shifted by  $\alpha$  from its ideal orientation. c) The elongations concentrated on one side only. As a result, one side has a wider and deeper elongation than the other.

### 3.2.3 Detailed breakout shape analysis and its correlation with fracture densities

Obviously, stress-induced borehole elongations are not distributed homogeneously along the depth, e.g. no breakouts were observed in the interval 3400-3600 mTVD depth and substantially higher numbers of breakouts were observed in the sections several hundred meters above and below. Additionally, breakouts were also observed to be asymmetrically formed. A detailed analysis of the breakout shape was conducted to gain more insight into material heterogeneities in the vicinity of the borehole. It was supposed that the intersection between fractures and the borehole might create damaged zones at the borehole wall which modify the geo-mechanical

properties. Especially the Young's modulus of such damaged zones should decrease when approaching the fracture core and the breakout elongation might rather develop towards the damaged weak zones. Hence, the final breakout might be perturbed from its ideal symmetrical shape as proposed for a homogeneous isotropic material (Figure 3.4).

To investigate this assumption, the orientation deviations  $a$  and width differences  $\Delta\omega = |\omega_1 - \omega_2|$  (Figure 3.4) were calculated for each breakout pair. Mean filtering with a moving window of 5 m was applied to smooth the profiles. Breakouts which have low orientation deviation  $a$  tend to have low width difference  $\Delta\omega$ , and vice versa. The orientation and width differences are found to be up to  $37^\circ$  and  $18^\circ$ , respectively (Figure 3.5.c and d).

The intersection of the fracture with the borehole will create a weak zone which might be a preferred location for breakout to develop. The upper and lower intersections of the fracture with the well, however, are separated by a distance depending on the fracture inclination. Here, a single fracture might only affect one side of the breakout at a particular depth. This effect will be amplified in a high fracture density zone, hence the most dense and asymmetric breakouts are observed in the high fracture density zone.

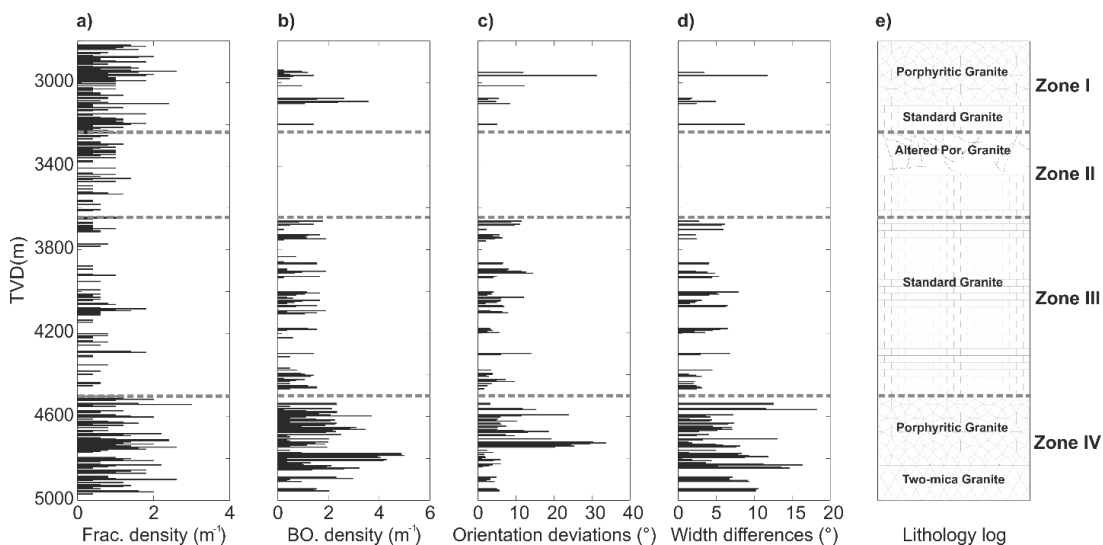


**Figure 3.5:** Results of the detailed breakout shape analysis and its correlation with lithology and the occurrence of fracture intersecting borehole. a) Fracture density. b) Breakout density. c) Breakout orientation deviations from its ideal opposite direction. d) Width differences of the pair elongation. e) Lithology log. Four zones were distinguished based on the occurrence of breakouts and their detailed shape and with comparison of fracture occurrence.

A crossplot of breakout density and fracture density (Figure 3.6) shows a clustering of breakout-fracture pairs consistent with four depth zones. These zones are consistent also with breakout asymmetry (Figure 3.5) and the petrographic model of the Soultz-sous-Forêts geothermal field by Hooijkaas *et al.* [2006]. In a simplified



manner, four different zones of breakout and fracture occurrence can be distinguished:

Zone I: This uppermost zone from 2900 to 3200 mTVD has a high fracture density of about 0.48 to 1.8 m<sup>-1</sup>, but the breakout density is low. This zone consists of massive porphyritic granite which is highly fractured and hydrothermally altered.

Zone II: Zone without breakouts between 3200 and 3600 mTVD. No further analysis was conducted for this section. This zone is characterized by a rather low fracture density and dominated by altered porphyritic granite section. In this altered granite section the borehole image quality is very poor and did not allow for breakout analysis.

Zone III: The middle zone between 3600 and 4500 mTVD is characterized by small fracture densities and breakout occurrences. Breakout pair orientation deviation and width difference also are quite small in this zone. In this depth interval, the granite is less fractured and is very rich in biotite and amphibole.

Zone IV: The lowermost part zone from 4500 to 5000 mTVD is characterized by a high density of both fractures and breakouts, up to 2.3 m<sup>-1</sup> and breakouts were observed continuously over several tens of meters. A younger, fine-grained, two-mica and amphibole-rich granite that intrudes into the porphyritic granites is predominating in this zone.

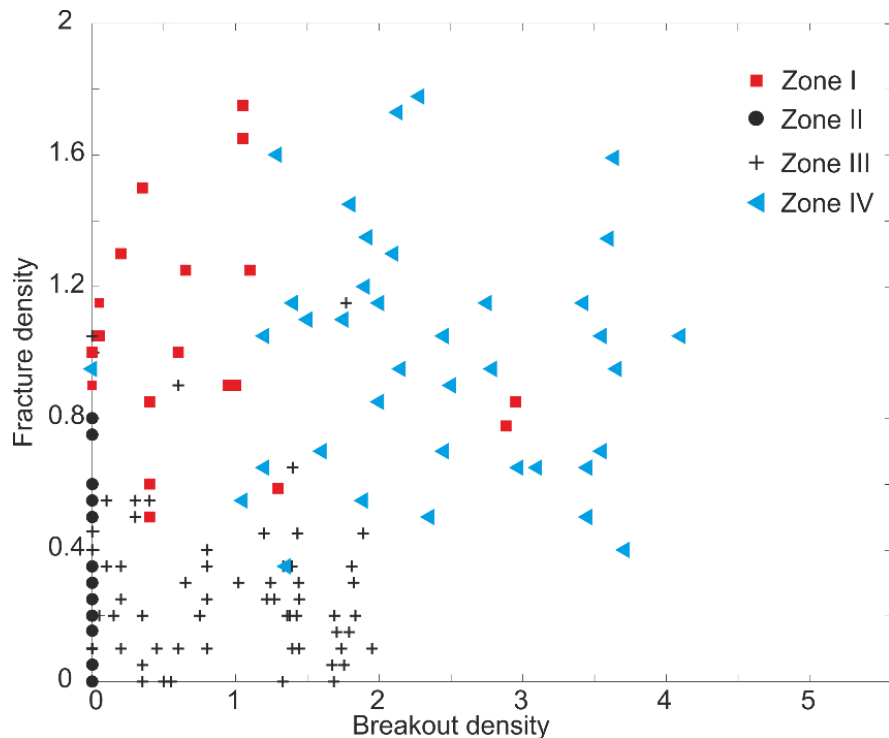


**Figure 3.6:** Crossplot between fracture density and breakout density observed in the crystalline section of the GPK4 well.

### 3.3 Breakout heterogeneity and its connection with fracture networks —

The origin of the breakout orientation heterogeneities shall be analyzed in the present section. *Mastin* [1988] found that breakout orientation is rotated away from the direction of the minimum horizontal stress, as the borehole deviates from the direction of the sub-vertical principal stress. He calculated the minimum value of borehole deviation (critical angle) for all borehole azimuths to rotate the breakout orientation by  $10^\circ$ . Considering the stress magnitude analyses of *Valley* [2007] and *Cornet et al.* [2007] who find the stress regime to be a transitional strike slip to normal faulting, the critical deviation angle for a breakout rotation by more than  $10^\circ$  is around  $35^\circ$ , which corresponds to the maximum deviation of GPK4 well. Hence, breakouts might be rotated by a maximum of  $10^\circ$  from ASh due to well inclination. The rotations observed in GPK4 well, however, showed much higher values. Consequently, it can be concluded that this is not the sole effect of borehole deviation.

Systematic or abrupt breakout orientation rotations were frequently observed in the intersection zone of fractures with the GPK4 borehole wall. Furthermore, shapes of breakouts were found to be the most asymmetric in the zone of the highest fracture density (below 4500 mTVD). When assuming the reservoir to be composed of homogeneous granite, it is reasonable to assume that the source of breakout heterogeneities is the occurrence of weak zones in the vicinity of fractures.

By analyzing the perturbation of breakout orientations in the vicinity of fracture, two main questions regarding the role of fractures shall be answered: Are there patterns of breakout orientation in the vicinity of fractures? What is the main factor that controls the breakout orientation rotation? Breakout analyses are performed in the vicinity of both fracture zones and fractures.

#### 3.3.1 Influence of fracture zones

It was observed in several fields that the principal horizontal stress orientations varies with depth [*Barton and Zoback, 1994; Paillet and Kim, 1987*]. In the following, we investigate the large-scale breakout orientation rotation trend with depth and its correlation with fracture zones. The whole survey depth range was divided into 10 sub-ranges according to the occurrence or lack of breakouts, their orientation variations, and also considering the intersection with fracture zones. All fracture zones used in this analysis have length and width of more than 300 m [*Sausse et al., 2010*].

**Figure 3.7** shows the one-sided breakout plot of the breakout orientation with depth. This is the averaged orientation of both borehole elongations in each pair shown in **Figure 3.3.a**, plotted in  $N0^\circ$ - $180^\circ E$  half-circle. The azimuthal deviations represented in each box plot can be considered as including measurement errors, local heterogeneities and variations of the stress orientation.

The median orientations of the breakout groups above 4150 mTVD are consistent with the ASh orientation. In this depth range, only a low to medium density of fracture ( $0.43m^{-1}$ ) and one fracture zone are observed. A long section of absence of breakouts is observed between 3230 and 3600 mTVD. DITF are also absent in this

depth interval [Valley, 2007]. Below this section, the FZ-3940 fracture zone is found at 3770 mTVD. Although the median orientation of breakouts is consistent with ASH, breakouts are found to be heterogeneously oriented in the vicinity of the fracture zone. The 1<sup>st</sup> and 3<sup>rd</sup> quartiles of the breakout orientations are N60°E and N100°E, respectively. Damage area surrounding the fracture core might be the source of these large heterogeneities of breakout orientation.

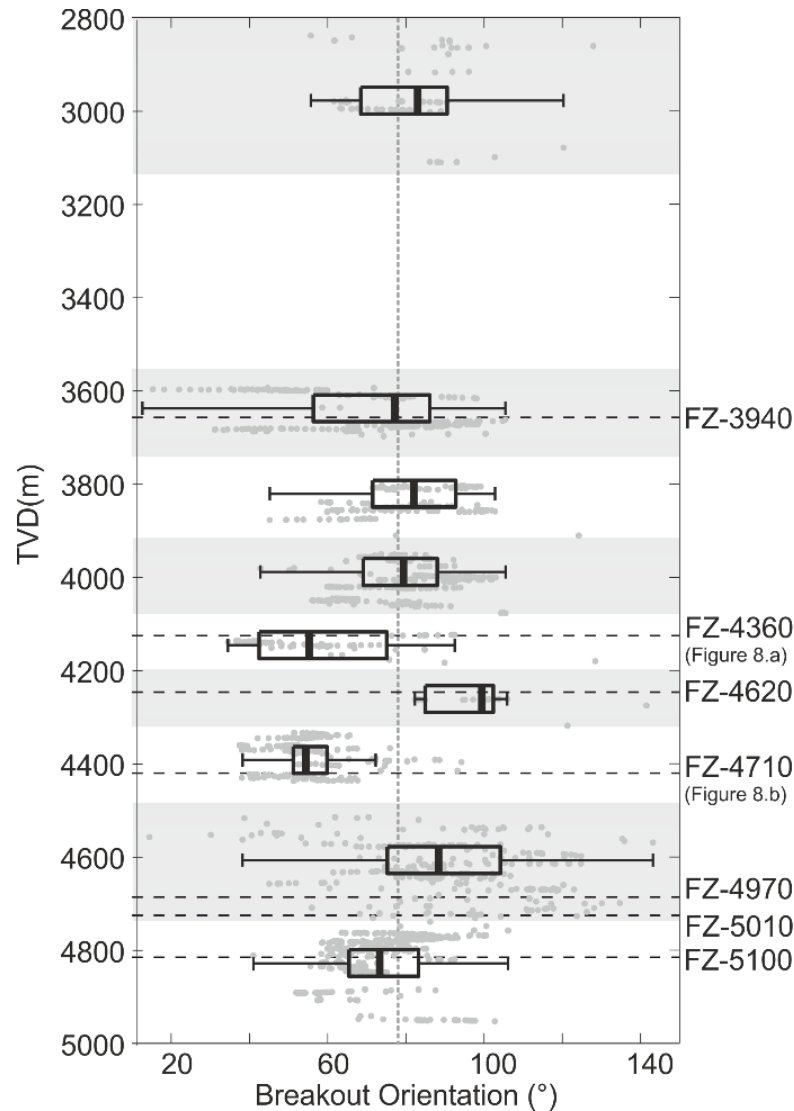


**Figure 3.7:** Profile of breakout orientations in the GPK4 well. Box plots are used to summarize the distribution of depth intervals. The lower and upper fences, the 1<sup>st</sup> and 3<sup>rd</sup> quartiles (rectangle) as well as the median value are plotted. The depths of the intersected major fractures are indicated by dashed lines.

In the vicinity of the fracture zone FZ-4360, most of the observed breakout orientations are rotated from ASH in counterclockwise direction. The median is found to be deviated by 13° (Figure 3.7). A closer look at the breakouts orientation in the vicinity of FZ-4360 is shown in Figure 3.8.a. The distribution of the breakout orientation above the fracture (from 4090 mTVD) and below it (up to 4185 mTVD)

follows a sinusoidal curve with its highest shift at depth of the fracture core. Above the fracture, the breakout orientations increase from  $-27$  to  $22^\circ$  relative to ASh; and below the orientations decrease to  $-40^\circ$ . Overall an orientation variation of about  $60^\circ$  is observed. However, breakouts were absent in the vicinity of FZ-4360 fracture core. Such a breakout absent zone was also observed in several other fields, e.g. *Barton and Zoback* [1994; *Lin et al.*]. The role of the FZ-4360 fracture zone seems to prevent breakout formation in its vicinity. This suggests that the magnitude of the differential stresses is reduced in the immediate vicinity of FZ-4360. Possible mechanisms are plasticity or creep [*Sibson, 1977*] [1977].

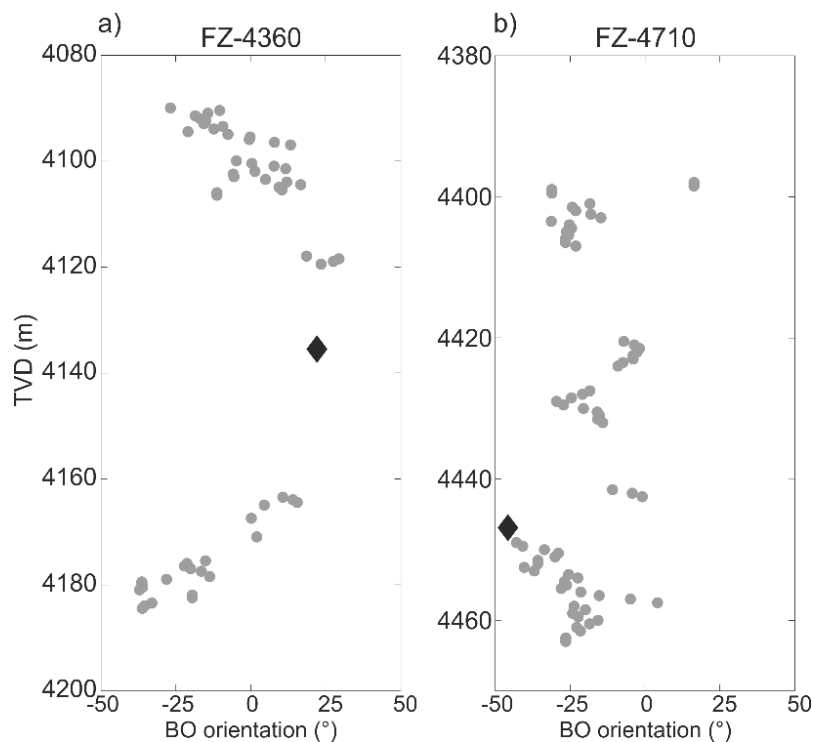


**Figure 3.8:** Breakout orientation profile with depth around three fracture zones: a) FZ-4360, and b) FZ-4710. Gray dots indicate borehole breakout orientations, black diamond display the fracture zones dip direction. All orientations are plotted relative to ASh.

Only few breakouts are observed in the vicinity of FZ-4620. All those breakouts are oriented toward clockwise direction from ASh (**Figure 3.7**). FZ-4710 is found around 80 m below FZ-4620. This fracture zone is a Hercynian fracture and intersecting the GPK4 well with the lowest inclination [*Ziegler, 1994; Hurd and Zoback, 2012*]. Numerous breakouts were observed in its vicinity, and almost all of them (96%) are shifted counterclockwise from ASh. Interestingly, FZ-4710 is also dipping toward counterclockwise direction relative to ASh. The parallel orientation of both major fracture dip azimuth and breakout orientation was also observed for FZ-4620. Breakout patterns in the vicinity of both major fracture zones suggest that breakout orientation, in a low to moderate fracture density zone, were rotated from ASh to a preferred direction which might be controlled by its dip azimuth.

A closer look at the breakout patterns in the vicinity of FZ-4710 is shown in **Figure 3.8.b**. Around the fracture zone, breakouts have the highest orientation rotation at the fault core. Breakout orientation trends were dominated by negative shifts. It is obvious that the fault initiated the breakout, starting from the borehole elongation towards the azimuth of the fault dip (clockwise 46° deviation) and gradually returns to ASH with increasing distance from the fault core. The two distinct breakout patterns in the vicinity of FZ-4360 and FZ-4710 fracture zones suggest the role of fracture zones in breakout heterogeneity, either in preventing breakout occurrence or rotating their orientation.

Three fracture zones and a large number of fractures are observed in the deepest two sub-ranges. Hence, it is not surprising that the most heterogeneous breakout orientation zones are found in this part. Additionally, it is also shown that an enhanced presence of fractures correlates well with an enhanced occurrence of breakouts. For example the depth interval of 4700 – 4830 mTVD has the highest density of fractures intersecting the well and also the most densely observed breakouts.

### **3.3.2 Influences of natural fractures**

A detailed observation of the breakout orientation in the vicinity minor fractures was performed to gain a better understanding of the relationship between breakouts and fracture orientation. Breakouts were found in the vicinity of 25% of fractures found in GPK4. Only those fractures accompanied by stress-induced borehole breakouts were selected for further analysis.

Cross-plots of fracture dip direction and average breakout orientation observed 3 m around each fracture was made (**Figure 3.9**). Both breakout and fracture orientations are plotted relative to ASH. The orientation deviations of both parameters are expressed in either clockwise (positive) or counterclockwise (negative) deviation. The purpose was to determine the deviation of breakout orientation and its correlation with the orientation of the fractures intersecting the borehole.

The correlation coefficient was calculated to measure the statistical relationship between those sets of orientation data. As the coefficient approaches zero, there is no correlation between fracture and breakout orientation. The closer it is to either -1 or 1, the stronger is the correlation between the variables.

**Figure 3.9.a** shows the cross-plot for the entire GPK4 well. Several breakout-fracture pairs are oriented towards ASH orientation. These breakout-fracture pairs fall in the gray area. The orientation of those breakouts is consistent with the ASH orientation. This indicates that the stress state remains mostly constant around those fractures.

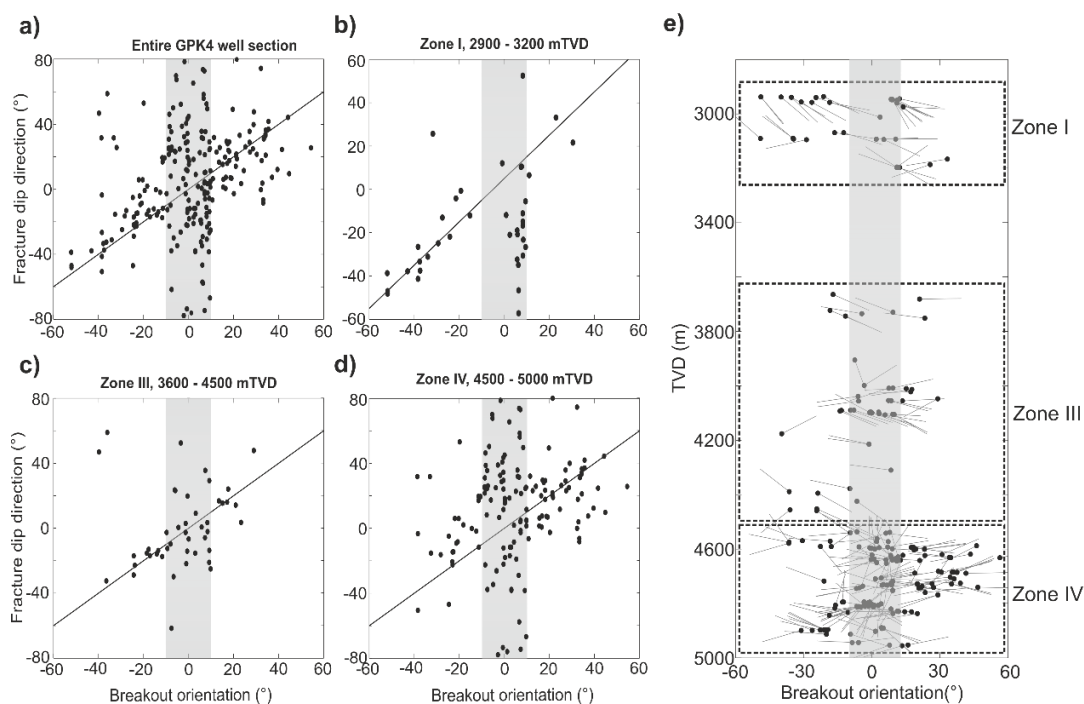


**Figure 3.9:** Cross-plot between fracture dip directions and averaged breakout orientations observed in the vicinities of fractures in (a) the entire GPK4 well, (b) zone I, (c) zone III and (d) zone IV. The gray area indicates the unperturbed breakouts orientation. (e) Tadpoles of breakout orientation to the fracture direction of each breakout-fracture pair versus TVD. Zero for all orientation axes is the ASh.

However, breakout orientations in the vicinity of many other fractures are found to be rotated from ASh by up to  $60^\circ$ . Hence, two breakout orientation trends in the vicinity of natural fractures can be distinguished in this plot. First, breakouts oriented about ASh and second, breakouts oriented more than  $10^\circ$  off from ASh. Only those fractures accompanied by breakouts deviated by more than  $10^\circ$  from ASh are used in this analysis. The threshold of  $10^\circ$  was used to consider the effect of borehole deviation on the breakout orientation and breakout picking uncertainties.

The black diagonal in the crossplots indicates a breakout orientation parallel to the fracture dip direction. In general, those breakout- fracture pairs are found very close to this trend, with a standard deviation of the azimuth of  $17^\circ$ . The correlation coefficient between both orientations is 0.6. This value indicates that there is distinct correlation between the breakout orientation rotation and the fracture orientation.

More detailed analysis of breakout-fracture pairs is conducted for the four different zones described in chapter 2.3 to analyze the correlation in each zone. The correlation between fractures and breakout orientations is very pronounced in the first zone (Figure 3.9.b). Here, breakout orientation rotations are dominated by counterclockwise deviation from ASh with a maximum shift of  $48^\circ$ . The pairs of breakouts and fractures are scattered along the black diagonal, indicating a direct relation, with a standard deviation of only  $7^\circ$ . This strong correlation is also reflected by a high correlation coefficient of 0.90. Interestingly, only one fracture family is present in this section, with all fractures dipping in similar directions.

A good correlation coefficient of 0.83 was obtained in the third zone (**Figure 3.9.c**). Around 50% of the fractures accompanied by breakouts in this zone were related to their surrounding breakout orientation deviation. Clockwise and counterclockwise deviations of up to 40° and 30°, respectively, were observed.

Such a strong connection was not observed in the fourth zone (**Figure 3.9.d**). Here, only a low correlation coefficient of 0.32 was obtained for breakout orientation in the vicinity of fractures. This is probably due to the high density of fractures observed in this zone. As observed in the previous studies e.g. *Heidbach et al.* [2008] and *Lin et al.* [2010], the breakout azimuths varies significantly on length scales of few centimeters to hundreds of meters as a function of depth along the well bore. Given the averaged distance between the fractures in this zone (3.9 m), it is reasonable to assume that the perturbation effect of one fracture might overlap with that of the neighboring fractures. Therefore no good correlation was observed in this zone.

Although the upper zone also has a high fracture density, the overlapping effect seems not to be dominant. This suggests that the overlapping effect is not only due to the high density of fractures. As the breakout orientation perturbation is affected strongly by the fracture orientation, it is reasonable to assume that it might be also due to the fracture network orientation. The upper zone has fractures which are uniformly dipping counterclockwise relative to ASh (**Figure 3.9.e**). In such a case, the overlapping effect still occurs, but breakouts are rotated consistently toward the same direction. Hence a good correlation can be achieved. The lower zone is not only highly fractured but the fractures are also heterogeneously oriented. As a result, the breakout-fracture orientation plot exhibits scattering with a very weak correlation. This shows the importance of fracture density and of their orientation on breakout orientation perturbations.

### 3.4 Discussions

---

The effect of fractures on the mechanical properties of rock was analyzed in many studies. In-situ laboratory measurements on Soultz-sous-Forêts granite [*Valley, 2007*] revealed the effect of fractures on rock mechanical parameters. Young's modulus of intact Soultz-sous-Forêts granite was determined to be around 54 GPa, but only 39 GPa for significantly fractured granite. Furthermore, the uniaxial compressive strength is also found to decrease with increasing fracture density [*Alm et al., 1985*]. Due to the reduction of rock strength, breakout is expected to develop more easily. Hence, a good correlation between the density of fractures intersecting the well and observed breakouts could be expected.

If a fault zone has an associated fractures damaged zone, the stresses are expected to be perturbed and rotated depending on the change in elastic properties of the damaged material. As the fault core bears the most damage, the stress perturbation is assumed to be concentrated in that zone and to decrease with distance. Breakouts will then develop according to this local stress perturbation. In such a case, a gradual breakout orientation rotation centered at the fault core is expected to result. This



gradual rotation trend starting from the fault core is observed well in the vicinity of GPK4-FZ4620 (Figure 3.8.b).

The dimensions of natural fractures are too small to induce local stress perturbations required to alter the breakouts orientation [Barton and Zoback, 1994]. Hence, we attribute the observed small wavelength breakout rotation in the vicinity of a natural fracture to the material heterogeneity due to the occurrence of weak zones in the vicinity of fractures. A conceptual model, supported by the strong correlation between breakout and fracture orientations in the first and second zones of the well, of the perturbed breakout shape in a heterogeneous material is shown in Figure 3.10. The weak zone is assumed to be the result of the increasing microcrack density in the fracture core. This typically reduces the stiffness (Young's modulus) and increases Poisson's ratio [Heap et al., 2010]. Furthermore, it has been shown that changes in elastic moduli can induce changes in the stress field [Heap and Faulkner, 2008]. Haimson [2007] showed that in an intact granite the breakout is initiated by the development of the microcracks subparallel to the maximum horizontal stress direction behind the borehole wall. In a heterogeneous material, such microcracks are already present in the weak zone. Hence, the perturbed breakout shape is then developing along this weak zone.

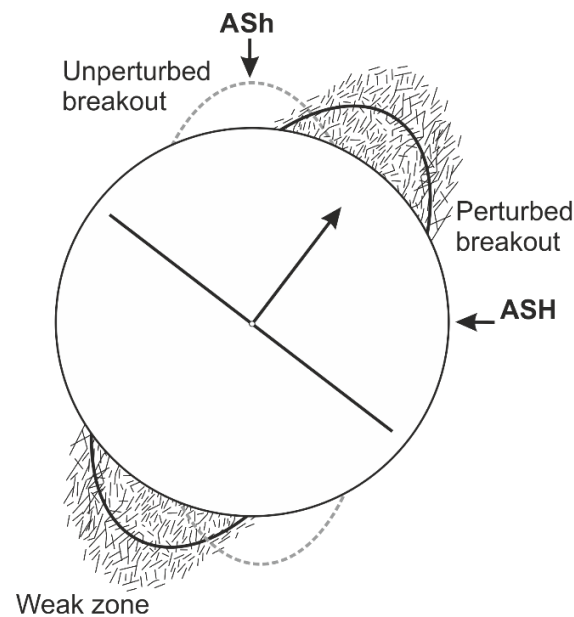


**Figure 3.10:** Sketch of the perturbed breakout shape in a heterogeneous material. The breakouts are rotated from the unperturbed breakouts (black elongations) toward the weak zone, i.e. weak zones are assumed to be the results of the intersection between natural fracture and borehole wall.

The different role of fractures in affecting breakout orientation was shown. Some fractures induce a breakout orientation rotation in their vicinity, while others do not. An attempt was made to distinguish those two different type of fractures based on



their orientation and dip angle. Fractures that perturbed breakout orientation in its vicinity have dip direction from N105°NE to N219°E and dip angles between 30° and 88°, which covers almost the entire range of all fractures observed in this well. Hence, no clear separation could be obtained.

Fractures that perturb the orientation of breakouts might have experienced slippage prior to drilling [Barton and Zoback, 1994], or different lithologies [Lin et al., 2010]. Another possibility is that those fractures significantly alters the mechanical material properties in the vicinity [Heap et al., 2010; Faulkner et al., 2006]. The latter is more probable, as laboratory measurements [Valley, 2007] also showed that the reduction of the rock strength due to fractures depends on its fracture filling mineral. Fractures with quartz sealing may be almost as strong as the intact rock, while sulfide sealed fractures show a rock strength reduction by almost 50%.

We also observe the importance of fracture inclination on breakout development. For nearly vertical fracture dipping, the top and bottom intersections of a single fracture with a borehole of 12.25 inch in diameter might be separated by a couple of meters. Here, fracture might only affect one side of the breakout at a particular depth. As a result asymmetrical shapes of breakouts will be expected. Furthermore, the overlapping effect of adjacent fractures might increase material heterogeneities, as the most asymmetric breakout shapes are observed in the high fracture density zone.

### 3.5 Conclusions

---

Analyzing detailed breakout heterogeneities and their correlation with fracture occurrence at great depth is a challenging task, in particular because of lacking information on in-situ material properties of fractured rock. While our determined mean direction of  $S_{\text{hmin}}$  agrees well with previous studies [Valley, 2007; Cornet et al., 2007], careful analysis shows that breakout orientations are systematically affected by the occurrence of fractures and fracture zones. We propose two different mechanisms for the breakout rotation in the vicinity of fracture zones and natural fractures. For breakouts around fracture zones, examples of systematic sinusoidal perturbations to breakout orientation, initiation and inhibition of breakout formation were presented. Therefore we conclude, that anomalies of breakout orientation in the vicinity of fracture zones reflect the large-scale stress heterogeneity caused by the fracture zones.

The analyzed well section was divided into four distinct sections, based on the correlation of breakout and natural fracture densities. It was shown that breakout occurrence, orientation, and shape symmetry are largely determined by the fracture network. Crossplots of breakout orientation and fracture dip direction reveal a direct correlation of both features. This correlation is highest for sections with only one fracture family present and is less in heterogeneous zones with high fracture density and several fracture families (Figure 3.9). Since Barton and Zoback [1994] found that natural fractures are too small to perturb the stress field even locally, the observed perturbations of breakout orientation cannot be explained by a perturbation of the stress field. However, the direct relation of fracture dip direction and breakout

orientation suggests that weak zones surrounding the fractures are causing the breakouts to form along the fracture dip directions. If slippage would perturb the stress field, no consistent correlation with fracture dip direction would be expected, since the slip direction would change according to the direction of maximum shear stress [Bott, 1959].

In the Fourth Zone, with a high fracture density the overlapping effects of several fracture families present reduces the correlation of fracture dip direction and breakout orientation. In this section we also observe the largest asymmetries, evidenced by different widths of opposite breakouts and also a distance between an elongation pair smaller than  $180^\circ$  along the borehole wall. We conclude that asymmetric breakouts are caused by the weak zones accompanying steeply dipping fractures, which are penetrated by the borehole over a length of up to several meters.

The results of this study provide a better understanding of stress-induced borehole elongations in fractured rocks. Careful analysis of breakouts can help us learn about the mechanical properties of fractures and their immediate surroundings. The impact of the fracture network on breakout heterogeneities is very pronounced in crystalline rock, which is mechanically isotropic. This is why we could attribute the perturbation of breakouts to the occurrence of fractures and accompanying alteration of mechanical properties only. Numerical modeling taking into account the elastic property changes as a result of fracturing and fracture filling is required to better quantify the phenomena observed in this study.

---

## Analysis of state of stress in a deep fractured crystalline rock

This chapter has been published as a conference proceeding in the World Geothermal Congress 2015 and is currently on-preparation for an international journal publication

### Abstract

The variations in mechanical properties, the fracture characteristics, and the inclination of the well may perturb the development of wellbore failures and, hence, affect the estimation of the stress state in fractured rocks. A detailed analysis of 1221 and 827 compressive, respectively tensile wellbore failures in a 3.5 km crystalline rock observed in the GPK4 well in Soultz-sous-Forêts enables us to analyze the different patterns of stress heterogeneities which may be related to several factors. The inclination of the well affects the stress distribution by a few MPa. This is found to have a significant effect on the development of the wellbore, i.e. the limitation of tensile failures in the part of the well which is inclined by less than  $10^\circ$ , and the delay of compressive-failure occurrence by about 700 m in a  $25^\circ$  inclined well. Fractures and alteration reduced the compressive strength of the crystalline rock by approximately 30% and, hence, promoted the development of breakout at a lower far-field stress. The orientation of wellbore failures in such fractured zones is found to be heterogeneously distributed and, hence, reduces the quality of stress estimation. Furthermore, the first and second order of stress heterogeneity patterns in the vicinity of major and minor fractures in a highly fractured zone at depths of 4600 to 4850 m are observed. The numerical modeling of the development of breakouts that takes into account the weak zone as a result of the fracturing process developed in this study shows a systematic analysis of the variation of the breakout orientation and the reduction of the mechanical properties. In fractured rock, wellbore failures do not correlate to the principal stress only, but also to the variation in the mechanical properties. Hence, a long continuous sequence of wellbore failures is a must to obtain sufficient stress-related failure data.

## 4.1 Introduction

---

In geosciences, knowledge of the current state of stress is the key component of a comprehensive mechanical model. The widespread use of wellbore imaging devices, e.g. ultrasonic borehole viewers [Zemanek *et al.*, 1970] and electrical imaging devices [Straub *et al.*, 1991] yields detailed information about wellbore failure that is critically important in assessing stress orientation and magnitude at depth. Drilling a well in a homogeneous isotropic material perturbs in-situ stress around the wellbore in a mathematically known way [Jaeger *et al.*, 2007; Kirsch, 1898]. In this case, it is possible to obtain information about both stress orientation and magnitude from knowledge of the occurrence and geometry of wellbore failures, especially if the well is deviated [Zoback *et al.*, 2003]. However, sufficient appraisal of the mechanical properties of the rock is required.

However, often wellbore failures deviated from the principal horizontal stress orientation. Paillet and Kim [1987] and Barton and Zoback [1994] suggested that slip on active faults penetrated by boreholes was the source of such wellbore failures deviation. Based on this assumption, a large stress drop and, consequently, large fault planes are required to sufficiently alter in-situ stress. Later study of Sahara *et al.* [2014] revealed that the rotation of the breakout orientations is also observed in the vicinity of minor fractures, which are too small to generate sufficient stress drop. They highlight impact of fracture networks on borehole breakout heterogeneities in crystalline rock. In other studies, it is also suggested that the stress heterogeneity might be related to lithology changes [Teufel, 1991] or to fluid pressure [Chang and Haimson, 2006].

Faulkner *et al.* [2006] showed that cracks influence the elastic properties of rock and, hence, the stress state of surrounding the damaged zone. In addition, the occurrence of clay might alter the reservoir mechanical properties [Sayers, 1994b]. These emphasize importance of the petrographical features in promoting the mechanical heterogeneity in the material and, hence, perturbing the orientation of wellbore failures. It has been long assumed that mechanical heterogeneities due to lithology, fractures and clay play an important role in the development of wellbore failures [Ewy and Cook, 1990; Haimson, 2007]. However, sound studies on the mechanical significance of those rock parameters on the estimation of in-situ reservoir stress state were missing.

A comprehensive study of the estimation of stress state that take into account petrographical rock parameters and well trajectory is performed in this study. Herein, we first identify all wellbore failures in 3.5 km crystalline section of the GPK4 well in the Soultz-sous-Forets geothermal field. Then, the orientation and magnitude of principal horizontal stresses and their heterogeneity are estimated from wellbore failures data. The mechanical properties of the crystalline rock used for stress inversion are determined from previous in-situ laboratory measurement [Valley, 2007] and sonic log [Genter and Tenzer, 1995] run in the GPK2 well. Petrographic log which was derived from integrated cutting data and various geophysical logs [Dezayes *et al.*, 2003; Dezayes *et al.*, 2005; Genter *et al.*, 1999] is used to extent the

mechanical information of the rock from the laboratory scale to the reservoir scale. The sources and patterns of the stress heterogeneity in the fractured granite section are then discussed. Subsequently, numerical modeling that takes into account the variation of mechanical properties caused by fractures is developed in this study to model the development of borehole breakout in heterogeneous material. The results of the observation and numerical modeling performed in this study explain the main parameters that affect the characteristic of the heterogeneities of wellbore failures in a fractured crystalline rock and give constraints in using them as a stress indicator.

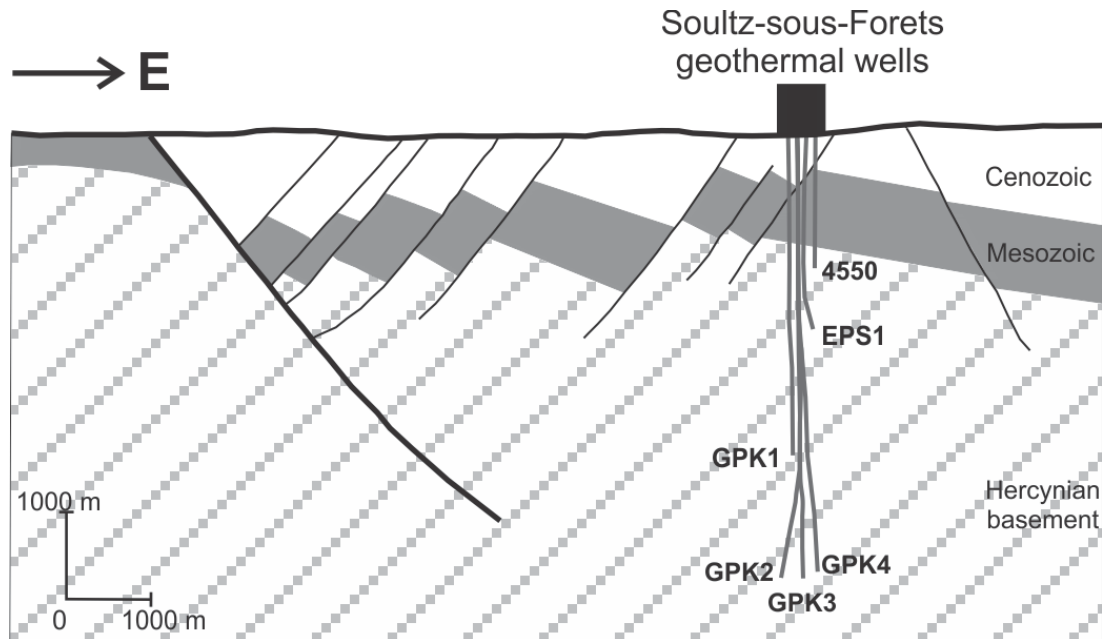


**Figure 4.1:** West-east cross-section through the Rhine Graben border and the Soultz-sous-Forêts site. Overview of the trajectories of five deep wells at Soultz-sous-Forêts is showed.

## 4.2 Soultz-sous-Forêts geothermal field

The Soultz-sous-Forêts enhanced geothermal system (EGS) field is located in the Upper Rhine Graben (URG). The high geothermal gradient of about  $100\text{ }^{\circ}\text{C}/\text{km}$  within the sedimentary cover results from deep hydrothermal convection loops within the fractured basement. The present targets for heat exploitation are the fractured granite at 4.5–5 km depth, where temperatures reach  $200\text{ }^{\circ}\text{C}$ . Five wells have been drilled and used to extract the heat in the granitic formation. Three of those wells are currently used for operation with two wells as injector (GPK3 and GPK4) and one producing well (GPK2) (**Figure 4.1**). In such a deep fractured reservoir, good knowledge of the stress field is essential for the optimization of borehole design [Moos *et al.*, 2003a], understanding of the flow distribution at depth [Barton *et al.*, 1995] and mitigation of the seismic risk due to induced seismicity [Gaucher *et al.*, 2015].

#### 4.2.1 Geological setting

Continuous coring was conducted in EPS1, providing 810 m of granite core for structural analysis and petrographic examination [Genter and Traineau, 1996]. In the other wells, however, only cutting samples were collected in the granite section and were used to realize a petrographic log. Geophysical measurements, i.e. caliper, spectral gamma ray and Ultrasonic Borehole Image (UBI) logs, were also carried out in the granite section and were analyzed in order to help to determine the lithology and the characteristics of the fractured zones.

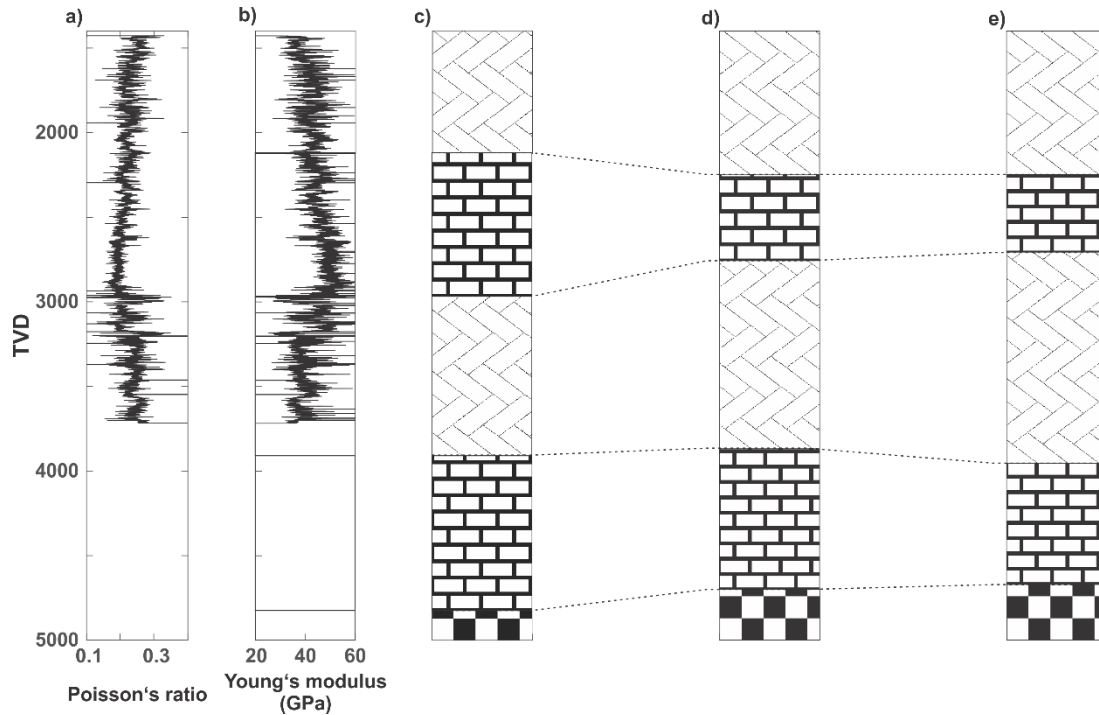


**Figure 4.2:** Dynamic Young's modulus (a) and Poisson's ratio (b) obtained from sonic log run in the upper section of the GPK2 well. The petrography log of the three deepest well in Soultz-sous-Forêts: GPK2 (c), GPK3 (d) and GPK4 (e).

Based on these integrated data obtained from boreholes, the main petrographic interpretation of the deep crystalline rock can be described as follows [Dezayes *et al.*, 2003; Dezayes *et al.*, 2005; Genter *et al.*, 1999; Genter and Tenzer, 1995] (**Figure 4.2**)

- From 1400 to 2100 m a porphyritic MFK-rich granite with fracturing, characterized by high average content of Th and U but low K content is observed
- The same granite but poorly fractured with moderate radioactive element content was penetrated from 2100 down to 3000 m.
- From 3000 to 4000 m the dominant lithology is the porphyritic MFK-rich granite but with a high intense fracturing and vein alteration and a high K-content. A lot of major fractured zones deduced from caliper data.
- From 4000 to 4700 the porphyritic MFK-rich granite shows low average content of the radioactive elements.

- From 4700 to the bottom depth, there are some petrographic variations with the MFK-rich granite and a younger two-mica granite.

It can be seen in **Figure 4.2** that the same lithology patterns are observed in all wells, however, the thickness of these lithologies varies among the deep wells, i.e. a thicker upper massive granite and thinner fractured zone in GPK2. This may be related to the faults that intersect the crystalline reservoir [Sausse *et al.*, 2010].

#### 4.2.2 Geomechanical properties of the crystalline rock

Laboratory tests were performed by Valley [2007] and Rummel and Baumgartner [1991] on Soultz-sous-Forêts granite in order to acquire its uniaxial compressive strength and static Young's modulus. They showed that uniaxial compressive strength ranges from 100 to 130 MPa for unaltered granite. One sample with significant vein alteration had a uniaxial compressive strength about 30% lower than that of the unaltered sample. The Young's modulus of unaltered granite is  $54 \pm 2$  GPa, and samples with vein alteration also show a reduction of Young's modulus of around 30%.

The sonic log was run over the first 3800 m of the GPK2 well and acquired compressive  $v_p$ , shear  $v_s$  and Stoneley  $v_{st}$  waves velocity. The two first waves are sensitive to strong modifications of the mechanical properties. The dynamic Young's modulus ( $E_{dyn}$ ) and Poisson's ratio ( $\nu_{dyn}$ ) of the granite can be estimated by using this equation [Fjaer *et al.*, 2008]

$$E_{dyn} = \frac{\rho v_s^2 (3v_p^2 - 4v_s^2)}{(v_p^2 - v_s^2)} \quad (4.1)$$

$$\nu_{dyn} = \frac{v_p^2 - 2v_s^2}{2(v_p^2 - v_s^2)} \quad (4.2)$$

with  $\rho$  is rock density. Within the crystalline rock, wireline density logs down to 3.6 km give a mean density of  $2.6 \pm 0.1$  g/cm<sup>3</sup>.

The dynamic Young's modulus and Poisson's ratio are rather stable for massive granite, respectively  $61 \pm 2$  GPa and 0.18. However, they show a sharp change for fractured and altered zones over 32% and 27% for the Young's modulus and Poisson's ratio, respectively. As expected, the dynamic elastic properties of the granite are better than its static properties. However, both the static and dynamic elastic properties show a similar reduction of the elastic moduli for fractured granite of around 30%.

The presence of fractures can also be deduced from the Stoneley waveform measurement [Hornby *et al.*, 1989]. In GPK2, the major anomalies visible from Stoneley slowness are located in the fractured zones observed between 3000 – 3500 m [Genter and Tenzer, 1995]. That's might explain the high variation of elastic moduli in this zone.

Based on the elastic moduli pattern, GPK2 can be separated into three main distinctive sections (**Figure 4.2**):



- From 1420 – 1950 m, which are characterized by rather high Poisson’s ratio and low Young’s modulus suggesting that granite is rather altered and fractured.
- From 1950 to 2960 m, high and stable values for Young’s modulus related to a massive porphyritic granite.
- From 2960 to 3820 m, Young’s modulus is low and very noisy suggesting that GPK2 penetrated a highly fractured granite section.

The elastic properties zonation above is consistent with the lithology characterization proposed by cutting and log data, i.e. significantly lower dynamic Young’s modulus and higher Poisson’s ratio for fractured porphyritic granite (**Figure 4.2**). Assuming that crystalline rock is mechanically isotropic and the perturbation of its mechanical properties can be attributed only to the occurrence of fractures and accompanying alteration, this information can be extended with the help of the petrographic log into the deeper part of the well. Furthermore, the elastic-properties information can also be laterally distributed among the wells following the lithology boundary.

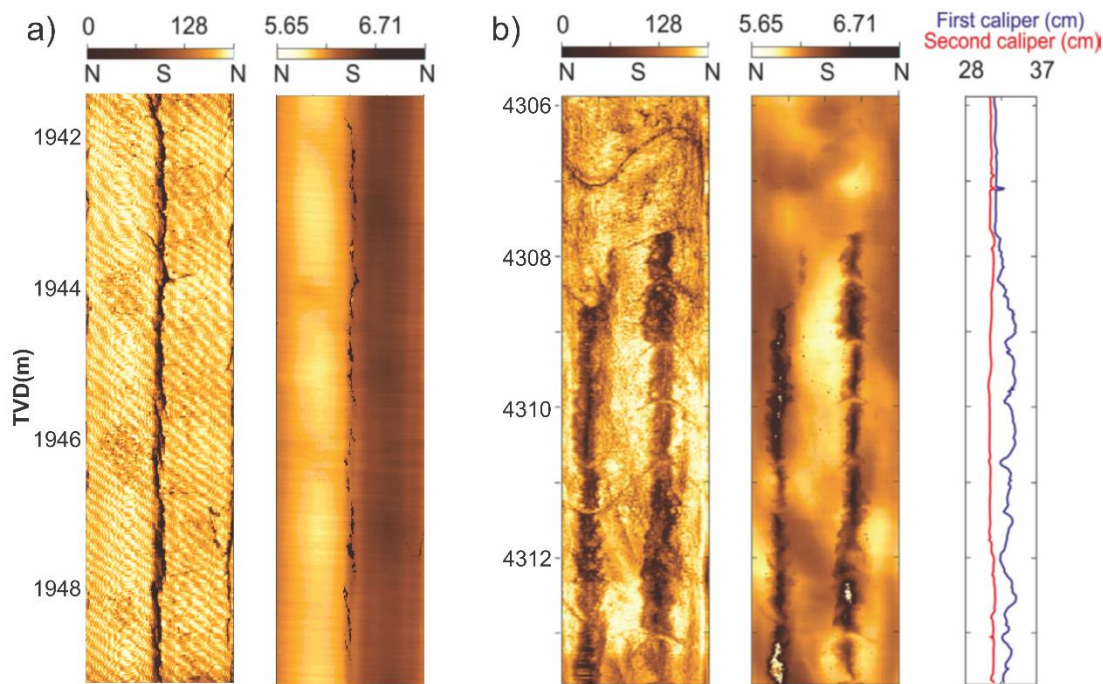


**Figure 4.3:** Typical DITF (a) and breakout (b) observed in UBI images. Wellbore failures appear as pair of zones (narrow zones for DITF and broad zones for breakout) of low amplitude (dark zones) on the amplitude log and increased borehole radius (dark zones) on opposite sides of the borehole on the travel time log. Caliper data were also used to measure the depth of the borehole elongation (right).

### 4.3 State of stress in Soultz-sous-Forêts

Wellbore failures were identified from the high-quality acoustic borehole televiewer (UBI) log that was run in the granite section of the deep well GPK4. GPK4 is the most deviated well in the Soultz-sous-Forêts geothermal field. Its deviation from vertical



exceeds  $15^\circ$  in the depth range of 2490 -4740 m TVD and reaches a maximum deviation of  $35^\circ$  at a depth of 4220m. The UBI tool provides detailed images of the ultrasonic reflectivity of the borehole wall along with the borehole geometry at an angular resolution of  $2^\circ$  inferred from the travel time. The logs were acquired in two runs 15 and 18 h after completion of drilling, respectively. Hence, the effect of time-dependent breakout growth was probably still insignificant. Median filtering with a kernel half width of seven samples (corresponding to  $14^\circ$ ) was applied to remove noise in the image data through a one-dimensional linear filter.

Wellbore failures can be grouped into two main types, i.e. tensile failure (DITF) and compressive failures (breakout). On the UBI image, wellbore failures appear as zones of increased borehole radius on the travel time log and low amplitude on opposite sides of the borehole on the amplitude log. Typical DITF and breakouts observed on the UBI image are shown in **Figure 4.3**.

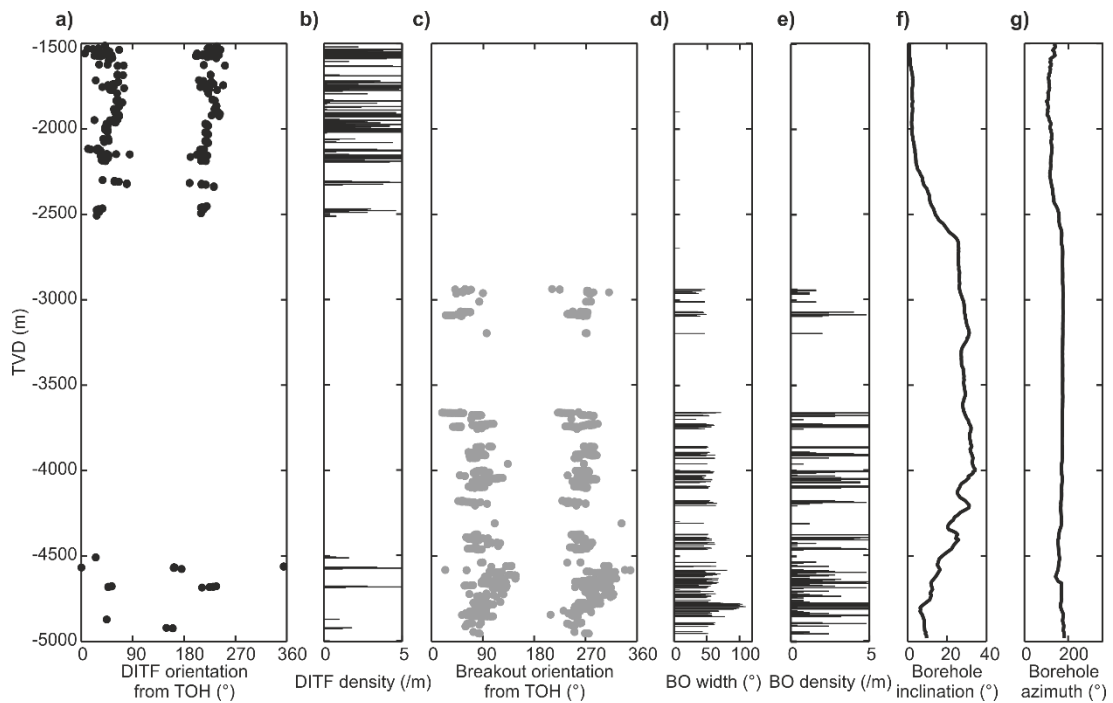


**Figure 4.4:** Results of the detailed analysis of the wellbore failure in a deviated GPK4 well. (a) Drilling induced tensile failure (DITF) orientation measured from TOH, (b) DITF density, (c) breakout orientation measured from TOH, (d) breakout width, (e) breakout density, (f) borehole inclination and (g) borehole azimuth.

**Figure 4.4** shows an overview of the DITF and breakout observation as discussed subsequently. Whereas DITF was observed mainly in the upper section of the well between 1500 to 2500 m TVD, breakouts were observed in the lower section starting at a depth of 2900 m TVD. The orientation and width of wellbore failure trends seen on UBI images were then measured every 20 cm. Both sides of the DITF and the breakouts were picked. A total of 1221 and 827 DITF and borehole elongation pairs, respectively, were identified. Each pair is then considered an individual DITF or breakout with a uniform length of 20cm. This approach enables us to examine the

characteristics of stress heterogeneities estimated from wellbore failures on deviated wells in fractured crystalline rock

#### 4.3.1 Wellbore failures in an inclined well

As a large fraction of the GPK4 well is deviated, it is necessary to analyze the occurrence of the wellbore failures in such deviated wells. In a deviated well, the principal stresses, i.e. vertical stress ( $S_v$ ), minimum ( $S_{hmin}$ ) and maximum ( $S_{Hmax}$ ) horizontal stress, acting in the vicinity of the wellbore wall are not aligned with the wellbore axis and the occurrence of the wellbore failures can be estimated based on the magnitude of the principal stresses acting in a plane tangentially to the wellbore wall,  $\sigma_{tmax}$  and  $\sigma_{tmin}$ . The principal stress,  $\sigma_{ij}$ , must be transformed into a wellbore coordinate system in order to analyze failure in a well of any orientation (**Figure 5**). This transformation can be achieved by utilizing tensors that rotate the principal stresses first into a geographic and then into a wellbore coordinate system according to the well trajectories [Peška and Zoback, 1995]. The maximum ( $\sigma_{tmax}$ ) and the minimum ( $\sigma_{tmin}$ ) tangential stresses are defined by:

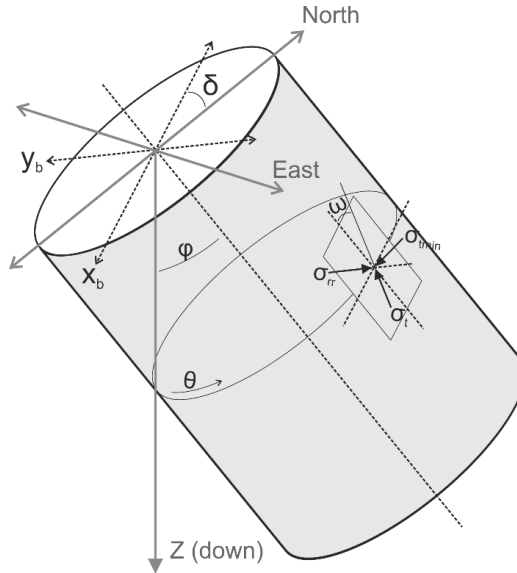


**Figure 4.5:** Sketch of the transformation of the principal stress from north geographic to arbitrary wellbore trajectory based on its azimuth ( $\delta$ ) and inclination ( $\phi$ ). Principal stresses acting on the borehole wall,  $\sigma_{tmax}$ ,  $\sigma_{tmin}$  and  $\sigma_{rr}$ , are then calculated after the transformation.

$$\sigma_{tmax} = \frac{1}{2}(\sigma_{zz} + \sigma_{\theta\theta} + \sqrt{(\sigma_{zz} - \sigma_{\theta\theta})^2 + 4\sigma_{\theta z}^2}) \quad (4.3)$$

$$\sigma_{tmin} = \frac{1}{2}(\sigma_{zz} + \sigma_{\theta\theta} - \sqrt{(\sigma_{zz} - \sigma_{\theta\theta})^2 + 4\sigma_{\theta z}^2}) \quad (4.4)$$

where  $\Delta P$  is excess pressure in borehole,  $\sigma_{zz}$  is the stress in axial direction,  $\sigma_{\theta\theta}$  is the stress tangential to the borehole and  $\sigma_{\theta z}$  represents the shear stress.

For specified remote stresses and borehole orientations we can determine the azimuth of the greatest compressive stress,  $\sigma_{tmax}$ , at the borehole wall. It is the

azimuth at which breakouts are expected to form. *Mastin et al.* [1991] showed that this azimuth might be rotated from the direction of  $S_{hmin}$  as the borehole deviates from the direction of the vertical principal stress. The magnitude of the rotation of the breakouts' orientation in deviated boreholes depends on the type of faulting regime in which the well was drilled i.e., normal, strike-slip, or thrust, on the deviation angle  $\phi$  of the borehole axis from vertical, and on the magnitudes of the three principal stresses.

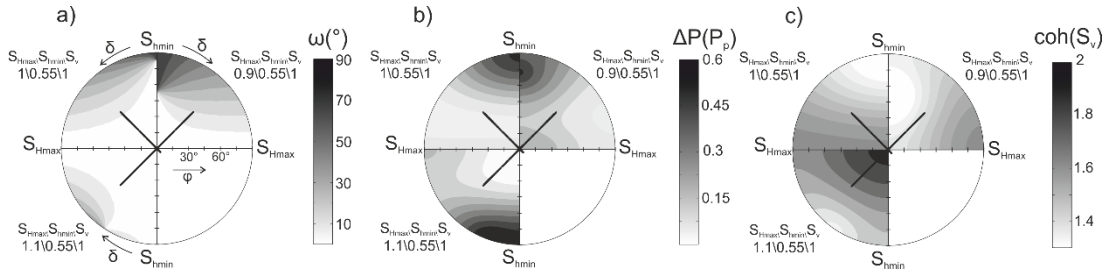


**Figure 4.6:** The effect of the inclination to the wellbore failure observation. (a) Breakout orientation deviation from  $S_{hmin}$ , (b) required excess pressure in borehole to create tensile failure, (c) required rock cohesion to prevent compressional failure. Azimuth and inclination of the GPK4 wall is shown in black line.

**Figure 4.6.a** shows the rotation angle of breakout orientations from  $S_{hmin}$  which was calculated for any oriented well throughout a range of values of possible faulting regime in Soultz-sous-Forêts, i.e. normal to strike slip. The GPK4 well trajectory is shown as a thick black line; the well is drilled towards  $50^\circ$  clockwise from  $S_{hmin}$  with inclinations vary from  $0^\circ$  to  $35^\circ$ . A lower-hemisphere diagram is used, where any point represents a well of a given azimuth and deviation. Arbitrarily oriented holes are shown as a function of their inclination with respect to vertical (radial distance from the center) and azimuth measured clockwise from  $S_{hmin}$ . The magnitude of  $S_{Hmax}$  and  $S_{hmin}$  are normalized with the  $S_v$  to make this analysis independent of the depth.

In a normal faults stress regime, breakouts in part of the well with low inclination oriented parallel to  $S_{hmin}$ , whereas in steeply inclined wells (more than  $30^\circ$ ) the direction of breakout is deviated up to  $15^\circ$ ; which is about the same as the uncertainty of the orientation of the principal horizontal stresses estimated from wellbore failures (Sahara et al., 2014). Furthermore, for  $S_{Hmax} = S_v$  and  $S_{Hmax} = 1.1 S_v$  the deviation of breakouts orientations in GPK4 is less than  $10^\circ$ . Hence, it can be concluded that the inclination of the GPK4 well did not cause significant perturbation to the orientation of the breakouts.

The area of compressive failure can be estimated based on the tangential stress concentration. It is usually assumed that failure will occur if the compressive stress concentration at the borehole wall is greater than the compressive strength of the rock,  $coh$ , i.e. (Zoback et al., 2003b). If compressional failure is developed, the width of breakout ( $\omega$ ) can be estimated by using

$$\cos \omega = \frac{(coh + \Delta P + \sigma^{\Delta T}) - \sigma_{tmax} - \sigma_{tmin}}{2\sigma_{tmax} - 2\sigma_{tmin}} \quad (4.5)$$

It can be seen that if the compressive strength is high, the width of the compressive wellbore failures can be minimized or even diminished. **Figure 4.6.b** shows the required compressive strength in order to prevent failure at the borehole wall. The compressive strength is normalized with the magnitude of  $S_v$ . It is shown that for normal faulting regimes, a constant compressive strength of around  $1.4 S_v$  is required to prevent borehole breakout to be formed at any inclination of the GPK4 well. For  $S_{Hmax} = S_v$  and  $S_{Hmax} = 1.1 S_v$ , the magnitude of the required rock strength decreases with increasing well inclination. The highest stress concentration is observed for a vertical well in a strike slip regime. In this case, boreholes are oriented parallel with the intermediate stress, hence, highest compressive-stress concentration is observed. Due to this high stress concentration, breakouts will be observed unless the compressive rock strength is twice as great as  $S_v$ .

If  $\sigma_{tmin}$  goes into tension at certain angles of  $\theta$ , tensile fractures will initiate at this point, provided  $\sigma_{tmin}$  overcomes the tensile strength of the rock  $T_0$ . Hence, the tensile fractures will initiate when the following occurs.

$$\sigma_{tmin} = -T_0 \quad (4.6)$$

$T_0$  is often expected to be very close to zero because some preexisting fractures or irregularities are usually present on the borehole wall [Jonas and Baudalet, 1977]. In this study,  $T_0$  is assumed to be zero. The wellbore excess pressure at fracture initiation, i.e. wellbore pressure that satisfies equation 4.6, is hereafter referred to as the initiation pressure,  $p_{frac}$ . **Figure 4.6.c** shows  $p_{frac}$  for any oriented wellbore. It is shown that when  $S_{Hmax} = S_v$  and  $S_{Hmax} = 1.1 S_v$  the highest tendency of tensile failure is observed for vertical well. Especially for strike slip, DITF will occur without any excess pressure in a vertical borehole.  $p_{frac}$  is increasing with increasing inclination, except for normal fault in which lower  $p_{frac}$  is required for the inclined section of the GPK4 well.

It is evident that there is a depth-partition in the type of wellbore failure, with DITFs occurring predominantly in the upper parts of the well whereas breakouts predominate below. It is interesting as DITF is only observed in the vertical section of the well (inclination of less than  $10^\circ$ ), which is in agreement with the high tendency of the tensile failure to be formed in a vertical well when  $S_{Hmax} = S_v$  and  $S_{Hmax} > S_v$ . These DITF and breakouts patterns observed in GPK4 well suggest that the stress regime in Soultz is more strike slip and that one of the principal stresses is vertical.

#### 4.3.2 Estimation of the in-situ stress field and its heterogeneities

Taking into account that the average strength of the granite from in-situ laboratory measurement is 100 MPa [Valley, 2007], breakout should be observed starting from depth of around 3300 m for vertical well and around 4000 m for around  $25^\circ$  deviated well. However, a cluster of breakouts is observed at a depth of around 2900 m where the well is inclined by around  $25^\circ$ . Interestingly, those breakouts observed in the fractured zone and terminated at depth of around 3100 m where the well start

intersecting the massive porphyritic granite. This suggests that those breakouts are most likely to be caused by the significant reduction of the rock strength due to fractures. Those breakouts have characteristics of asymmetrical shape of borehole elongations pair; the two elongations are shifted by more than  $20^\circ$  from the perfectly opposite direction and the width of elongations differs by more than  $15^\circ$ . The similar asymmetric pattern is also found for DITF observed at the deepest 500 m of the GPK4 well.

*Sahara et al.* [2014] shown that the orientation of those wellbore failures are highly affected by the dip direction of the fractures intersecting the well, while the symmetric one oriented parallel to the  $S_{hmin}$  or systematically deviated in the vicinity of major fracture zones. Hence, we considered the asymmetric wellbore failures as the fractured-related failures, and the symmetric one as the stress-related failures.

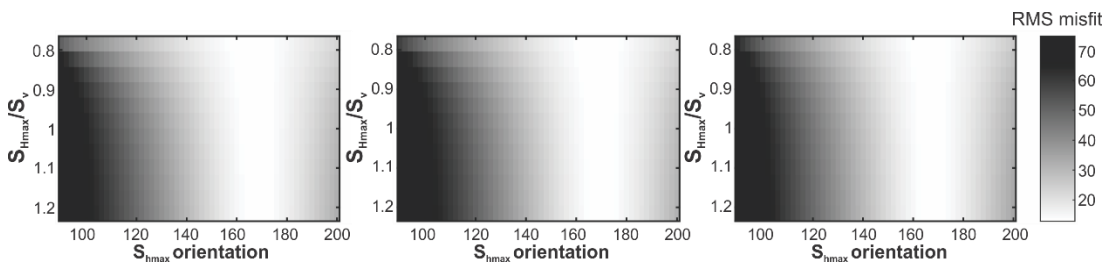


**Figure 4.7:** The RMS misfit of wellbore failures orientation between modeled and observed wellbore failures; if both breakout and DITF data are combined (a), breakout data only (b) and DITF data only (c).

#### 4.3.2.1 Stress orientation

The stress profile of  $S_v$  and  $S_{hmin}$  obtained by *Cornet et al.* [2007] is used as an input for this stress inversion. An iterative forward modeling of the orientation of wellbore failures (equation 4.5) at each depth section is performed for a selected range of magnitude and orientation of  $S_{Hmax}$ . The misfit,  $\Delta\theta$ , is defined as the angle between modeled wellbore failures orientation and observed data. Root mean square (RMS) is then used to represent the misfit for each  $S_{Hmax}$  orientation and magnitude.

Three different set of data is used in this inversion: both breakout and DITF data breakout data only and DITF data only. **Figure 4.8** shows the  $\Delta\theta$  values for all data set as a function of  $S_{Hmax}$  orientation and magnitude. White areas define stress regimes with  $\Delta\theta$  values lower than  $20^\circ$ . Gray to black areas indicate high  $\Delta\theta$  values of up to  $70^\circ$ . Consequently, the white areas represent stress regimes with the best agreement of observed and modeled data. The best fit is marked by the grey line. The results of the inversion using three different set of data show a consistent pattern;  $S_{Hmax}$  is oriented toward  $N168^\circ E \pm 15^\circ$ .

However, the misfits are independent of the  $S_{Hmax}$  orientation. Therefore, it is not possible to deduce a preferential  $S_{Hmax}$  magnitude. This may be because the deviation of the wellbore failures from the orientation of principal horizontal stresses caused by the well inclination is not significant, hence it cannot be used to determine the magnitude of the principal stress. This is the case for strike slip regime where

wellbore orientation and inclination have little effect on the wellbore failures orientation (**Figure 4.6.a**).

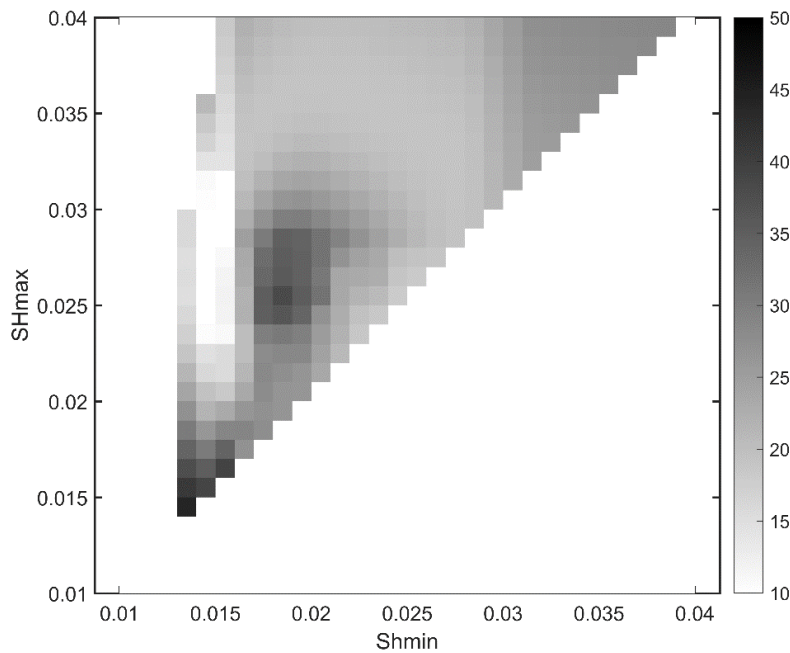


**Figure 4.8:** Stress profile based on the wellbore failures orientation and width observed in the GPK4 well. a)  $S_{Hmax}$  orientation and b)  $S_{Hmax}$  and  $S_{Hmin}$  magnitude.

The procedure of the estimation of the  $S_{Hmax}$  orientation is repeated for every 200 m depth interval to analyze the stress heterogeneity along the well for all type of wellbore failures observed in each depth section. The results of the  $S_{Hmax}$  orientation profile is shown in **Figure 4.8**. It is shown that the orientations of  $S_{Hmax}$  are aligned with the mean  $S_{Hmax}$  orientation in the massive granite and are shifted by approximately  $15^\circ$  in the fractured granite section. Apparently, the uncertainty of the orientation of  $S_{Hmax}$  is greater in the fractured zone. Particularly, in a highly fractured zone at depth of around 4500 m, a satisfactory result of  $S_{Hmax}$  orientation could not be achieved, i.e. the uncertainty of the  $S_{Hmax}$  orientation is greater than  $35^\circ$ . It might be due to the high material heterogeneity in this zone caused by fractures, hence, wellbore failures are arbitrarily oriented toward the weak zones.

#### 4.3.2.2 Stress magnitude

The magnitude of the principal horizontal stresses could be estimated from the width of borehole breakouts. The information of the elastic moduli and the uniaxial compressive strength of the rock used for this stress inversion is obtained based on the results of the laboratory measurement and sonic log run in GPK2 (**Figure 4.2**). The compressional strength and Young modulus of the massive granite is 100 MPa and 54 GPa, respectively, and 30% lower each for fractured rock. The width of the breakouts is calculated using equation 4.5.

Iterative forward modeling is performed to minimize the misfit ( $\Delta\theta$ ) between the observed and modeled breakout width. In this calculation,  $S_{Hmax}$  and  $S_{Hmin}$  are varied

while  $S_v$  is fixed. We sample all magnitudes of  $S_{Hmax}$  and  $S_{Hmin}$  that fall within the stress polygon [Zoback *et al.*, 2003] assuming that the friction coefficient is 1. However, a satisfactory result of the  $S_{Hmax}$  magnitude estimation could not be achieved, i.e. magnitude uncertainty of  $S_{Hmax}$  greater than 30%. Based on equation 4.5, the slight changes of breakout width affect the magnitude of  $S_{Hmax}$  significantly. Hence, the high variation of the breakout width, especially, in the fractured zone make this stress estimation is not possible.

To better analyze the effect of fractures on the stress estimation, this procedure is repeated for every 200 m depth interval. The high uncertainty of the magnitude of the  $S_{Hmax}$  in highly fractured granite might be explained as follows. The development of the breakout is a function of the value of the differential stress and the material strength. The previous slip on the major fracture zone will cause the reduction of the differential stress with or without brittle deformation depending on the failure mechanisms. The occurrence of clay mineral in some fracture zones in Soultz [Meller *et al.*, 2014a; Sausse, 2002] indicated that creeping mechanism might play an important role in the previous deformation. In this case, the reduced stresses around the fracture zone limit the failure area at the borehole wall, even in some fracture zones with high clay contents no breakouts are observed. On the other hand, the brittle deformation might significantly reduce of rock strength and, hence, extremely wide breakouts were formed, e.g. breakouts at depth of around 4800 m. Both upper and lower limits of breakout width are observed in highly fractured granite, thus, the uncertainty of the stress magnitude is very high in fractured zone.

For this reason, we exclude the breakouts data observed in the fractured granite and recalculate the magnitude of  $S_{Hmax}$ . The same procedure is applied. **Figure 4.9** shows the  $\Delta\theta$  values of breakout widths in GPK4 as a function of  $S_{Hmax}$  and  $S_{Hmin}$  magnitude. The best fit is obtained when  $S_{Hmax} = 0.9 - 1.15 S_v$  and  $S_{Hmin} = 0.62 S_v$ . Interestingly, the magnitude of  $S_{Hmin}$  determined from the breakout width is comparable to the one from hydraulic data at shallower depth which shows  $S_{Hmin} = 0.67 S_v$  (Cornet *et al.*, 2007). In the absence of hydraulic data, this suggests that by carefully selecting the input breakout data this method might provide a reliable alternative for estimating the magnitude of  $S_{Hmin}$ .

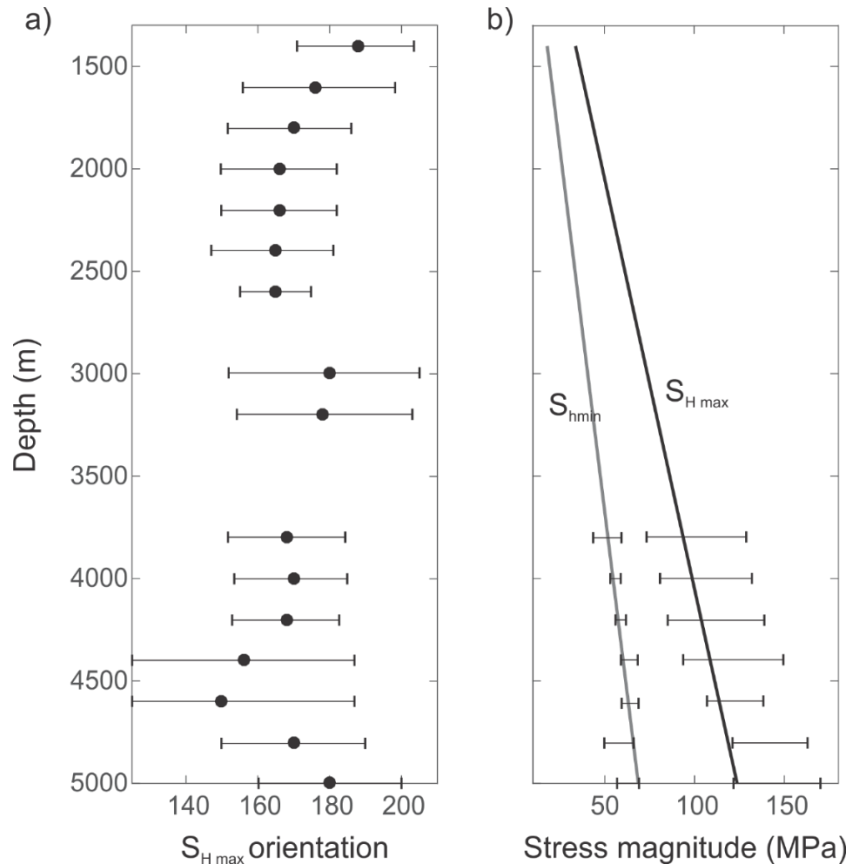


**Figure 4.9:** The RMS misfit of borehole breakout width between modeled and observed wellbore failures for each  $S_{Hmax}$  and  $S_{hmin}$  magnitude.

#### 4.4 Wellbore failure in a heterogeneous fractured material

In this chapter, we intend to model the effect of the material heterogeneities to the stress distribution around borehole and, eventually, calculate the damaged area accordingly. The commercial finite element software Abaqus (Simulia) is used in this simulation. In order to compute the stresses around a vertical wellbore, we model a 2-D slice orthogonal to the wellbore axis. The model is meshed with four-node linear quad elements with mesh density increasing in the vicinity of borehole (**Figure 4.10**). A plane strain assumption is applied in the modeling scheme.

Weak zone is modeled by a narrow zone which has lower elastic properties. Young's modulus reduction of 30% from the intact rock is applied in the center of the weak zone, comparable to the elastic moduli reduction observed in Soultz-sous-Forêts. Fractures also reduce the capability of host rock to support stress [Heap and Faulkner, 2008], hence, we also lowering the compressive strength at the weak zone by the same percentage as the Young's modulus reduction.



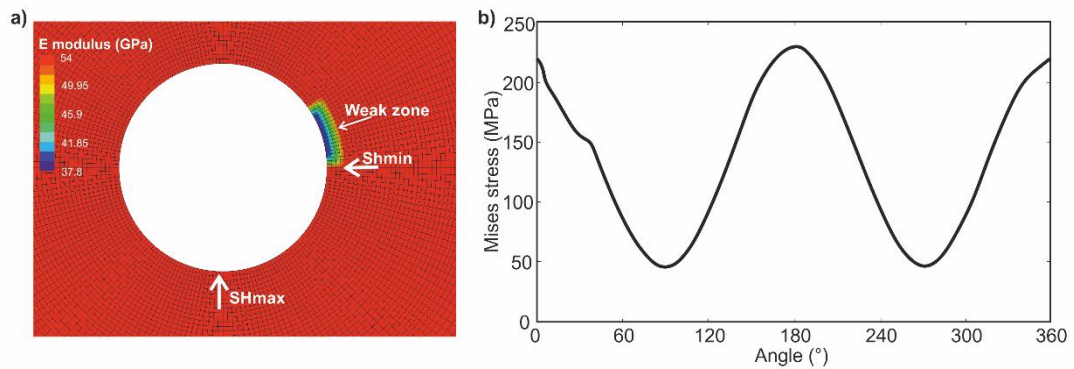


**Figure 4.10:** The mesh used in the numerical modeling (left). Narrow and thin weak zone were modeled the intersection with the fracture. Weak zone has lower elastic properties compare to the surrounding material. Stress distribution at the borehole wall (right). The occurrence of the weak zone promotes a lower stress region.

The model is pre-stressed with a far field effective stress with a magnitude of 15 MPa, 70 MPa and 60 MPa for  $S_{hmin}$ ,  $S_{Hmax}$ , and  $S_v$ , respectively, to represent the Soultz stress state at depth of around 4000 m. Displacement boundary conditions are chosen, i.e. the outer nodes are fixed and the inner nodes of the wellbore wall are free. At the beginning of the simulation the nodes at the wellbore wall are fixed to simulate the undisturbed rock. Drilling of the well is simulated by instantaneous release of this boundary condition. It can be seen in **Figure 4.10** that a small weak zone alters the stress distribution around boreholes; it is lower as it should be observed in the homogeneous material.

Micromechanical analysis of borehole breakout from laboratory experiments (e.g. *Ewy and Cook [1990]*, *Haimson and Lee [2004]*) and numerical modeling (e.g. *Sahara et al. [submitted]*) showed that the development of breakout started from the first damage area at the borehole wall and grew deeper and wider subsequently. The growing of the damage area involved plastic deformation through complex fracturing processes. As the purpose of this modeling is to model the perturbed orientation of breakout due to the occurrence of weak zone, only the first damage area at the borehole wall is modeled. Hence, elastic material assumption is used in this modeling and the stimulation is stopped when a significance damage in the vicinity of borehole is observed.

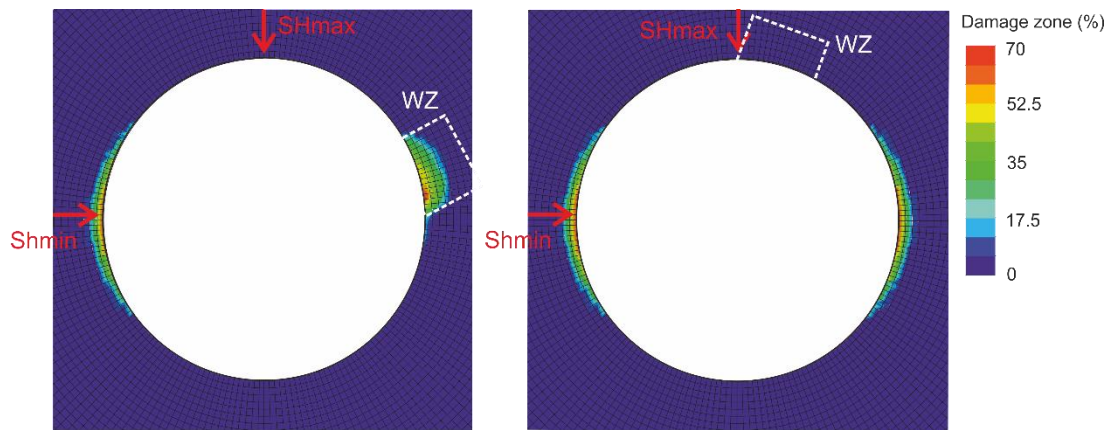


**Figure 4.11:** The final damage zone modeled in the heterogeneous material with the weak zone is located in the vicinity of  $S_{hmin}$  direction (left) and  $S_{Hmax}$  direction (right).

Continuum damage mechanics concept [Lee and Fenves, 1998; Lubliner et al., 1989] is used to calculate the damaged zone due to compressional stress around borehole. The damaged zone is defined as the zone which the stresses acting in that zone are greater than its compressional strength. The step failure model is incorporated in Abaqus using a subroutine. Here the damage state of the model is read and updated according to the current stress state at each time step. The stress and the stiffness of the material is then updated based on the damage level at each step.

$$D = 1 - \frac{E}{E_0} \quad (4.6)$$

We run the simulation in two cases. First the weak zone is set in the vicinity of  $S_{hmin}$  direction, while in the second run it was moved close to  $S_{Hmax}$  direction. The purpose is to model how the stress perturbation around those weak zones alter the calculated damage zone. In the first model, we can see that the failure was initiated in the weak zone and then followed by the failure in  $S_{hmin}$  direction (**Figure 4.11.a**). The damage zones are then developed according to this initial failure. The orientation of the modeled breakout is perturbed by the occurrence of the weak zone and rotated from  $S_{hmin}$  direction. Due to the heterogeneity of the material properties, the breakout does not develop symmetrically as is explained in the Kirsch's solution [Kirsch, 1898]. These breakouts are those which we defined as the fracture-related wellbore failures earlier. They might not show the true direction of  $S_{hmin}$ , instead it was affected by the weak zone.

It was not the case for the second run. Here a symmetric breakout shape parallel to the direction of  $S_{hmin}$  is resulted (**Figure 4.11.b**). The strength degradation at the weak zone was not significant enough to facilitate the breakout to be developed in the weak zone. In the direction of the  $S_{Hmax}$  stress, the stresses are less concentrated hence it is difficult to reach the yield criterion here prior to the  $S_{hmin}$  direction. A huge reduction of material strength is required to facilitate the damage to be developed in the  $S_{Hmax}$  direction.

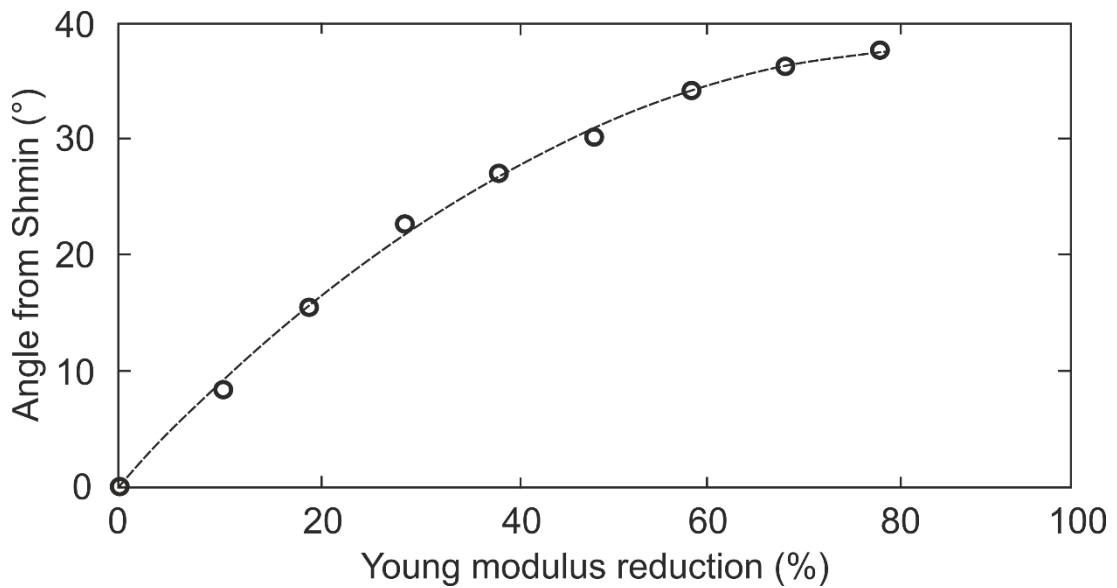


**Figure 4.12:** Graphic of the perturbing weak zone position as a function of the elastic properties contrast. Material properties reduction is in percent relative to the intact rock elastic properties.

#### 4.5 Discussions

---

The role of material heterogeneity in perturbing breakout orientation is described through the numerical modeling developed in this study. However, the critical question as to under what conditions breakout orientation is perturbed remains. A set of models with different positions and elastic properties of the weak zone have been run under several different differential stress magnitudes. The strength of the rock is assumed to be linear with the elastic properties of the rock. From the simulation results, a graphic of the position of the perturbing weak zone relative to  $S_{hmin}$  direction as a function of the weak zone elastic contrast with the intact rock was created (**Figure 4.12**). The area below the line shows the perturbing weak zones' position for a specific elastic properties contrast. The higher the degradation of the elastic moduli of the weak zones, the higher the possibility of altering the breakout formation at a greater angle from the  $S_{hmin}$  direction. A function of the weak zone elastic properties contrast relative to the intact rock and its position relative to the minimum horizontal stress required to perturb the orientation of breakouts is proposed. Consequently, it gives us a hint that the mechanical properties of fractures intersecting the well might be deduced from the pattern of the breakout orientation heterogeneities.

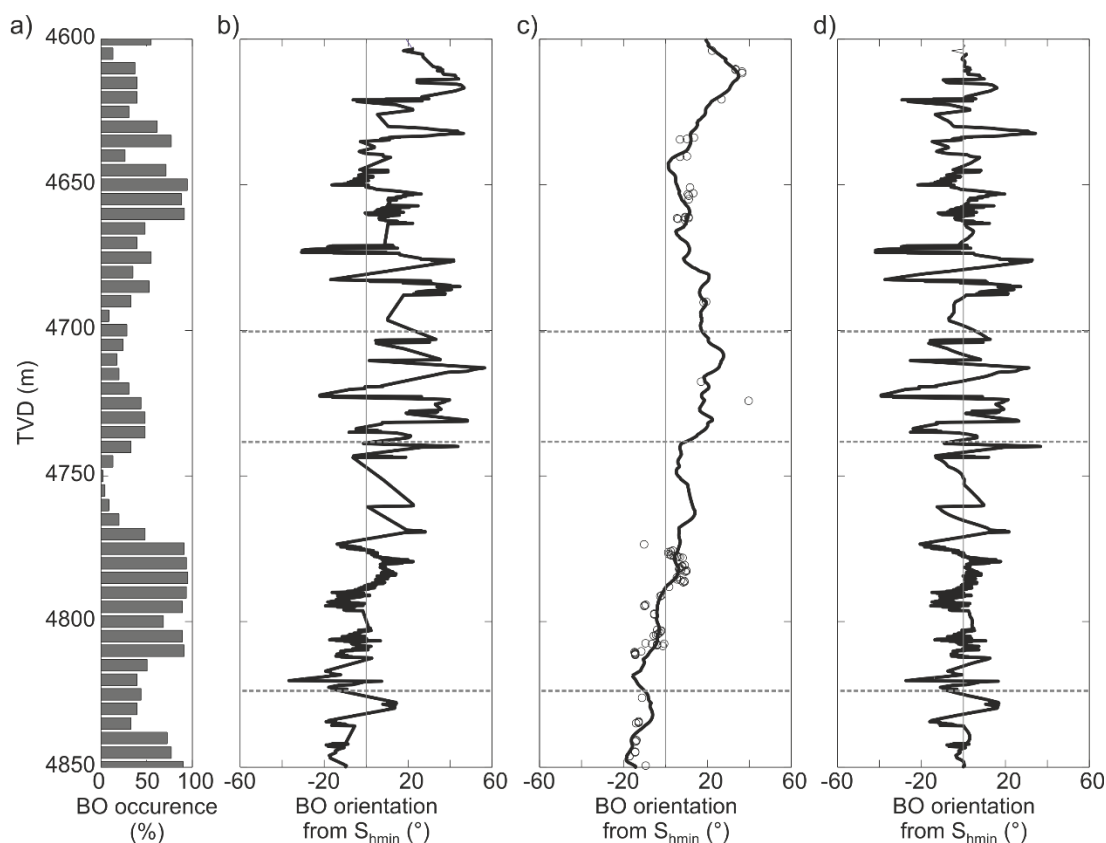


**Figure 4.13:** Breakout orientation analysis in the fractured zone at depth between 4600 – 4850 m. a) The percentage of breakout occurrence per 5 m. b) Breakout orientation deviations from the orientation of  $S_{hmin}$ . Breakout orientations data are averaged every 5 m. Breakout orientation anomalies are categorized into two group, anomalies with wavelength of more than 20 m (c) and less than 20 m (d).

As weak zones might perturb the initiation and the development of wellbore failures, critical question arise, can we use failures data observed in fractured rock as stress indicator? This discussion is missing in publications of wellbore failures as stress indicator. A detailed analysis of breakout occurrences and orientations pattern is performed in the highest density breakout area between 4600 – 4850 m (**Figure 4.13**). Within this depth section, GPK4 well intersected massive porphyritic granite up to approximately 4700 m and highly fractured two-mica granite in the lower part.

A low-pass filter is applied to select orientation data which has wavelength of more than 20 m (**Figure 4.13.c**). This filtered data is then subtracted from the original data to obtain the lower wavelength anomaly which might be related with the material heterogeneity in the reservoir (**Figure 4.13.d**). It can be seen in **Figure 4.13.c** that a systematic orientation rotation with a peak of around  $25^\circ$  is observed in the fractured zone. A sinusoidal pattern of the breakout orientation deviation, with a center at depth of around 4720, coincidences with two major fracture zones that intersect the GPK4 well around that depth [Sausse *et al.*, 2010]. At a greater depth breakout orientation is shifted counterclockwise with the similar amplitude, which also

coincide with the occurrence of GPK4-FZ5100 major fracture zone. Hence it can be concluded that the major fracture zones significantly affect the large scale stress heterogeneities in the Soultz crystalline reservoir.

Based on these observations, a hypothesis of the breakout orientation rotation in the vicinity of a fracture could be developed as follow. If a fracture has an associated fractures damaged zone, the stresses are expected to be perturbed and rotated depending on the change in elastic properties of the damaged material [Faulkner *et al.*, 2006]. As the fracture core bears the most damage, the stress perturbation is assumed to be concentrated in that zone and to decrease with distance to the core. Wellbore failures will then develop according to this local stress perturbation. Hence, a gradual wellbore failures orientation rotation centered at the fault core is observed. The orientation rotation observed at depth of around 1500 m and 3000 m in this well could also be addressed with the same process. The stress heterogeneities plotted in **Figure 4.13.c** stem from the wellbore failures that defined previously as stress-related failures and, apparently, those data are a good indicator of the in-situ stress field and its heterogeneity.

In addition, a random pattern of orientation rotations is observed (**Figure 4.13.d**). This might well represent the wellbore failures orientation rotation due to material heterogeneity. The maximum amplitude of breakout orientations deviations is around 35°. Based on the results of the numerical modeling developed in this study and the field observation of the detailed breakout shape, we interpret those random stress heterogeneities represent the wellbore failures orientation perturbation due to material heterogeneity, or the fractured-related wellbore failures as defined previously. Despite those data do not related to the principal horizontal stresses, they could give us a hint about the mechanical properties of the rock in the surrounding of the well. This information could provide us an insight of the estimation of the damaging level in the fault core and, hence, its permeability. This will be a challenging task to be developed in the future because, despite a huge amount of image logs collected in the reservoir, none of them are used so far for this purpose.

## 4.6 Conclusion

---

Analyzing state of stress from wellbore failures at great depth is a challenging task, in particular because of the occurrence of highly fractured granite which make the orientation of wellbore failures is highly heterogeneous. Two type of wellbore failures are distinguished: stress-related and fracture-related wellbore failures. Based on the characteristics of each wellbore failures type, we concluded that only the stress-related wellbore failures can be used as a stress indicator. The orientation of  $S_{Hmax}$  is found to be  $N168^{\circ}E \pm 15^{\circ}$  and the magnitude of the two principal horizontal stresses are:  $S_{Hmax} = 0.9 - 1.15 S_v$  and  $S_{Hmin} = 0.62 S_v$ . Those are in agreement with the previous stress investigations, e.g. Cornet *et al.* [2007], Valley [2007] and Sahara *et al.* [2014]. Furthermore, the magnitude of  $S_{Hmin}$  determined from the breakout width is comparable to the one from hydraulic data at shallower depth which shows  $S_{Hmin} = 0.67 S_v$  [Cornet *et al.*, 2007]. In the absence of hydraulic data, this suggests that, by

carefully selecting the input data, this method could provide a reliable alternative for estimating the magnitude of  $S_{\text{hmin}}$ .

A numerical model of stress distribution around boreholes that incorporate the material heterogeneities could explain the observed breakout heterogeneities in this field. It was shown that for heterogeneous isotropic elastic material, the stress distribution around boreholes is dependent on the elastic properties of the material. It improves the analytical formulation of the stress distributions which developed under homogeneous material assumption, i.e. Kirsch solution [Kirsch, 1898]. A graphic showing the position of weak zones that perturb the development of breakouts as a function of the elastic properties contrast is presented. The results of the numerical modeling presented in this study give us an insight in inferring the mechanical properties of fractures and their immediate surroundings from the breakout observation, which is still missing in the current breakout orientations.

GPK4 well is unique data set, in which continuous wellbore failures are observed almost continuously on the 3.5 km depth section of the well. We concluded that wellbore failures are not related to the principal stresses only, but also to the effect of mechanical heterogeneities like weak zones with different elastic moduli, rock strength and fracture patterns. Hence, in order to obtain a reliable estimation of the stress orientation and its heterogeneity in such fractured reservoir, it is necessary to distinguished the stress-related wellbore failures from the fractures-related and to sample the stress field on a long interval.

---

## Characterization of the mechanical heterogeneity and their role in induced seismicity in Soultz-sous-Forêts fractured crystalline reservoir

This chapter is currently on-preparation for an international journal publication

### **Abstract**

The importance of the reservoir characterization for addressing a broad range of geomechanics-related problems and the limitation of the deep core data necessitates tools to characterize the mechanical properties indirectly from borehole data. The novel approach of integrating various borehole and hydraulic data of the Soultz-sous-Forêts EGS field proposed in this study enables a characterization of the deep crystalline rock with respect to their role in affecting the failure processes during stimulation. Three zones in the reservoir are proposed based on the inherent structures present in a set of geophysical logs of GPK4 well. The occurrence of abundance fractures and breakouts in the two-mica granite indicate that this zone is weaker than the massive porphyritic granite. In between, a transition zone is identified by its high clay content. On the top of this, the slip tendency of all minor and major fractures in each zone is estimated. Consequently, the reservoir rocks respond differently to the increasing pore pressure during fluid injection, e.g. an episodic fracture reactivation from two-mica to porphyritic granite, an anti-correlation between clay content and seismicity, a significantly higher number of events in the two-mica granite, and an extensive damage area in a larger crystal porphyritic granite. A similar pattern is observed for the other deep wells stimulation. Furthermore, the pattern of microseismicity in each zone is matched with the different injection schemes used in this field, suggesting that an adapted injection strategy might be developed based on the reservoir model proposed in this study. As most of the EGS target the crystalline rock, the understanding of the lithological controls on seismicity in granitic rock is crucial for the future development of the EGS.



## 5.1 Introduction

---

Enhanced Geothermal System (EGS) offer an attractive prospect for producing large quantities of energy from deep, low-porosity, hot crystalline rocks found in many places in the world. Often, the natural permeability of an EGS reservoir is too low for the requisite flow to circulate between the wellbores and is artificially enhanced. This enhancement is accomplished by a reservoir stimulation in which a large volume of fluid is injected into the rock mass at high flow rates that lead to the reactivation of the preexisting fractures. In this case, good knowledge of the stress field and the mechanical properties of the fractured reservoir rock is essential for the reservoir management.

Mechanical heterogeneities play a significant role in affecting the response of rock masses to massive fluid injection [e.g. Zoback, 2007]. The petrographical control on the frictional strength of granite is shown in experimental studies, e.g. Collins and Young [2000] and Sajid *et al.* [2016]. Preexisting fractures in the reservoir also have a significant effect on weakening mechanism in rocks, especially if those fractures are oriented preferably to the maximum principal stress [e.g. Jaeger *et al.*, 2007]. Hence, the analysis of the slip tendency of faults is currently becoming a standard exploration technique to anticipate on preferential fluid pathways with or without hydraulic stimulation [Morris *et al.*, 1996]. Alteration also plays an essential role for geothermal reservoirs, where percolation by geothermal brine promotes the formation of hydrothermally altered zones around fluid pathways [André *et al.*, 2006]. The dissolution of primary rock-forming minerals and the precipitation of secondary minerals, such as quartz, clay, or carbonates, change the in situ conditions on the mechanical strength of the rock [Meller and Kohl, 2014]. Hence, to characterize a geothermal reservoir and to assess its mechanics, it is important to understand the significance of each of those rock characteristics.

As deep core data and mechanical testing data on geo-reservoirs are limited, new tools are required to better characterize the stress heterogeneity and the mechanical properties indirectly from the geophysical well log and geological cutting data. Soultz-sous-Forêts is a unique EGS field with an extensive logging and hydraulic database, enabling us to perform a detailed analysis of the reservoir characteristics. Sahara *et al.* [2014] showed the immediate effect of the fracture network seen from the borehole on the heterogeneity of the stress field seen from stress indicators in the borehole. Magnetic susceptibilities of the cutting samples collected from all Soultz-sous-Forêts wells were used by Meller *et al.* [2014b] to estimate the lithology and the alteration grade of the reservoir rock. Furthermore, the clay content, an indicator of hydrothermal alteration processes, has been estimated from the fracture characteristic and the spectral gamma ray (SGR) log by Meller *et al.* [2014a] using a neural-network analysis.

Following the studies mentioned above, we intend to improve the characterization of the mechanical properties of the Soutz deep reservoir and its response to fluid injection. This study is focused on the open-hole section of the GPK4 well from 4480 to 4980 m depth (here and subsequently, the depths cited are the True Vertical Depth



(TVD) measured from the drilling platform). Herein, we first perform an integrated analysis of geological and geophysical borehole data measured in the GPK4 well. A neural-network clustering scheme is applied to identify inherent structures present in a set of geophysical logs of GPK4 well, i.e. magnetic susceptibility, fracture, alteration, and breakout. The reservoir characterization is made based on the distribution of neurons in the topology. . The tendency of preexisting fractures to be reactivated during stimulation is also analyzed. Hydraulic stimulation data performed in the same well is then used to infer the patterns of the microseismic events in the different zones proposed from borehole data, i.e. the occurrence time and the density of microseismic events, as well as the stimulated area. The role of each rock parameter in affecting the failure mechanism due to hydraulic stimulation is discussed. This integrated analysis can provide key information on the reservoir characteristics to improve the understanding of the failure mechanisms during hydraulic stimulation.

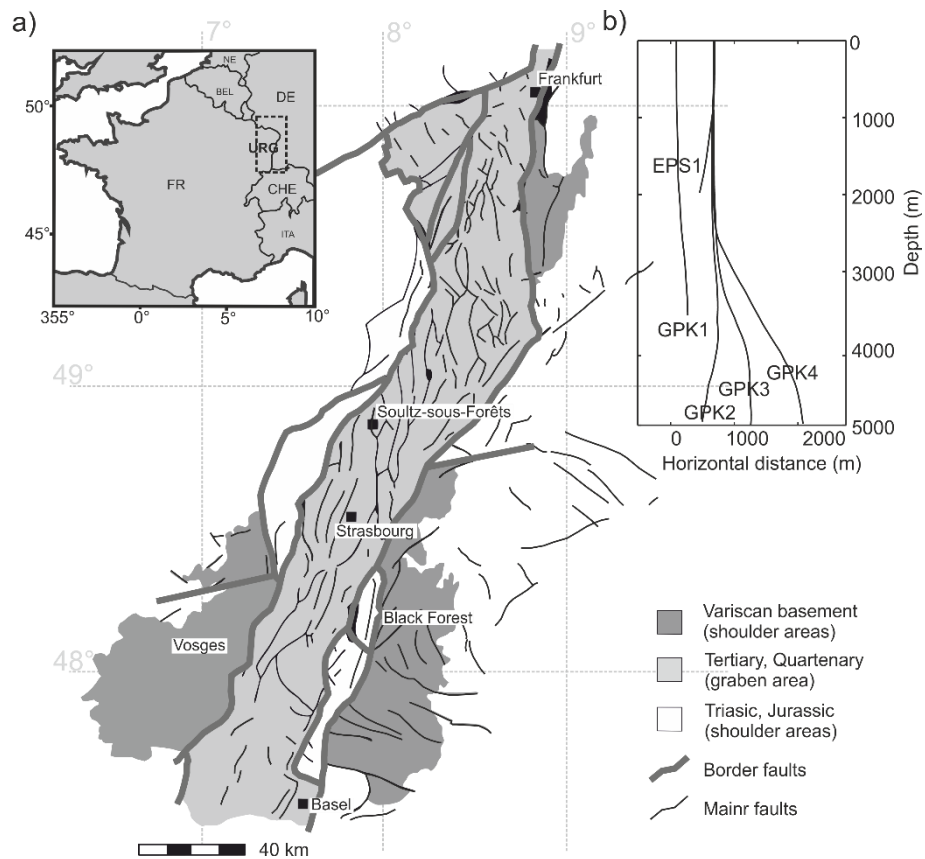


**Figure 5.1:** (a) Geological map and major fault map of the Upper Rhine Graben (URG) rift system (modified from Peters [2007]). The insert map shows the location of the URG (b). N-S depth projection of the five wells in the Soultz-sous-Forêts geothermal field.

## 5.2 Soultz-sous-Forêts geothermal field

The Soultz-sous-Forêts geothermal field is located in the Upper Rhine Graben (URG). The URG is a Cenozoic rift structure belonging to the West European Rift System

[Ziegler, 1994]. The intra-graben faults predominantly strike in N180±17°E direction parallel to the main border faults, whereas faults in the shoulder areas are bimodal with a primary strike orientation towards N45±15°E and N115±20°E (**Figure 5.1.a**). The kinematic of the intra-graben faults is predominantly extensional [Cardozo and Behrmann, 2006], which suggests that the current maximum principal horizontal stress ( $S_{Hmax}$ ) is oriented parallel to the orientation of the intra-graben faults. This is confirmed by the world stress map on a regional scale [Heidbach *et al.*, 2008]. The wellbore failures and the microseismic data observed in the Soultz geothermal field suggest that the local in-situ  $S_{Hmax}$  is oriented toward N168°E±10 and the stress regime is normal to strike-slip regime [e.g. Cuenot *et al.*, 2006; Sahara *et al.*, 2014].

This geothermal project is probably the most comprehensive research project in the field of EGS being developed so far. Initiated in 1986, it has now a long history which is broadly documented, e.g. Baria *et al.* [1999], Genter *et al.* [2010], and benefits from a vast amount of field observations in numerous domains (geology, geochemistry, geophysics, petrophysics, hydrogeology, etc.) gathered during the exploration, drilling, stimulation, circulation, production phases. Over the development phases of the EGS, five wells have been drilled and stimulated to create underground heat exchangers in the granitic formation (**Figure 5.1.b**). Three of these wells are currently used for operation with two wells as injectors (GPK3 and GPK4) and one producing well (GPK2) [Gérard *et al.*, 2006].

**Table 5.1.** Hydraulic stimulation data of the deep Soultz reservoir stimulation and the total number of induced seismicity. BHP is bottom hole pressure

Stimulation	Duration (hour)	Injected volume (m <sup>3</sup> )	Maximum BHP increase (MPa)	Number of located seismic events
GPK2 2000	141	22680	14.5	12217
GPK3 2003	255	37300	16	21981
GPK4 2004	83	9300	17	5753
GPK4 2005	95	12300	18	2968

The reservoir is bounded by the Soultz horst structure [Meixner *et al.*, 2016] and is covered by approximately 1400 m of Mesozoic and Cenozoic sediments. It mainly consists of two different granites. The shallow granite is a porphyritic monzogranite with large potassium-feldspar crystals in a matrix of quartz, plagioclase, biotite, amphibole and accessories of magnetite, titanite, apatite, allanite. This granite extends approximately from 1400 to 4700 m depth. Below, a fine-grained two-mica granite is found, with primary muscovite and biotite and a depletion of K-feldspar. The two mica-granite is interpreted as an intrusion of a younger granite into the porphyritic granite [Dezayes *et al.*, 2005].

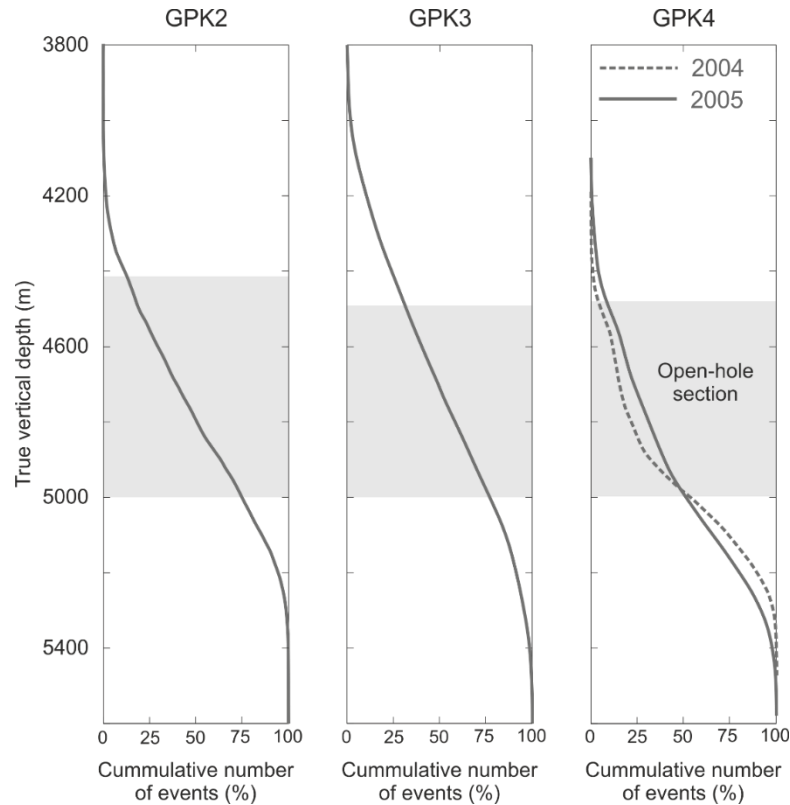


**Figure 5.2:** Cumulative number of microseismic events as a function of depth in the three deep wells in Soultz. The events in GPK4 well is the cumulative of two stimulations performed at 2004 and 2005. The open-hole section of each well is marked in gray area.

The crystalline reservoir is characterized by low porosity, natural and forced fluid circulation takes place through the fracture network. To increase productivity and the quality of the hydraulic connection between the wells, hydraulic stimulations were performed in the deep wells in 2000 (GPK2), 2003 (GPK3), and 2004 and 2005 (GPK4) [Genter *et al.*, 2010]. Tracer testing and geophysical monitoring carried out after each of the hydraulic stimulations indicated a good hydraulic connection between GPK2 and GPK3, while the link between GPK3 and GPK4 appeared to be poor [Sanjuan *et al.*, 2006]. It might be because of a fault interpreted to be located between GPK3 and GPK4 [Held *et al.*, 2014]. This fault is oriented E-W, which might be closed due to a high  $S_{Hmax}$  that is acting as the normal stress on this fault.

The stimulation of GPK4 produced less microseismic events than the other well stimulations (Table 5.1), which makes the determination of the detailed reservoir geometry difficult. Furthermore, GPK4 stimulation had a unique characteristic of microseismic events pattern; 80% of the microseismic events are located deeper than 4800 m (Figure 5.2). A flow test recorded during the GPK4 stimulation [Nami *et al.*, 2008] indicated a linear leakage of flow from 4500 m until the bottom-hole. The results of multidisciplinary studies, e.g. Sausse [2002], Kohl and Mégel [2007], Baujard and Bruel [2006] and Evans [2005], suggest that the characteristics of fractures in the crystalline rock play a fundamental role in governing the response of the reservoir to the

injection. By far, knowledge of the mechanical properties of the fractured granite relies much on the very limited laboratory measurements performed on core samples [e.g. Valley, 2007; Baillieux *et al.*, 2012]. These motivate us to investigate further the mechanical properties of fractures from borehole data. Taking advantage of the vast amount of logging and hydraulic stimulation data available in GPK4 well, this study focuses on this well to improve the characterization of the mechanical properties of the deep reservoir of Soultz and their impact on preexisting fractures reactivation during stimulation.

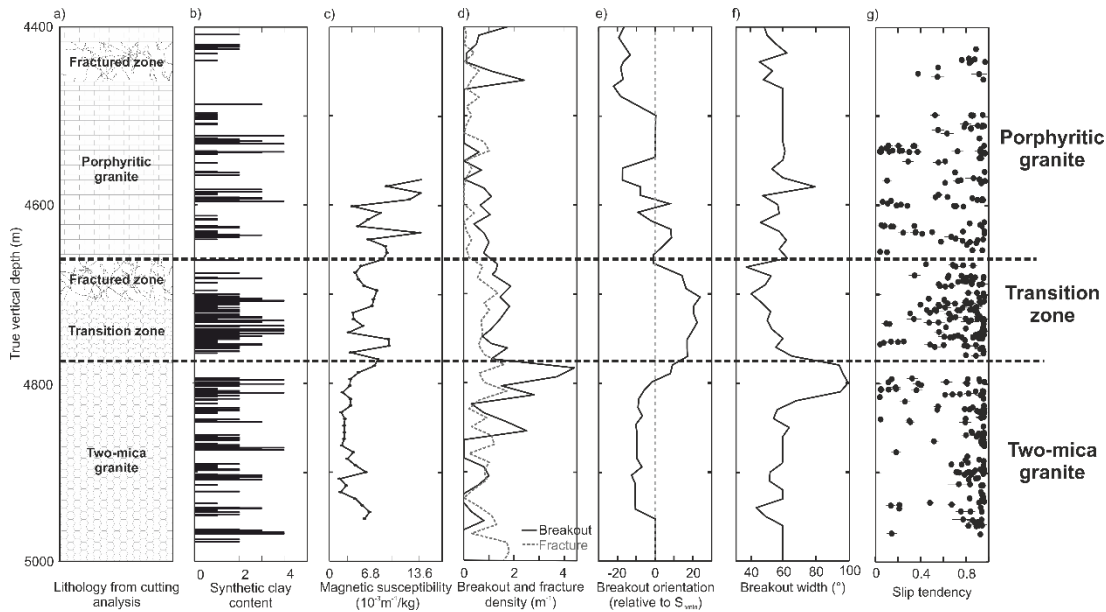


**Figure 5.3** Comparison of various geophysical and geological data of the GPK4 well open-hole section. a) Geological lithology log of the GPK4 well from the interpretation of cutting data, b) synthetic clay content log of GPK4 derived from spectral gamma ray and natural fractures data, c) magnetic susceptibility measured from cutting data, d) breakout and fracture density, e) breakout orientation, f) breakout width, and g) slip tendency of natural fractures observed in the well. Three different zones with different lithology, fracture characteristic, alteration and breakout pattern were distinguished.

### 5.3 Deep reservoir characterization from borehole observation

In this chapter, we propose an integrated analysis of the borehole data to better identify the rock characteristics of the deep geothermal reservoir in Soultz. Only the deep reservoir section penetrated by the open-hole of the GPK4 well at depths from 4437 to 4982 m is analyzed. As the reservoir rock experiences different phases of deformation, alteration, weathering processes, it requires a broad ranges of data to describe the induced effects and characterize the reservoir.

### 5.3.1 Input data

The lithology of the rock was derived from cutting data analysis *Dezayes et al.* [2005] (**Figure 5.3.a**) with the help of the magnetic susceptibility measurements (**Figure 5.3.c**). *Meller et al.* [2014b] measured magnetic susceptibility of drill cuttings recovered during the drilling of the Soultz wells to distinguish the two granites in the deep reservoir. They found that the combination of the bulk magnetic and the temperature-dependent susceptibility of drill cuttings could be used to make a distinction between porphyritic and two-mica granite. This analysis has an advantage compared to cutting data in determining the lithology of a fractured zone as it is based on the magnetite content, which is less affected by the washing out process of the drilling fluid than clay minerals or platy minerals.

The natural fracture data of the GPK4 well used in this study (**Figure 5.3.d**) were obtained from the French Geological Survey (BRGM) on the GPK4 image logs (*Dezayes et al.*, 2005). Major fracture zones derived from the geological analysis, induced microseismicity and vertical seismic profiles modeled by *Dezayes et al.* [2010] and *Sausse et al.* [2010] are also incorporated in this analysis. Their notations derived from the name of the well and the measured depth are used throughout this study, e.g. GPK4-FZ4710. All log data are presented in TVD, as a result of which the depth of the major fractures plotted in the figure might be different from the depth indicated by their name.

The occurrence of clay in fractures, as a product of the alteration process, is also an important characteristic since it affects not only the frictional strength of rock but also the flow paths through fractures. In-situ laboratory measurements revealed that the porosity of hydrothermally altered granite can be twice as high as a fresh unaltered granite [e.g. *Genter and Traineau*, 1996; *Ledesert et al.*, 1999]. The alteration degree was estimated from synthetic clay content analysis performed in fractured granite [*Meller et al.*, 2014a] (**Figure 5.3.b**).

Breakout data is used to infer the in-situ stress field and its heterogeneities in the reservoir [*Sahara et al.*, 2014] (**Figure 5.3.d-f**). The orientation and width of borehole elongation trends seen on UBI images run in the granite section of the GPK4 well were measured every 20 cm by *Sahara et al.* [2014]. A total of 472 borehole elongation pairs were identified in the open-hole section of GPK4. Each elongation pair was considered as an individual breakout with a uniform length of 20 cm. This detailed breakout data enabled us to examine the stress heterogeneity and its correlation with the mechanical properties of the crystalline rock. In addition, the tendency of fractures to be reactivated during the stimulation is also estimated in this study (**Figure 5.3.g**).

### 5.3.2 Neural network clustering

Clustering is a common technique in identifying inherent structures present in a set of objects based on a similarity measure. Clustering methods can be built on the statistical model identification or competitive learning. In this study, we use a Self-Organizing Map (SOM) neural network clustering methodology [*Kohonen*, 1984] for grouping similar parameters obtained from log data of GPK4 into distinct subsets. A

neural network clustering is an unsupervised technique to classify N-dimensional data into two-dimensional output layer of numerous units called neurons. The clustering process is performed from top to bottom, i.e. the general pattern is resolved before going to the details of the lowest levels. This technique is better than the statistical methods for clustering complex data like a geophysical log [Mangiameli *et al.*, 1996]. The neural network toolbox from MATLAB release 2015.b is used. The clustering algorithm is described in Appendix A.

The massive crystalline rock is mechanically isotropic. Hence, we could attribute the variation of mechanical properties to the lithology, the occurrence of fractures and accompanying alteration. Breakout data is also used as it represents the rock strength mechanical at the borehole wall. Hence, the network is run on the magnetic susceptibility, synthetic clay content, fracture, and breakout density data sets (**Figure 5.3.a-d**). Each of the input data has its own sampling rate, i.e. clay content and magnetic susceptibility was measured every 0.25 m while fractures and breakouts were sampled based on their occurrence. Hence, to have the same sample rate, each log is resampled by averaging the values every 4 m. In total four input parameters each containing 145 data points are used.

The number of neurons should be adapted to the input data to achieve a proper learning and classification; it should be considerably smaller than the number of the input samples. The neural network is tested with SOM sizes of 6×6, 8×8, 10×10 and 12×12 neurons and their results are compared. This is an iterative procedure, in which 10000 iterations are performed. It is found that the update to the weight vectors (Appendix A) is negligible after around 1000 iterations have been performed, and the global solution is reached at the end of the iteration. The respective clustering results are shown in **Figure 5.4**. The input data are mapped into around 85% of the number of neurons used for the 6×6 SOM and slightly decreases to around 75% for the 12×12 SOM. However, it can be seen that the results are consistent in all tested SOM sizes.

The input-output mechanism in neural network clustering is determined by the weights, which control the connection of each input to each of the neurons (**Figure 5.5**). They also show the properties of each neuron, e.g. neurons in the top left indicate high magnetic susceptibility, and low clay content, fracture and breakout density. Therefore, the correlation between input data can be estimated from the patterns of the weight of each input; similar trend implies high correlation and vice versa. In general, the magnetic susceptibilities and the density of breakouts and fractures is found to be highly correlated; higher susceptibility (indicated porphyritic granite) has a lower density of fractures and breakouts and vice versa. Clay content is found to be concentrated near fracture zones and has a rather low correlation with lithology, fractures, and breakouts.

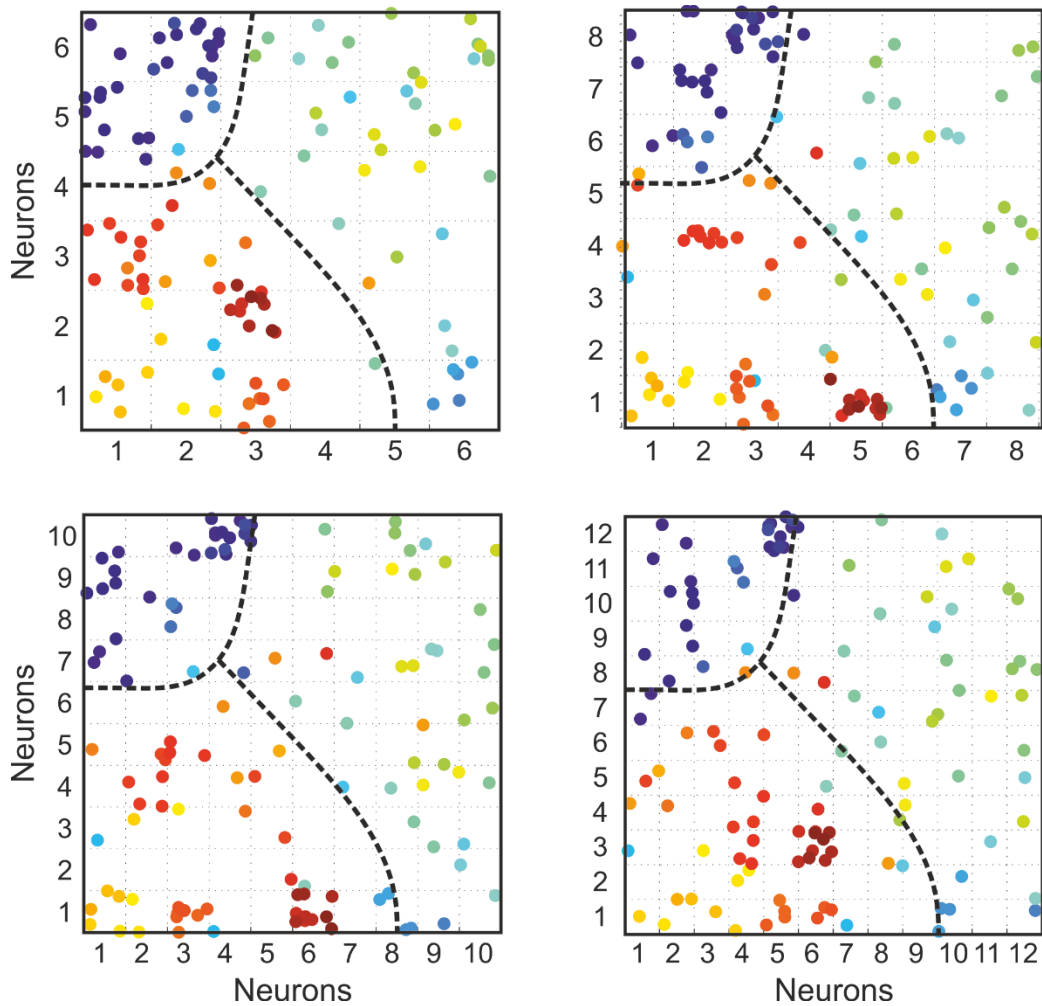


**Figure 5.4:** The map of neuron locations in the topology for the four different numbers of neurons used. Each node represents one combination of all input data at each depth. Clustering (dashed line) is made based on the location of neurons and the depth of the input data.

Neurons that are adjacent to each other in the topology have similar properties. A reservoir zonation is established based on the distance between the neurons and the depth of the samples. Data separated by maximum 150 m depth and 4 neurons from the center of the cluster is considered as one cluster. From the results of SOM clustering and the distribution of data points in the SOM, we can conclude that three distinct zones can be distinguished (**Figure 5.4 and 5.5**):

1. The uppermost zone, from 4400 to 4630 m depth, has a relatively low density of fractures and low clay content. It consists of porphyritic granite, which is only slightly affected by the hydrothermal alteration process. Two major fracture zones intersect the GPK4 well in this zone.
2. The middle zone corresponds to a transition from porphyritic to two-mica granite, between 4630 and 4780 m. It has low to medium density of fractures and breakouts, and a medium to high clay content. In addition, the width of breakouts is found to be very narrow in this zone. GPK4-FZ4910 is intersecting the well in this zone.

3. The lowermost zone, from 4780 to 4980 m, consists of a younger two-mica granite that intrudes into the porphyritic granite. This zone has a medium to high fracture density and a moderate clay content. The density and width of breakouts are found to be the highest in this zone.

The boundaries of those lithologies are also found at similar depth in the GPK2 and GPK3 deep well [Dezayes et al., 2003; Genter et al., 1999] and we assume this is also true for the associated properties.

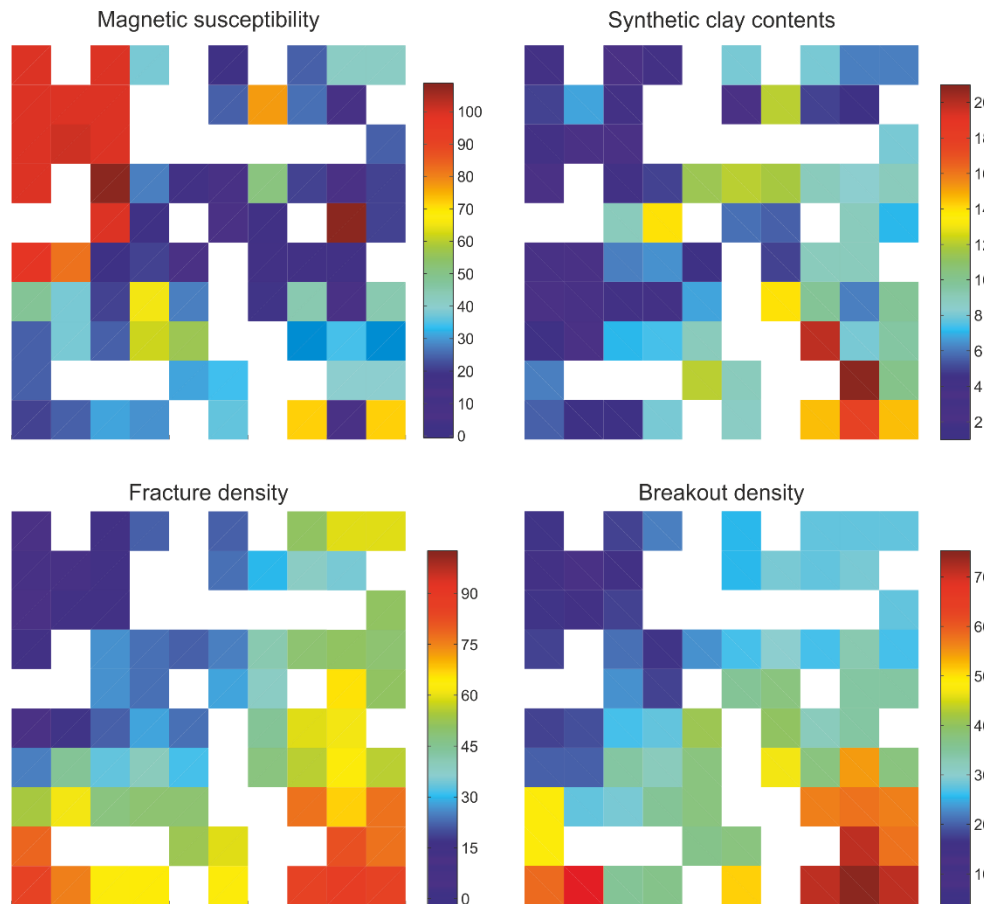


**Figure 5.5:** Map of weight plane of each input parameter: a) magnetic susceptibility, b) synthetic clay contents, d) fracture, and d) breakout density for the 10×10 neuron SOM. Only neurons that have members are plotted.

### 5.3.3 Stress and mechanical properties

The interpretation of the variation of the mechanical properties of the reservoir is made based on the previous in-situ laboratory measurements of Soultz reservoir. Petrophysical analysis of the samples taken from the roller reamer after drilling has revealed that the two-mica granite has a lower density, 2.52 kg m<sup>-3</sup>, compared to the porphyritic granite, 2.62 kg m<sup>-3</sup> [Baillieux et al., 2012]. It has been shown empirically that rock with lower density tends to have lower elastic moduli [Brocher, 2005]. Hence, lower elastic moduli are expected for two-mica granite.



The process of alteration is usually accompanied by an enrichment of clay minerals in the veins and rock matrix, which might act as a zone of weakness [Sausse *et al.*, 2006]. It was found that altered samples in Soultz are characterized by smoother surfaces of fractures [Sausse, 2002], suggesting a lower frictional strength of altered rock. In-situ laboratory measurements have been performed by Valley [2007] to analyze the effect of fractures and alterations on rock mechanical parameters. He showed that the Young's modulus of massive porphyritic Soultz granite is around 54 GPa, and significantly reduced for altered granite. An inverse correlation is found between alteration grade (in terms of clay content) and the mechanical properties of the rock (Table 5.2). In the other fields, it is also shown that the uniaxial compressive strength is also found to decrease with increasing fracture density [Alm *et al.*, 1985]. These observations suggest that the two-mica granite, which has a lower density, higher alteration grade, and higher fracture density, is less stiff compared to the porphyritic granite.

The higher number of borehole breakout occurrence in the two-mica granite compared to the porphyritic granite section (Figure 5.3.d) is also consistent with a reduction of the compressional rock strength as suggested by Haimson and Chang [2000]. Additionally, the asymmetry of the breakouts formed in the two-mica granite is also higher [Sahara *et al.*, 2014], which might be the effect of the higher mechanical heterogeneity of the two-mica granite.

**Table 5.2** Mechanical properties of fractured porphyritic granite in Soultz-sous-Forêts (modified from [Valley, 2007])

	None	Low alteration	Medium alteration	High alteration
UCS (MPa)	105 - 132	88 - 110	95	67
E modulus (GPa)	52 - 58	50 - 55	40	38

In addition, the stress orientations, derived from the orientation of breakouts, are also heterogeneous in the deep reservoir. Figure 5.3.e highlights a systematic variation of the breakout orientation in the vicinity of the major fracture zones. Breakout orientations are shifted by approximately 20° counterclockwise from the  $S_{hmin}$  direction (negative shifting) in the surroundings of the GPK4-FZ4620 fracture zone and align again along the mean  $S_{hmin}$  direction about 50 m below GPK4-FZ4710. A continuous 200 m section of breakout rotation is observed around GPK4-FZ4970 and GPK4-FZ5050. The patterns of breakout orientation suggest that existing fractures affect the stress heterogeneity in the reservoir, especially in the transition and two-mica granite.

#### 5.3.4 Fracture reactivation

Hydraulic stimulation in a deep EGS reservoir has the goal to enhance the reservoir permeability through reactivation of preexisting fractures. Estimating the tendency of fractures to be reactivated during stimulation lets us identify fractures that are most likely to be reactivated. Such an estimate is based on the knowledge of the regional stress field in the reservoir and the relative orientation of fractures to the

principal stresses [Morris *et al.*, 1996]. See Appendix B for further details on this method.

Using the stress profile obtained by [Cornet *et al.*, 2007], and the direction of  $S_{Hmax} = N168^{\circ}E \pm 10^{\circ}$  obtained by Sahara *et al.* [2014], the slip tendency is calculated for all fractures intersecting the open-hole section of the GPK4 well. The uncertainty of the input parameters is taken into account by generating 100 combinations of random numbers within 10% uncertainty range. The value of the slip tendency is normalized to its maximum value for optimally oriented fractures.

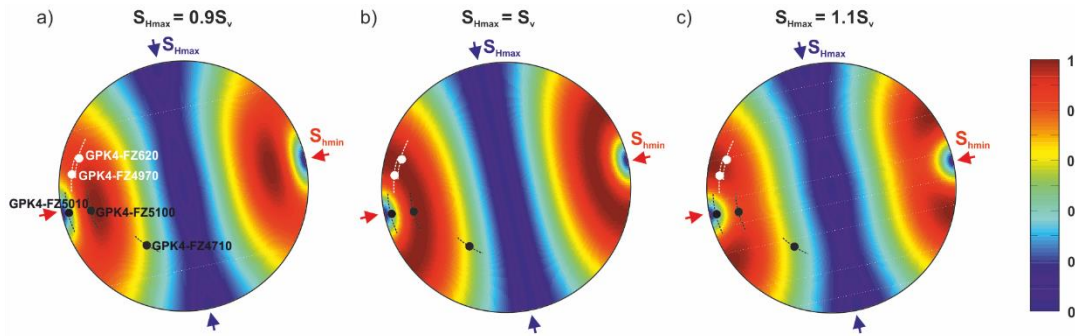


**Figure 5.6:** Slip tendency for three different faulting regimes in Soultz-sous-Forêts. a) Normal fault, b) normal to strike slip and c) strike slip faulting regime. A lower-hemisphere diagram is used to plot the orientation and dip of fractures which have high (red color) and low slip tendency (blue). Solid dots indicate the slip tendency of each fracture zone, while line shows its variation due to the uncertainty of the  $S_{Hmax}$  orientation.

**Figure 5.3.g** shows the mean, first and third quartiles of the slip tendency values for each fracture observed in GPK4 well. In the two-mica granite and the transition zone, not only the density of fracture occurrence is greater, but a larger number of fractures is also found to be have higher slip tendency. Around 80% of fractures observed in two-mica granites have slip tendencies of more than 0.8, while only 53% fractures have such high slip tendency in the porphyritic granite. Therefore, it can be expected that those fractures in the two-mica granite are the first to be reactivated during stimulation.

After Cornet *et al.* [2007], the stress regime in Soultz is normal fault to strike slip. The slip tendency of major fracture zones for different stress regime in Soultz-sous-Forêts is shown in **Figure 5.6**. It can be seen that for a normal faulting regime only GPK4-FZ5100 has high slip tendency while for strike-slip faulting regime both GPK4-FZ4620 and GPK4-4970 have slip tendency of more than 0.8. This is noteworthy as different fracture zones are more likely to be reactivated during stimulation depending on the faulting regime. Focal mechanisms show a mix of normal and strike-slip faulting regime in the Soultz-sous-Forêts crystalline reservoir, with more strike-slip at greater depth [Cuenot *et al.*, 2006]. The strike-slip stress regime in the deep reservoir is also supported by the high differential principal horizontal stress inferred from the occurrence of the wide breakouts observed at the top of two-mica

granite. This suggests that GPK4-FZ4620 and GPK4-FZ4710 are the two major fracture zones that are the most likely to be reactivated during stimulation.

#### 5.4 Induced seismicity due to hydraulic stimulation

We analyze the microseismic events recorded during the GPK4 stimulation to possibly identify the variations of microseismicity patterns associated with the characteristics of the reservoir zonation identified from the borehole data. The hydraulic stimulations in the GPK4 well were conducted twice, in September 2004 and February 2005. The injection lasted about four days for each stimulation, with a total injected volume of 9300 m<sup>3</sup> and 12300 m<sup>3</sup> for the 2004 and 2005 stimulations, respectively. The injection of 2004 stimulation was conducted at a constant injection rate of 30 L/s, except at the end of the third day when the injection rate was increased to 45 L/s for a few hours. Approximately 560 m<sup>3</sup> of NaCl heavy brine, with a density of around 20% higher than fresh water, injected in the first six hours. In the 2005 stimulation, the injection was performed using fresh water only and was divided into three phases: 30 L/s for 24 hours, 45 L/s for 48 hours and 25 L/s for 24 hours. The fluid pressure values at depth (BHP) is determined using an in-house numerical borehole simulator, which uses measured wellhead data (i.e. flow rate, pressure, equivalent NaCl-molality and fluid temperature).

The microseismic catalog of *Dyer* [2005] obtained using three 4-component accelerometers and two 3-component geophones deployed at a various depth ranging from 1500 m to 4500 m is used in this study. 5753 and 3817 microseismic events were localized by the down-hole network during the 2004 and 2005 stimulation, respectively. The location uncertainty of the events is in the order of 50 - 80 m.

To analyze the evolution of microseismicity in the three depth zones defined previously, cross sections of microseismic event density as a function of time are presented in **Figure 5.7**. The two major fracture zones with high slip tendency in a strike-slip stress regime, GPK4-FZ4970, and GPK4-FZ4620, are plotted (**Figure 5.6**). It can be seen in **Figure 5.7** that during the initial period of the 2004 injection (heavy brine), microseismic events are developed first in the two-mica granite. The microseismic events at this period are found to be scattered in a radius of around 170 m from the bottom-hole. At time = 20 hours most of the microseismic events developed near of the GPK4-FZ4970. A cluster of microseismic events in the porphyritic zone begins to develop after the hydraulic injection is increased to 45 L/s for a couple of hours at the end of the 2004 stimulation. At shut in, time = 75 hours, two distinct microseismic clusters are observed in the porphyritic and the two-mica granite zone. A similar pattern of microseismic density is also observed during the 2005 stimulation. This episodic pattern of fracture reactivation, from porphyritic to two-mica granite, is consistent with the variation of the frictional strength of those granites proposed by the borehole data analysis.

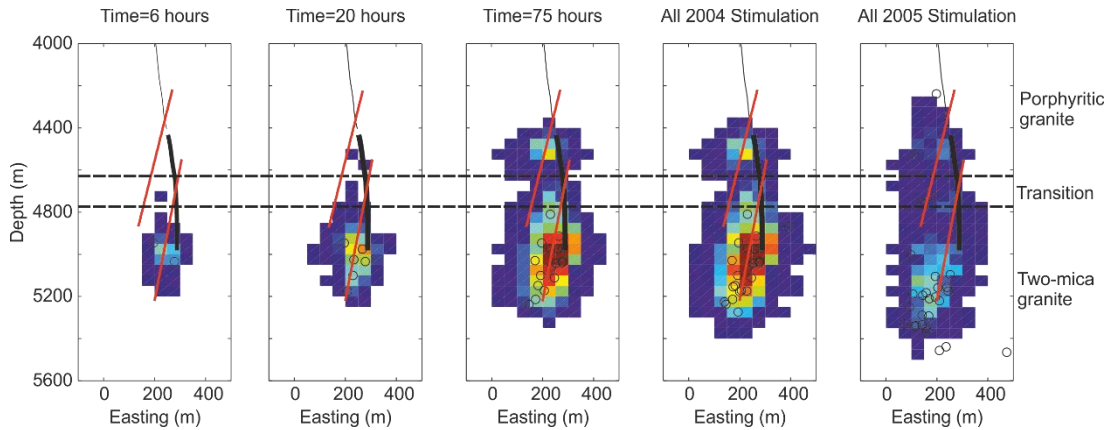


**Figure 5.7:** Microseismic events distribution at a different time and BHP level in N280°E cross sections. Two major fractures, GPK4-FZ4620, and GPK4-FZ4970 are plotted as red lines.

For both stimulations, events at 4670 – 4835 m depth have unique characteristics, i.e. both the density and the magnitude of the microseismic events are very low. This might be related to the high clay content in this transition zone. With a great abundance of clay, aseismic creep might play a significant role. Hence, only a few events of small magnitude were recorded. This low magnitude events pattern in high clay content is also observed during the GPK2 stimulation [Meller and Kohl, 2014]. Furthermore, creep during stimulation of the Soultz-sous-Forêts geothermal field was already suggested by previous works, e.g. Cornet *et al.* [1998b], Bourouis and Bernard [2007] and Schoenball *et al.* [2014a].

On top of this, failure initiation in the surroundings of the borehole as a function of time is analyzed. Events within a distance of 100 m from the wellbore during the first 20 hours after the first event are selected to represent slip on preexisting fractures located near the borehole and which can be statistically representatives of the fractures observed in the well log data. The BHP is also plotted as a function of time to find the corresponding maximum pore pressure perturbation when the microseismic events were recorded.

**Figure 5.8** shows that the first event cluster occurs near the bottom-hole at a depth of around 4980 m when BHP is still below 13 MPa, approximately 9 minutes after injection started. The BHP then increases and stabilizes at around 16 MPa. At the end of the heavy brine injection, the fractures in the entire two-mica granite and transition zone are reactivated, while the fractures in the porphyritic granite remain silent. The fracture set in the porphyritic granite is reactivated approximately 7 hours after fresh water injection started. Interestingly, the failure process in this zone begins with relatively big events followed by weaker events. A similar pattern of fracture reactivation from two-mica to porphyritic is also seen in the 2005 stimulation. Furthermore, the Kaiser effect is evidence in this stimulation; the first events occurred 44 hours after the injection started when BHP exceeded the highest pressure reached during the first stimulation.

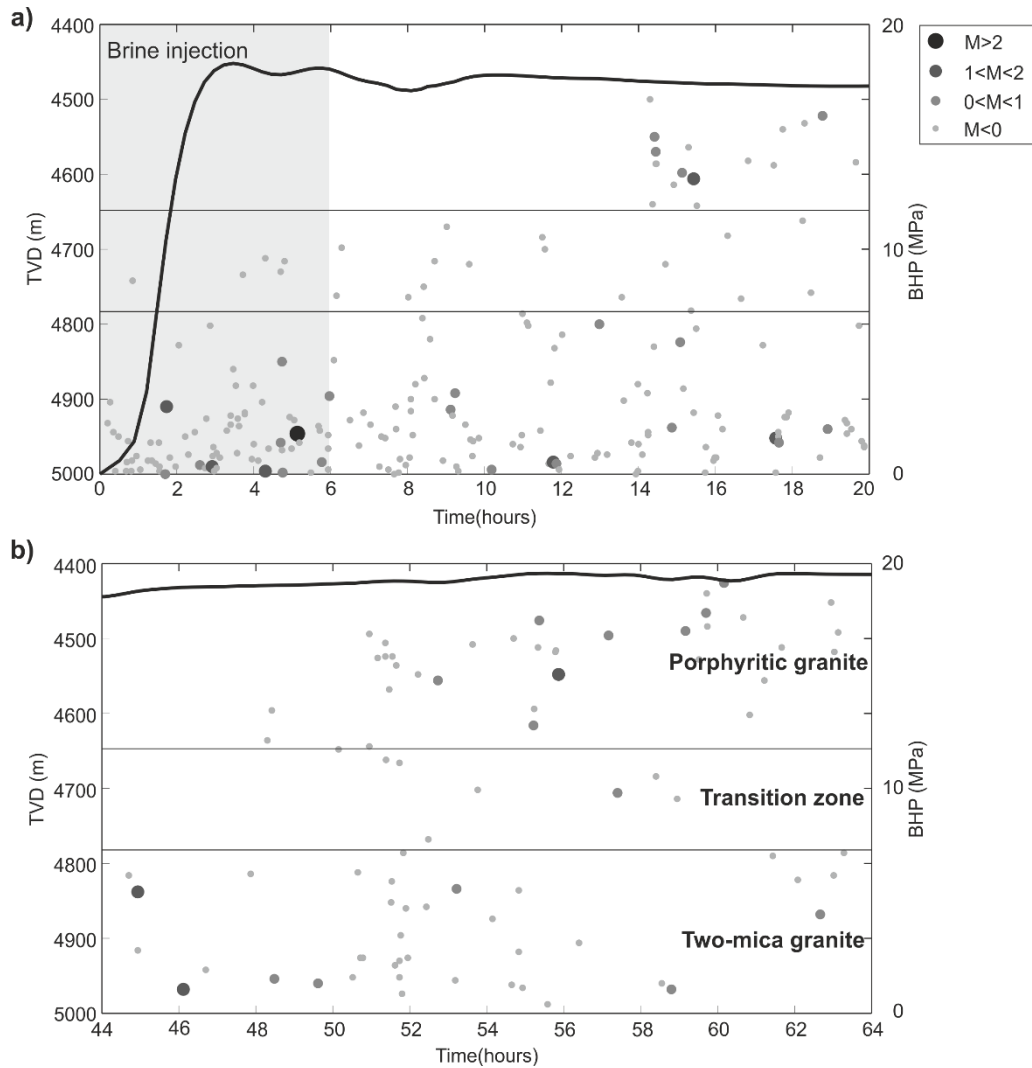


**Figure 5.7:** Microseismic events distribution at a different time and BHP level in N280°E cross sections. Two major fractures, GPK4-FZ4620, and GPK4-FZ4910 are plotted as red lines.

## 5.5 Discussion

This study addresses the question of the main parameters that affect the mechanical properties of the rock and the failure processes during stimulation in the Soultz-sous-Forêts deep reservoir and how we characterize those parameters from an integrated borehole data analysis. The mechanical zonation of the reservoir was made based on the common geophysical logs available in the exploration well. From the neural network clustering, it is found that the lithology, fracture, and breakout play a significant role on the mechanical zonation. The maximum weight of each of those parameters is around four times bigger than the clay content. However, despite its low weight, the variation of the clay content indicates the different failure mechanisms that might occur during stimulation. Care has to be taken when interpreting the mechanical properties from log data; drilling creates a damaged zone

were observed parameters might be different from those away from borehole. Hence, we can only infer the variation of the mechanical properties of the reservoir from the log data.

In this study, the slip tendency is normalized to remove the depth dependency of the principal stress magnitude and the rock is assumed to be cohesionless. Previous studies, e.g. *Cornet et al.* [2007], *Evans et al.* [2005], proposed that fractures in Soultz reservoir should have a cohesion of around 6 MPa to match the field observation. This cohesion reduces the ratio between the shear and normal stress by a maximum of 15%. In this case, the slip tendency shown in **Figure 5.3.g** and **Figure 5.6** is the higher end of possible values. Nevertheless, the pattern of the high and low region of the slip tendency will remain the same. As our purpose is to make a comparison of the slip tendency of preexisting fractures in the different zones, it is enough not to take into account the cohesion. However for a further purpose, e.g. calculating the increasing pressure required to reactivate existing fractures, the cohesion must be taken into consideration.

The results of this study indicate that the different patterns of microseismicity that occur during the GPK4 stimulation correlate very well with the variation of rock characteristics observed from borehole data of the GPK4 well. Interestingly, the similar microseismic pattern is also captured during the GPK2 and GPK3 stimulation (**Figure 5.9**). At the beginning of the stimulation, microseismic events develop first in the two-mica granite section. Then, in contrast to the GPK4 stimulation, a significant amount of microseismic events is observed in the porphyritic granite at the later stage of the injection. It was achieved after about 20000 m<sup>3</sup> of water had been injected, and the injection rate was increased to 50 L/s, higher than the total injected volume and the maximum injection rate of each of the GPK4 stimulation (Table 3). Furthermore, the GPK3 stimulation, in which the highest amount of water had been injected, produced the highest number of microseismic events in the porphyritic granite [*Dyer, 2005*].

**Table 5.3** The hydraulic injection data and the maximum pressure increase of the deep well stimulations in Soultz-sous-Forêts

	Total injected volume (m <sup>3</sup> )				Max pressure increase (MPa)			
	GPK2	GPK3	GPK4a	GPK4b	GPK2	GPK3	GPK4a	GPK4b
<b>1<sup>st</sup> quarter</b>	5215	6000	3045	2770	13	12.7	17.3	16.8
<b>2<sup>nd</sup> quarter</b>	12385	16845	5185	6445	13.8	16.8	17.3	18
<b>3<sup>rd</sup> quarter</b>	19730	26975	7365	10055	14.4	17.3	17.5	18.6
<b>4<sup>th</sup> quarter</b>	22950	34100	9145	12175	14.5	17.3	17.5	18.6

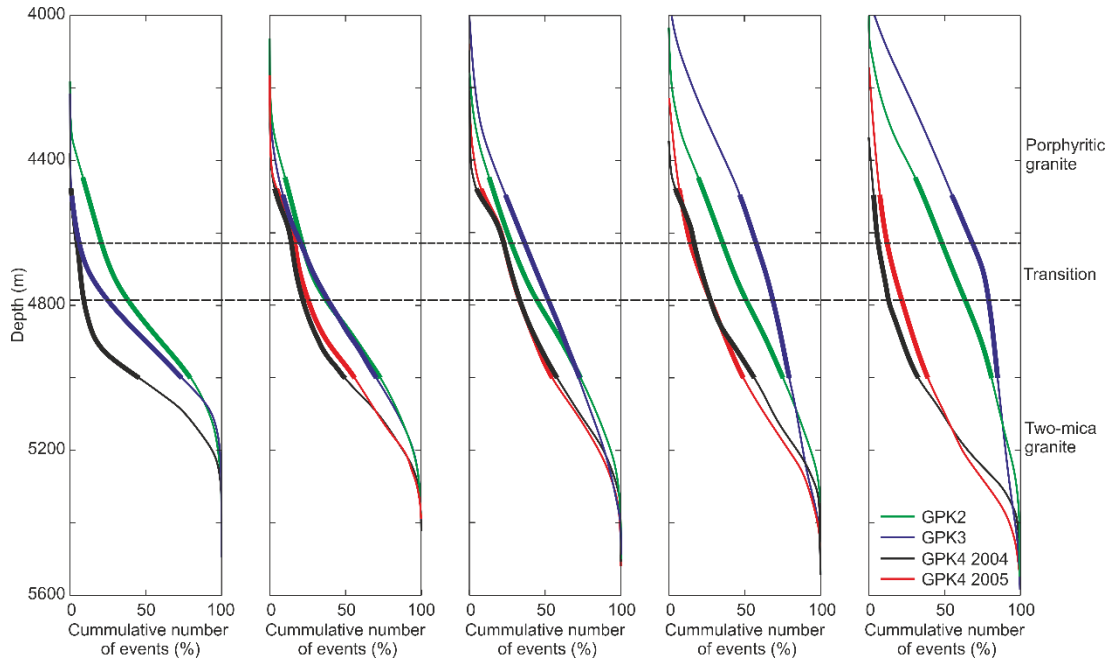


**Figure 5.10:** Evolution of the distribution of microseismic events with increasing injection volume and time.

In this study, the BHP response was less sensitive to the dynamic behavior of the fracture reactivation in the reservoir. From the beginning of the injection, the BHP of the GPK4 well was already 16 – 17 MPa (**Table 5.3**), higher than at the GPK3 and GPK2 stimulation (**Table 3**). *Hasan and Kabir* [2010] mathematically explain the BHP as a function of the injection rate and the injectivity (or permeability) of the rock. The small permeability of the fracture zones intersecting the GPK4 well [*Sausse et al.*, 2010] seems to be the source of this high borehole pressure. Numerical studies show that BHP might only represent the near wellbore condition, and the pressure might decline very fast with distance from the well [e.g. *Kohl and Mège*, 2007]. These might explain the limitation of the fracture reactivations in the two-mica granite, and the smallest number of microseismic events in the GPK4 stimulations, although those stimulations produced the highest BHP.

**Table 5.4** The area of the damaged zone in each lithology for each deep well stimulation. GPK4 is the accumulation of the 2004 and 2005 stimulations.

	<b>Porphyritic granite</b>	<b>Transition zone</b>	<b>Two-mica granite</b>
<b>GPK2</b>	77x10 <sup>6</sup>	15.5 x10 <sup>6</sup>	50.5 x10 <sup>6</sup>
<b>GPK3</b>	129x10 <sup>6</sup>	22x10 <sup>6</sup>	87.5x10 <sup>6</sup>
<b>GPK4</b>	14x10 <sup>6</sup>	4x10 <sup>6</sup>	30.5x10 <sup>6</sup>



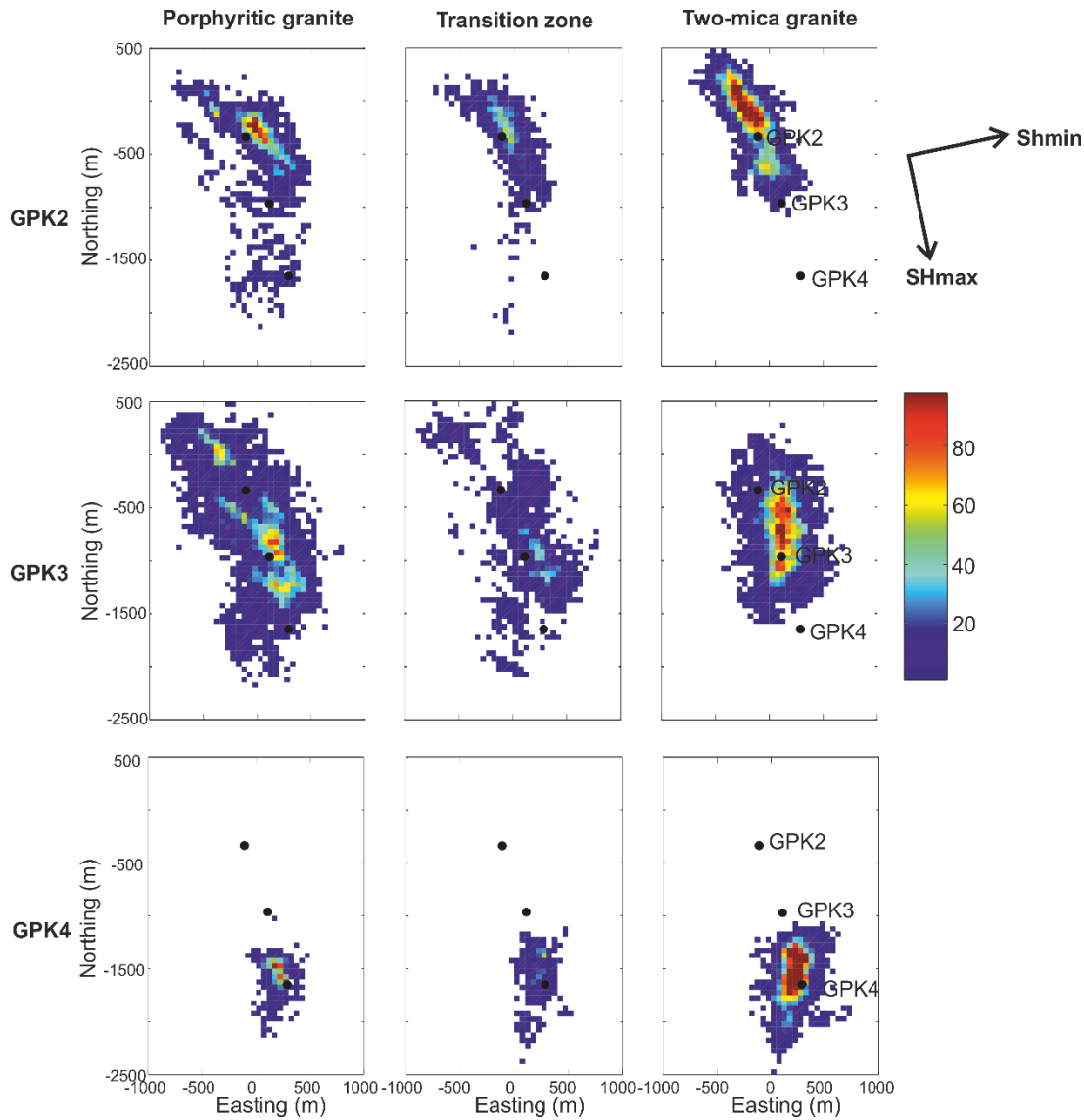


**Figure 5.11:** Map view of microseismic events distribution at different lithologies for all deep well stimulations. The events in GPK4 well is the cumulative of two stimulations performed at 2004 and 2005. Colors indicate number of events per  $50 \times 50 \times 50$  m cell.

The microseismic cloud in each of those three zones is plotted in **Figure 5.10**. The microseismic clouds of the GPK2 stimulation are all aligned in  $N140 \pm 10^\circ E$  direction, makes a  $28 \pm 10^\circ$  angle with respect to the maximum principal stress orientation. Given that the microseismic cloud is nearly vertical, this suggests that the friction coefficient of the major fractures be approximately 0.78. This is in agreement with the high friction coefficient in Soultz reservoir proposed by *Cornet et al.* [2007] and *Evans* [2005]. In the GPK3 stimulation, the rotation of the microseismic cloud orientations from  $N140 \pm 10^\circ E$  in the porphyritic granite to  $N183 \pm 13^\circ E$  in the two-mica granite is consistent with the main direction of the fracture families observed from borehole data in each of the reservoir zones.



It can also be seen in **Figure 5.10** and **Table 5.4** that, except for the GPK4 stimulations, the area of the seismically active zone in porphyritic granite is approximately 1.5 larger than in the one in the two-mica granite. We defined seismically active zone as the area in which contain more than 10 microseismic events. Most of the microseismic events in the two-mica granite are aligned in a plane with a width of around 200 m (red color), which can be interpreted as a fault core. This is in contrast to the diffuse pattern of microseismicity in the porphyritic granite. Furthermore, after shut in, the microseismicity is more developed in the porphyritic than in the two-mica granite (**Figure 5.9**). The different fracture families observed in those two granites could not explain the larger active area in the porphyritic granite; fewer fractures with high slip tendency are observed in the porphyritic granite. However, the variation of the microseismic occurrence time and the damaged area in different granites is also observed during tunneling [Collins and Young, 2000] and volcanic area [Sajid et al., 2016]. Collins and Young [2000] proposed that the effect of the fractures reactivation might be different according to the crystal grain size; it significantly reduces the rock strength of a large grain granite, while the impact is not significant as it is distributed over a larger number of grain boundaries in a small grain granite. It gives us a hint that the variation of the damaged area observed in the Soultz reservoir might also be related to the petrographical features of the granite. **Figure 5.11** shows the mineralogies of the porphyritic and two-mica granites as extracted from core samples in the well EPS1.

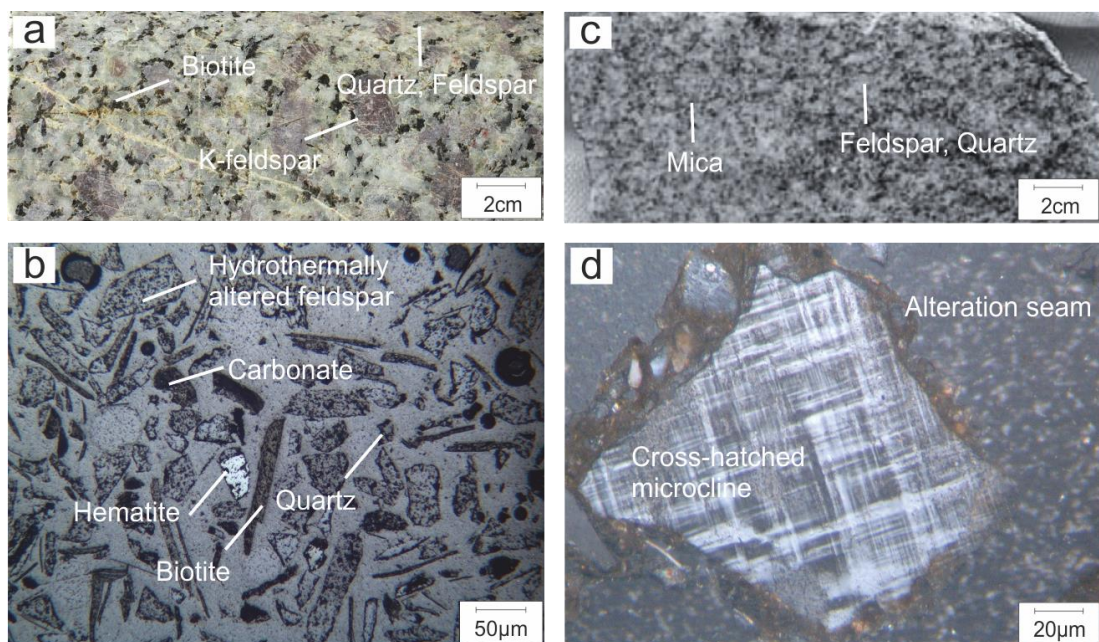


**Figure 5.12:** a) Typical fresh porphyritic granite sample with large K-feldspars in a matrix of quartz, orthoclase and biotite. b) Thin-section of cuttings from the standard granite with typical mineral assemblage and alteration of the mineral grains. c) Sample of the fine-grained two mica granite with a depletion of K-feldspar and a fine matrix of mica, feldspar and quartz. d) thin-section of cuttings from two-mica granite: a characteristic mineral occurring only in the two-mica granite is myrmekite, a cross-hatched microcline.

A fault that acts as a barrier between GPK3 and GPK4 does not intersect any of the deep wells; hence, it could not be identified prior to injection. The extent of this fault is not known. However, it has been shown in this study that the hydromechanical properties of the fault core might not be homogeneous. Furthermore, in the porphyritic section, the microseismic events propagate in a larger area, and the overlapping area of microseismic events between the GPK4 and GPK3 well is observed. Hence, we might expect that a hydraulic connection between those two well could be achieved through the porphyritic section. It gives us a hint that, if hydraulic stimulation is planned to be performed again in the GPK4 well, a different hydraulic stimulation strategy needs to be considered. The next stimulation should target the porphyritic granite by injecting fresh water at higher flow rates and longer duration, comparable to the stimulation of GPK2 and GPK3.

Moreover, the concentration of the microseismic events only in the two-mica granite at the low injection rate GPK4 stimulation, suggests that we might limit the damaged area by appropriately adjusting the stimulation strategy according to the geomechanical model of the reservoir that includes petrographic properties of different reservoir lithologies. This will be particularly importance for deep CO<sub>2</sub> storage and tight oil and gas reservoir fracturing, in which the stimulation shall target a specific formation and not creating new fractures in the seal layer of the reservoir.

## 6.6 Conclusion

---

This study demonstrates that the analysis of the rock characteristics from borehole data proposed in this study is essential to improve the understanding of the geomechanical processes due to hydraulic stimulation. Three zones in the reservoir are identified based on the neural network clustering using various geophysical logs data of the GPK4 well. It is shown that the mechanical zonation of the Soultz crystalline reservoir highly depends on the magnetic susceptibilities, fractures, and breakouts. The interpreted variation of the mechanical properties of the porphyritic and two-mica granite is matched with the episodic fracture reactivation and the different microseismic pattern in those two granites. Furthermore, the clay content provides key information about the area in which creeping mechanism might occur during stimulation. Hence, the combination of those rock characteristics needs to be considered to improve the geomechanical modeling of a fractured granite.

The dynamic pattern of the microseismicity in all deep well stimulations and the different injection strategy was discussed. Despite its low injection rate and total injected volume, the hydraulic stimulation performed in 2004 successfully increases the injectivity index by 20 fold [Nami *et al.*, 2008]. However, due to the occurrence of fault between GPK4 and GPK3 well, which unknown prior to stimulation, the hydraulic connectivity between the two well remained low. Based on the knowledge of the geomechanical properties obtained in this study, a different stimulation strategy for the next stimulation is proposed to increase to hydraulic connectivity of GPK4 well.

The results of this study provide a better understanding of the significance of the mechanical properties characterization in fractured rocks. Careful analysis of log data

can help us learn about the mechanical properties of the fractured granite. The impact of the fracture network on mechanical heterogeneities is very pronounced in crystalline rock, which is mechanically isotropic. This is why we could attribute the variation of the mechanical properties to the occurrence of fractures and accompanying alteration of mechanical properties only. As most of the EGS target the crystalline rock, the understanding of the lithological controls on seismicity in granitic rock is crucial for the future development of the EGS.

## Appendix A

The computing of the SOM employs a training algorithm, where the network analyzes the given input and the Kohonen layer, and the acquired weight vector is tested. The Kohonen layer is designed as a two-dimensional arrangement of the neuron weights that maps N-dimensional input into two-dimensional neurons. The learning algorithm for Kohonen networks is described as follows.

1. Neural network clustering starts with calculating an input vector from selected geophysical logs and arbitrarily defining the weights of each neuron.
2. The output neurons are calculated based on the weights, which are initially random values .
3. The winning neuron for each input vector is selected, that is for which the distance between neuron and input vector is minimal.
4. The weights of the winning neuron and its neighbor are updated according to the average position of all of the input vectors for which it is the winner. The neighborhood size is altered through two phases: an ordering phase and a tuning phase.
  - The ordering phase is performed in the first 200 steps. In this phase, the algorithm adjusts the neighborhood size from 6 (half of the max neurons size used in this study) to 1 neuron. As the network updates the winner and its neighbors in every circle, the result is that neighboring neurons tend to have similar weight vectors and to be responsive to similar input vectors.
  - In the tuning phase, neighborhood distance is less than 1. During this phase, the weights are expected to spread out in more detail while retaining their topological order found during the ordering phase.
5. This process is repeated (back to step 2) until the predefined number of iterations is reached.

A large number of cycles is required to achieve a stable solution; 10000 cycles are performed in this study.

## Appendix B

The fault planes that are more likely to slip are those with a ratio of shear to normal effective stress close to the coefficient of friction,  $\mu$ . The criterion for fracture reactivation is the Mohr-Coulomb criterion, expressed as,

$$\tau = c + \mu \sigma_n \quad (5.1)$$

where  $\tau$  and  $\sigma_n$  are the shear and the normal stresses acting on the fault surface, respectively,  $c$  is the cohesion and  $\mu$  is the coefficient of the sliding friction. In terms of the effective stress,  $\sigma_n^{eff} = \sigma_n - p_f$ , which incorporates the effect of the pore fluid pressure  $p_f$ , the critical condition for sliding on a pre-existing plane of weakness can be written as

$$\mu = (\tau - c) / \sigma_n^{eff} \quad (5.2)$$

The slip tendency of a surface is defined as the ratio of the shear stress to the normal stress on that surface [Morris *et al.*, 1996],

$$T_s = \tau / \sigma_n^{eff} \quad (5.3)$$

The fault planes that would more likely slip are those with a high ratio of shear to the normal effective stress, close in value to the coefficient of friction ( $\mu$ ). The slip-tendency analysis is based on the fact that the slope of the failure criterion, i.e. the coefficient of friction, may span a range of values limited by the Byerlee's experiments [Byerlee, 1978].

At a given stress regime, the assumption of a specific  $\mu$  determines the optimum angle  $\theta$  for sliding,  $2\theta = \tan^{-1}(\mu)$ . This is the most favorable orientation of the fracture plane relative to the direction of maximum principal stress. In this plane the slip tendency is maximum, i.e.  $T_s = T_s^{max}$ . A normalized slip tendency varying between 0 and 1 is defined by dividing the slip tendency by its maximum possible value  $T'_s = T_s / T_s^{max}$ . This normalization make the slip tendency calculated in this study independent from the magnitude of the differential stress, and the value of friction coefficient of the rock. The normalized slip tendency then ranges from 1 near the ideal fault orientation to 0 in the principal stress directions.

---

## Analysis of borehole breakout development using continuum damage mechanics

This chapter has been submitted to International Journal of Rock Mechanics and Mining Sciences.

### Abstract

Damage distribution and evolution have a significant effect on borehole stress concentrations. To model the complex fracturing process and inelastic deformation in the development of the borehole breakout we implement a continuum damage mechanics (CDM) concept that takes tensile and compressive failure mechanisms into account. The proposed approach explicitly models the dissipative behavior of the material due to cracking and its evolution, which leads to an inhomogeneous redistribution of material properties and stresses in the vicinity of the borehole wall. We apply a constitutive plastic model for Berea sandstone and compare our numerical results to laboratory experiments performed on Tablerock sandstone. We are able to reproduce several characteristics of the failure process during the breakout development as observed in experimental tests, e.g. localized crack distribution in the vicinity of the borehole wall, damage evolution, which exhibits a widening process in the beginning followed by subsequent growth in depth, and shear fracturing-dominated breakout growth in sandstone. A comparison of our results with laboratory experiments performed on a range of stress conditions shows a good agreement of the size of borehole breakouts. The importance of the constitutive plastic law in defining the failure mechanisms of the damaging processes is discussed. We show that the depth and the width of breakouts are not independent of each other and no single linear relation can be found between the size of breakouts and the magnitude of the applied stress. Consequently, only one far field principal stress component can be estimated from breakout geometry if the other two principal stresses are known and sufficient data on the plastic parameters are available.

## 6.1 Introduction

---

Continuum damage mechanics (CDM) was developed based on the work of *Kachanov* [1958] and *Rabotnov* [1968], who considered the creep of metal. In this concept, the progressive material damage is used to explain distributed defects in the material and structure that lead to crack initiation and coalescence to fractures. The theoretical framework was not developed further until the work of *Chaboche* [1981] who used the general framework of thermodynamics of irreversible processes. The CDM approach does not prescribe the microcracks that cause the damage, rather it uses a damage parameter to define the effect of damage on the free energy of the system [*Lubliner et al.*, 1989]. CDM has been successfully applied to model the failure process in a wide range of materials, e.g. steel [*Roth and Mohr*, 2014], concrete [*Mazars et al.*, 2014], ceramics [*Deshpande and Evans*, 2008] and others. One of the success factors of this approach stems from the use of a single constitutive model that governs the nonlinear behavior of the material including failure, both in tension and compression [*Lee and Fenves*, 1998].

Modeling the expected degree of damage of a rock mass around cavities is required in many subsurface geotechnical problems such as boreholes and tunnels. The importance of the material properties on the borehole breakout development have been highlighted in some studies, e.g. *Zheng et al.* [1989], *Sahara et al.* [2014] among many others. Several modelling attempts that take into account the changes of the material properties of the rock have been conducted in order to model the damage propagation around boreholes. *Cheatham Jr* [1993] modeled the damage zone around the borehole as a soft inclusion and found that the residual stiffness in soft zones developing due to the damage is sufficient to alter the stress concentration. *Nawrocki and Dusseault* [1995] modeled the damage zone by introducing a radius-dependent Young's modulus around the borehole wall, and calculated the corresponding stress distribution around the borehole. *Detournay and Fairhurst* [1987] further developed the concept for a plastic material. *Gaede et al.* [2013] incorporated anisotropy in a non-linear plastic model. *Schoenball et al.* [2014b] analyzed time-dependent breakout formation with a simplified damage mechanics approach.

Previous laboratory experiments on borehole breakouts have shown that failure of the borehole wall is often governed by two different modes: tensile spalling and shear fracturing [*Vardoulakis et al.*, 1988; *Guenot*, 1989]. Laboratory experiments can be used to study the micromechanical failure of boreholes from the condition of breakouts at the end of an experiment. However, it is difficult to explain the failure processes that lead to the final breakout shape. CDM has led to considerable progress in understanding the onset, development and stabilization of failure. It typically requires extensive testing to determine the relevant constitutive plastic laws as well as the strength and yielding criteria. *Buseti et al.* [2012b] developed a CDM model to describe the progressive damage accumulation that finally leads to brittle failure in Berea sandstone. Uniaxial and triaxial tests were performed to calibrate the model. It was found that the damage and fracturing patterns simulated by the CDM match the experimental features very well.



Herein, we intend to demonstrate that CDM is able to characterize key observations of the transient development of borehole breakouts in an elastoplastic material. Our investigation allows us to account for both tensile and compressive failure. We use the single constitutive law by *Lee and Fenves* [1998] in our modeling scheme. The plastic law obtained *Busetti et al.* [2012b] is used as a basis for the non-linear deformation involved in the simulation. A sensitivity study is performed to analyze the significance of each parameter possibly affecting the dimensions of borehole breakouts. We compare our results to available experimental data from *Ewy and Cook* [1990], *Haimson and Lee* [2004], *Haimson* [2007]. In general, a good match between modeling and laboratory experiment results is achieved.

## 6.2 Theoretical framework

---

### 6.2.1 Fracturing and damage

The failure of most rock materials is a process of crack initiation and propagation. A number of approaches to model those phenomena have been proposed in the past. Many of them were formulated for a linear elastic medium, e.g. fracture mechanics based on the Griffith theory [*Griffith*, 1921]. Fracture mechanics assume that a fracture grows from a small initial crack that amplifies the local stresses at the crack tip and the fracture propagates when the local stresses exceed the strength of the material. Fracture mechanics assesses the strength of a stressed material through the relationship between the loading conditions, the geometry of the crack and the resistance to crack propagation in terms of strain energy release rate (G) or stress intensity factor (K). In this approach the propagation of the fracture is modeled either by cohesive crack tip [*Irwin*, 1957] or a shielding zone. This model is relevant for fracture propagation in rocks that exhibit macroscopic propagation via coalescence of microcracks within a damage front. However the rock stiffness degradation due to the increase of microcrack density [*Kachanov et al.*, 1990; *Heap et al.*, 2010] cannot be modeled with fracture mechanics. Furthermore, as experiments show, there exist inelastic deformations around the crack front which contradict the assumption of a linear elastic medium [*Erdogan*, 2000]. These inelastic deformations could be modeled by taking into account the plasticity in the modeling scheme, i.e. the strain hardening/softening phase due to the accumulation of microcracking [*Reches and Lockner*, 1994]. Macroscopically, this degraded stiffness is linked to the evolution of stress-induced damage that leads to local fracturing and, eventually, to failure [*Katz and Reches*, 2004].

A continuum damage mechanics concept is used in this study to handle the complex fracturing process and the inelastic deformation that cannot be explained by the elastic approach. With this concept the deformation of the material is simulated, based on the damage evolution due to microcrack development, which might better represent the in-situ rock behavior. Unlike the insertion of cohesive or shielding zones, damage propagation is localized within weakening zones that are determined by the plastic deformation. Yielding is characterized by nonlinear inelasticity associated with stress-induced damage accumulation [*Heap and Faulkner*, 2008]. This approach has several advantages. First, field and experimental studies display

inelastic deformation of complex networks of fractures that cannot be explained by elastic analysis. Second, damage mechanics does not require any special assumption, such as initial perturbations or non-realistic high stresses. Third, damage fracturing does not suffer from the present computational limitations of local element enrichment formulations (e.g., the extended finite element method (XFEM) [Moës and Belytschko, 2002]).

### 6.2.2 Continuum damage mechanics (CDM)

With this study we aim to model the typical failure mechanisms occurring around borehole walls shortly after drilling, as observed in laboratory experiments. It was observed that the mechanism of breakout development is governed by tensile spalling and shear fracturing [Vardoulakis *et al.*, 1988; Guenot, 1989]. An attempt was made to model those failure mechanisms by taking into account the different strength criteria for tension and compression in the modeling procedure. Because the responses of a quasi-brittle material to tensile and compressive failure are quite different, it is not sufficient to represent the failure processes by a single parameter. Hence, following [Lee and Fenves, 1998], the parameters of the plasticity used herein are decomposed into a tension and a compression part.

The theory of continuum damage models has been developed using a thermodynamical approach [Chaboche, 1981]. The constitutive equations for this plastic model and its thermodynamic interpretation can be found in Lemaitre [1984]. The essential parameters of the plasticity model are the elastic and plastic strain, which are governed by the hardening rule, the flow rule and the yield criterion.

In the theory of plasticity, the strain tensor  $\varepsilon$  can be decomposed into the elastic and the plastic part. The plastic strain represents all irreversible deformations including those caused by microcracks. Plastic strain will occur if the accumulated stress is larger than the elastic strength of the material, or the yield surface. The CDM approach used herein makes use of the yield function proposed by Lee and Fenves [1998] to account for the different evolutions of strength under tension and compression. In term of stress invariants, the yield function takes the form

$$F = \frac{1}{1-\alpha} (\sqrt{3J_2} + \alpha I_1 + \beta \sigma_{max} - \gamma \sigma_{max}) - \sigma_c(\varepsilon_c^p) = 0 \quad (5.1)$$

with

$$\alpha = \frac{\frac{\sigma_{b0}}{\sigma_{c0}} - 1}{2\left(\frac{\sigma_{b0}}{\sigma_{c0}}\right) - 1}; 0 \leq \alpha \leq 0.5 \quad (5.1.a)$$

$$\beta = \frac{\sigma_c(\varepsilon_c^p)}{\sigma_t(\varepsilon_t^p)} (1 - \alpha) - (1 + \alpha) \quad (5.1.b)$$

$$\gamma = \frac{3(1-K_c)}{2K_c - 1} \quad (5.1.c)$$

where  $I_1 = tr(\sigma)$  is the first stress invariant,  $J_2 = \frac{1}{2} tr(s^2)$  is the second invariant of the deviatoric stress tensor  $s$ ,  $\sigma_{max}$  is the maximum principal stress;  $\frac{\sigma_{b0}}{\sigma_{c0}}$  is the ratio of initial equibiaxial compressive yield stress to initial uniaxial compressive yield stress;  $K_c$  is the stress intensity factor;  $\sigma_t(\varepsilon_t^p)$  is the tensile cohesion stress; and  $\sigma_c(\varepsilon_c^p)$  is the compressive cohesion stress.



A flow rule, which is assumed to be a non-associated potential plastic flow rule, is then used to evaluate the plastic strain. The flow rule can be written as:

$$G = \sqrt{(e \sigma_{t0} \tan \theta)^2 + J_2^{-2}} - I_1 \tan \theta \quad (5.2)$$

where  $\theta$  is the dilation angle measured in the  $I_1 - J_2$  plane at high confining pressure,  $\sigma_{t0}$  is the uniaxial tensile stress at failure; and  $e$  is the eccentricity. For further details on the theoretical description we refer the reader to *Lee and Fenves [1998]* and *Lublimer et al. [1989]*.

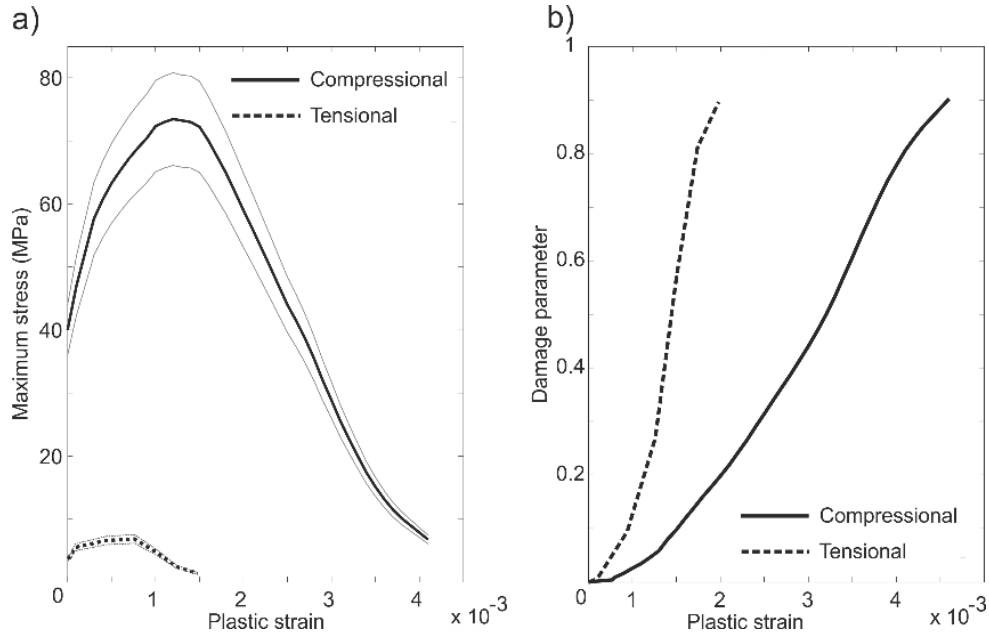


**Figure 6.1:** Plastic law of strain (a) and damage (b) evolution obtained by Buseti et al (2012) for Berea Sandstone. The rock is about 10 times stronger in compression. The grey lines in (a) indicate the 10% variation of the rock strength applied in the parameter study.

The essential step in applying a damage theory concerns the definition of the damage variable. Several procedures have been proposed in the literature to define the damage variable through direct and indirect measurements. The most conventional definition for the damage parameter is to observe and quantify irreversible defects, e.g. intergranular cavities in creep, surface microcracks in fatigue or dimensions of cavities [*Dyson and Mclean, 1977*]. Some problems arise when interpreting these results, especially due to the difficulty in observing defects during the initial phase of the damaging processes. Some indirect damage measurements through physical parameters of the material are also available, e.g. density changes [*Jonas and Baudelet, 1977*] and changes of elastic moduli [*Lemaitre, 1996*]. The elastic moduli variation is used in our CDM approach due to its close relation to the effective stress concept. It is assumed that a damaged volume of material under the applied stress  $\sigma$  shows the same strain response as the undamaged one subjected to the effective stress  $\sigma_{eff}$ .

$$\sigma_{eff} = E_0(\varepsilon - \varepsilon^p) \quad (5.3)$$

$$\sigma_{eff} = \sigma \frac{E_0}{E} = \frac{\sigma}{1-D} \quad (5.3.a)$$

$$D = 1 - \frac{E}{E_0} \quad (5.3.b)$$

in which  $D$  is the isotropic material damage variable which represents the degradation of the elastic stiffness due to increasing plastic strain. Plastic strain and damage can be represented in both the tensile and the compressive domain. The total damage is a function of both damage components:

$$D = 1 - (1 - d_t)(1 - d_c) \quad (5.4)$$

where  $d_t$  and  $d_c$  are the tensile and compressional damage, respectively.

Since the relation between plastic strain and damage parameter highly depends on the rock properties, laboratory measurements are mandatory to define the connection between both parameters. Abundant laboratory tests are available in literature, yet only very few numerical studies have been done to determine the plastic law of a rock based on laboratory data. *Busetti et al.* [2012b] created a numerical model based on the triaxial laboratory measurements on Berea sandstone. A plastic law describing the hardening and damage evolution of the material resulted (**Figure 6.1**). We will use their results and apply it to the wellbore problem.

### 6.3 Numerical Modeling of CDM

The CDM presented has been implemented in a standard finite element program for non-linear analysis. The commercial finite element software Abaqus (Simulia) is used in this simulation. We intend to model the stress concentration around a borehole and the damaging process that follows. Plastic strain is assumed to be caused by the accumulation of microcracks during the damaging process and is decomposed into compressive and tensile part to highlight the different failure mechanisms involved.

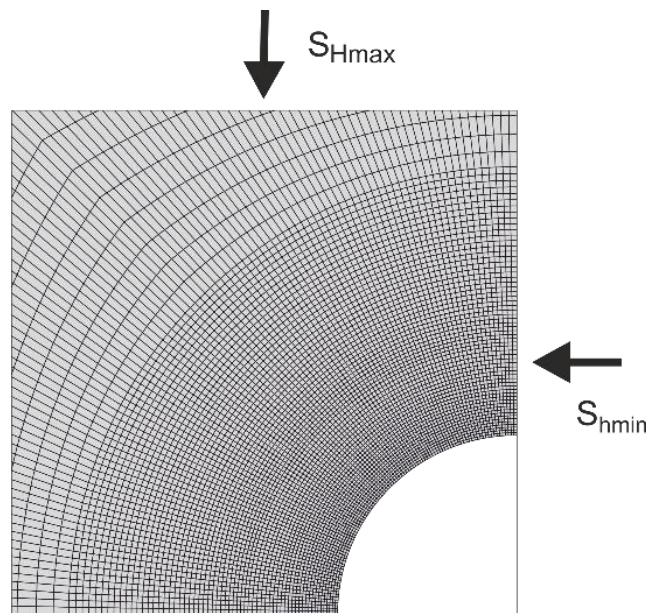


**Figure 6.2:** A close up of the refined mesh around the wellbore.  $S_{Hmax}$  and  $S_{hmin}$  are plotted in vertical and horizontal directions, respectively.

### 6.3.1 Numerical procedure and borehole model

In order to compute the stresses around a vertical wellbore, we model a 2-D slice orthogonal to the wellbore axis. The model is meshed with four-node linear quad elements with mesh density increasing in the vicinity of borehole (**Figure 6.2**). A plane strain assumption is applied in the modeling scheme. Taking advantage of the symmetric stress distribution in an isotropic medium, only a quarter of the wellbore is modeled to reduce the computational time.

We apply the initial stress at the mesh to model the stressed rock in the underground. Displacement boundary conditions are chosen, i.e. the outer nodes are fixed and the inner nodes of the wellbore wall are free. At the beginning of the simulation the nodes at the wellbore wall are fixed to simulate the undisturbed rock. Drilling of the well is simulated by instantaneous release of this boundary condition. The stress invariants at each time step are used with equations 1 and 2 to calculate the plastic deformation at each node. The constitutive plastic law is then used to determine the damage state at each node based on the magnitude of the plastic strain. The effective stress and the stiffness of the material is then updated based on the damage level at each step. Hence, it represents a transient process of damage propagation in a stressed material. The simulation ends after a steady state is reached, i.e. no more plastic deformation accumulates.

It is possible to take into account the effect of the weight of the mud, which usually is used to stabilize the wellbore, by applying a radial pressure to the borehole wall. While in principal any orientation of the wellbore can be modeled by our model set up, results shown hereafter are for the case of a vertical wellbore.

To incorporate the CDM approach, we use the concrete damage plasticity capability of the finite element suite Abaqus [Simulia, 2015]. The Buseti [2012b] plastic law is taken as basis for the CDM model. The damage parameter, for both tensile and compressive damage, is limited up to 90%. This was made to prevent extreme plastic strains at highly damaged elements. Despite this limitation it can be seen in the following results that highly damaged elements show strong plastic deformation. In terms of borehole breakout development, it can be assumed that those elements would be easily washed off by the circulation of the drilling mud during the drilling process and leave a breakout at the wellbore wall.

In a pre-stressed medium, the instantaneous release of the boundary condition at the borehole wall will create rapid deformation around the borehole. Rayleigh damping is used in order to reduce the deformation rate and allow convergence of the solution of the deformation problem. This damping makes the system viscous by creating an additional damping stress proportional to the total strain rate. To prevent numerical artefacts that might occur by introducing damping into the modeling scheme, only a small value of stiffness-proportional Rayleigh damping (0.0015) is used. Another parameter that affects the simulation time is mass scaling [Jing, 2003]. A reduction of the density by a factor of 2 is used in order to reduce the computational time. Hence, although the results showed herein represent the transient process of

damage propagation, our time scale does not correspond to the real time scale these processes occur on [Jing and Hudson, 2002].

The CDM simulation in this study uses the concept of Hillerborg's [Hillerborg et al., 1976] fracture energy-based damage and stiffness degradation in continuum damage mechanics. With this approach the rock's brittle behavior is defined by a stress-displacement response rather than a stress-strain response. This concept is implemented by defining a characteristic length associated with an integration point. By using square elements we reduce possible numerical errors that can occur during modeling of the softening phase of plastic deformation.

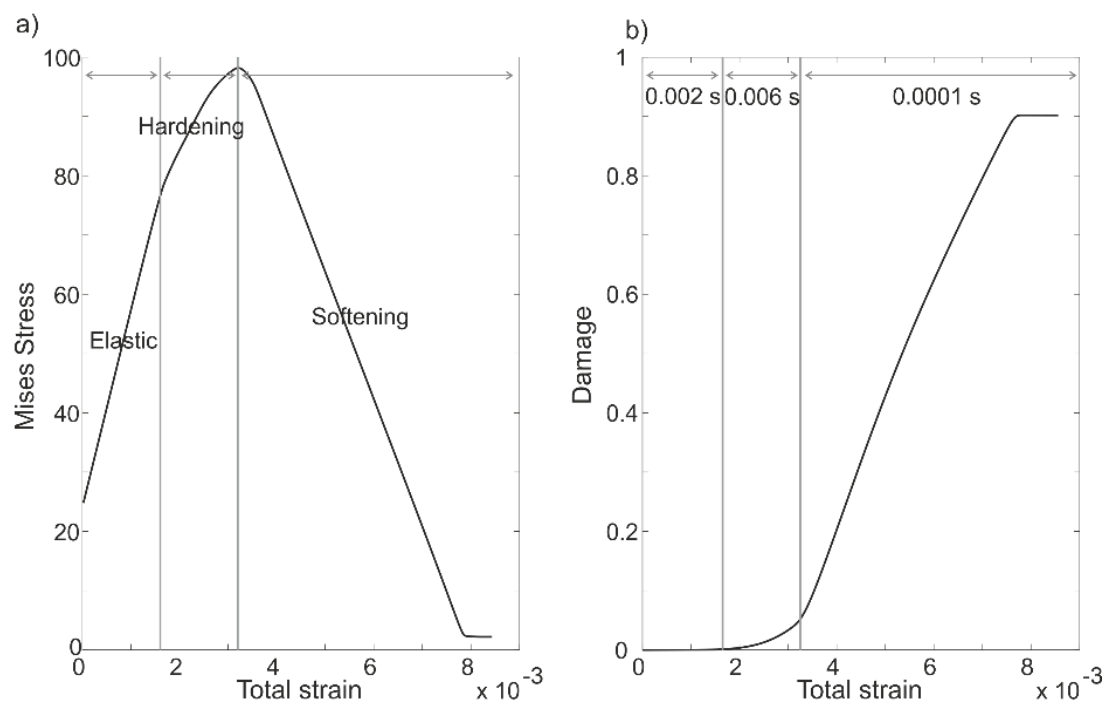


**Figure 6.3:** Graphic of the stress and damage as a function of total strain measured at the first damaged element of the model. The element is located at the borehole wall along the direction of  $S_{hmin}$ .

### 6.3.2 CDM synthetic borehole breakout modeling

The parameters used in this simulation are listed in **Table 6.1**. For testing purposes, the model was first run using an elastic medium and compared to the analytical Kirsch solution [Kirsch, 1898]. A perfect match was obtained between the numerical and the analytical solutions. The code is then run for a synthetic plastic medium with a modified plastic law from *Buseti et al.* [2012b]. A borehole with radius equal to 10 cm is modeled. This model is pre-stressed with a far field effective stress with a magnitude of 25 MPa and 60 MPa for the minimum ( $S_{hmin}$ ) and the maximum horizontal stress ( $S_{Hmax}$ ), respectively, and 40 MPa for the vertical stress ( $S_v$ ). This model is built to represent the production borehole in the typical oil and gas reservoir at depth of around 2.5 km. No mud pressure in excess of the formation pressure stabilizing the well is incorporated in this synthetic test run.

**Figure 3.3** shows the stress and damage evolution as a function of strain in the element at the borehole wall in the direction of the  $S_{hmin}$ . This element is subjected to the highest compressive stress concentration and is the first element to be damaged. At the early step the element is still in the elastic mode. A linear increase of stress with increasing strain is observed. At strain  $\epsilon=0.0015$ , the stress concentration is larger than the yield strength and plastic deformation starts to accumulate. The element is entering the hardening phase of the plastic deformation. At this stage, stress increases with increasing strain but at a lower rate than during the elastic loading. **Figure 6.3.a** shows the stress, strain and damage in the mesh at the end of the hardening phase.  $S_{hmin}$  is plotted in the horizontal direction and, since we focus only on the borehole breakout development, only the region within  $30^\circ$  from  $S_{hmin}$  is plotted in the numerical results showed herein. Only plastic strain is shown in this figure as the purpose is to analyze the development of the plastic deformation in the model. It can be seen that the plastic deformations take place only in the vicinity of the borehole wall and very low plastic strain is present at this stage. The damage value is also very low, which means that the elastic properties of the element is not altered by much, hence the stress concentration is very similar to the one obtained for the elastic medium.

**Table 6.1:** Model parameters for the breakout simulation in Berea sandstone

Density ( $\rho$ )	2100 kg/m <sup>3</sup>
Young's modulus (E)	23.2 GPa
Poisson's ratio ( $\nu$ )	0.17
Dilation angle ( $\theta$ )	15°
Eccentricity ( $e$ )	0.1
Ratio of initial equibiaxial compressive yield stress to initial uniaxial compressive yield stress ( $\frac{\sigma_{b0}}{\sigma_{c0}}$ )	1.16
Stress intensity factor ( $K_c$ )	0.66
Effective maximum horizontal stress ( $S_{Hmax}$ )	60 MPa
Effective minimum horizontal stress ( $S_{hmin}$ )	25 MPa
Effective vertical stress ( $S_v$ )	40 MPa

With increasing time the element then eventually enters the softening phase. This phase occurs very fast and increases the value of both damage and plastic strain significantly to the final damage state. It can be seen in **Figure 6.3.a** that the stress at the damaged element decreases to 3 MPa (very small compared to the 98 MPa at the end of the hardening phase). Interestingly, a high stress concentration is observed at the tip of the damage area. This high stress concentration drives the damage area further inside the rock mass. **Figure 6.4** shows the development of the damage area with time. The elements which have damage value equal to 0.9 in this figure are highly damaged, which means that they would be easily washed off by the circulation of the drilling mud. It can be seen that the damage area propagation is governed by the high stress distribution at the damage front. At the end of the simulation, time  $t=0.1$  s, the second invariant of the stress deviator at the damage

front is very high. However, the first stress invariant is also high. The first stress invariant acts as the normal stress in the Mohr-Coulomb criterion. The increase of the magnitude of this stress invariant makes the stress concentration at the damage front fall below the yield surface. Hence, the model has reached the stable condition. At the end of the simulation, a wide and deep damaged area is formed (**Figure 6.4.d**). In sandstone, under high values of compressive stress, tensile splitting is suppressed and only shear failure, i.e. compressional damage, occurs in this simulation.

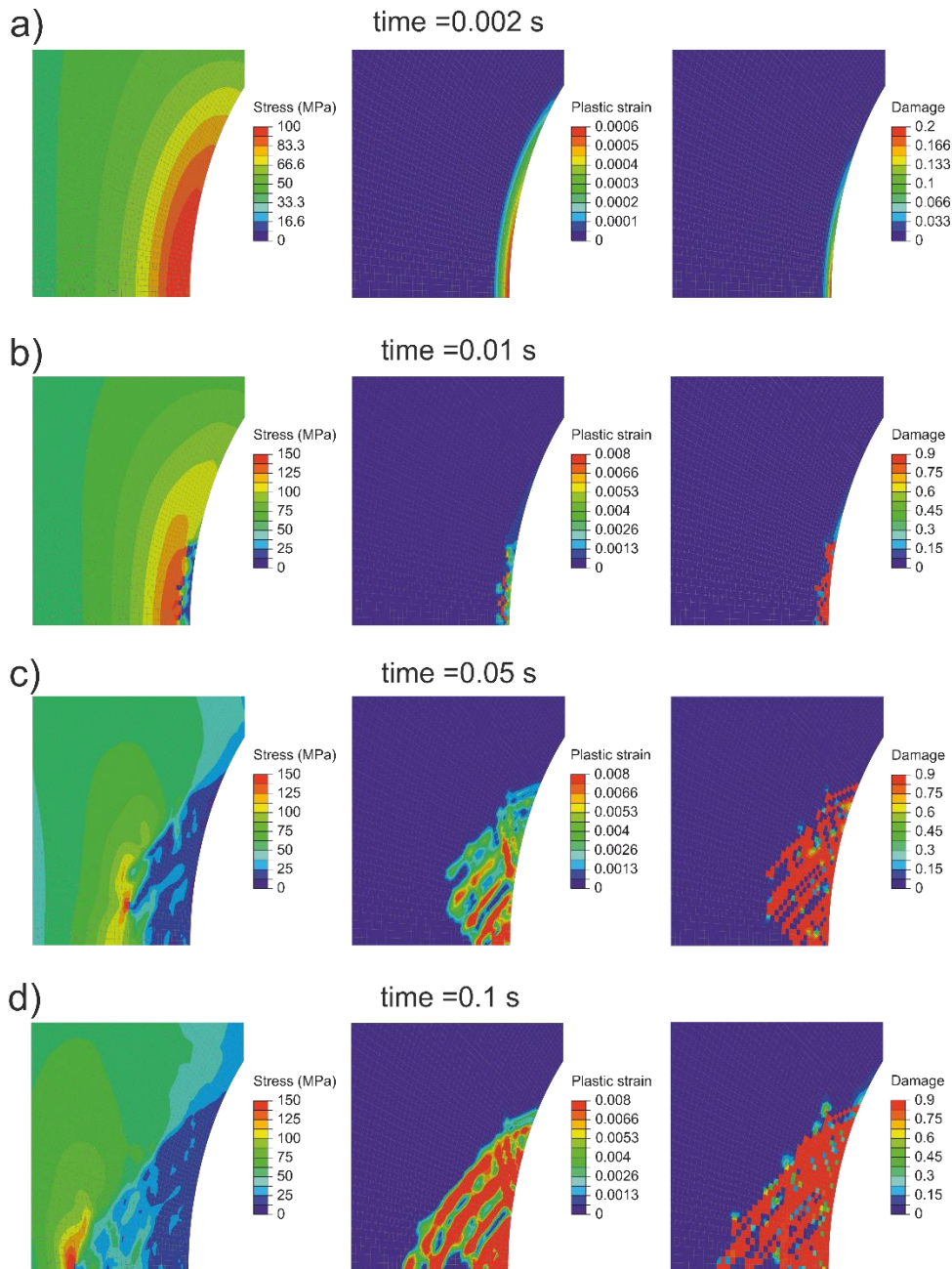


**Figure 6.4:** The evolution of von Mises stress (left), plastic strain (middle) and damage (right) around borehole during simulation. The simulation end after a steady state is reached.



**Figure 6.5** shows the number of damaged elements and the evolution of plastic strain as a function of time. The analysis is done at elements within 1.2 times the borehole radius and within  $30^\circ$  from  $S_{\text{hmin}}$ . This is the area where most of the plastic deformation took place. It can be seen that both the median of plastic strain and the number of damaged elements increases significantly following the damage of the first element (time  $t=0.008$  s). After time  $t=0.06$  s the slope of both graphs decreases and it approaches the stable condition at time  $t=0.095$  s. After this time, no more plastic deformation occurs. The flat line in both graphs starting at time  $t=0.095$  s till the end of the simulation indicates that the simulation has reached a stable equilibrium condition. The time required for the simulation to reach the stable condition depends on the far field stress. High differential stress creates a larger damaged region and requires a longer simulation time.

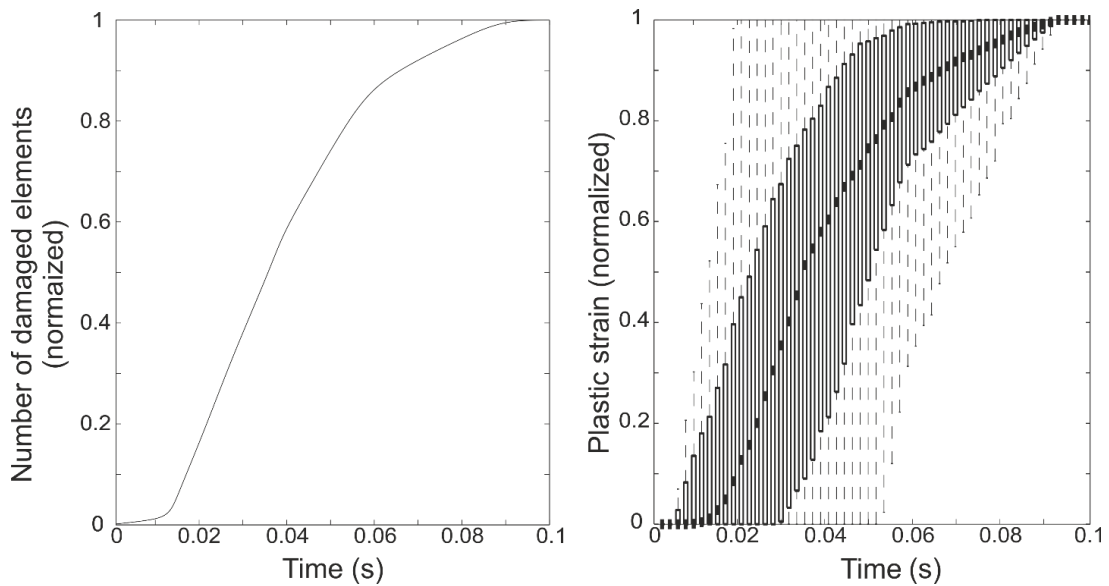


**Figure 6.5:** (a) The evolution of the number of damaged elements and (b) the distribution of plastic strain in all elements as a function of time drawn as boxplots. The values of both parameters are normalized.

### 6.3.3 Sensitivity test

In simulations involving softening processes mesh dependency needs to be accounted for. Several models with element sizes at the wellbore wall ranging from 1.5 mm to 3 mm are used to check the consistency of the results. The outer shape of the damage area is picked as a proxy for the outer boundary of the breakout. The variation of the breakout size is entirely within the element size used. Hence it can be concluded that the geometry of the damage area obtained in our simulation is consistent for different element sizes. Although the element size does not influence the inferred size and shape of breakouts, the internal structure of highly damaged zone obtained in this numerical simulation (**Figure 6.4.d**) is mesh-dependent, i.e. the finer element size the more structures are observed. Hence, we do not interpret this internal structure. A more sophisticated constitutive scheme is required in order to model those local failure processes, e.g. Cosserat continuum [Bazant *et al.*, 1984].

When we compare our simulation with laboratory experiments, one source of discrepancy is the uncertainty in the mechanical parameters reported for laboratory experiments, e.g. Young’s modulus, Poisson’s ratio and the compressional and tensile strength of the material. The influence of each parameter is investigated by a set of simulations where we vary material properties within 10% of their default values listed in **Table 6.1**. **Table 6.2** lists the resulting variation of breakout depth and width for each parameter tested. The geometry variation is represented in percentiles relative to the geometry obtained with the default parameters. It can be seen that the Poisson’s ratio affects breakout size stronger than Young’s modulus both concerning depth and width of the breakout. The strength of the rock affects breakout size the most, as it governs the failure processes in the simulation. In general, it can be concluded that varying the mechanical properties by 10% will vary the breakout size by 12% and 17% for width and depth, respectively.

**Table 6. 2:** The variation of the geometry, width and depth, of the damaged area in percent relative to the one obtained with parameter listed in table 1 for 10% material properties uncertainty

Rock property	Breakout width	Breakout depth
Young’s modulus	7%	10%
Poisson’s ratio	10%	13%
Rock strength (Compressive and tensile)	12%	17%

#### 6.4 Analysis of borehole breakout

An understanding of the breakout phenomenon is important for determining in-situ stress. The relation between the magnitude of the far field stress and size of breakouts is of particular importance for stress measurement using borehole breakouts. Previous studies of borehole breakouts indicated that failure of the borehole wall in a sedimentary rock is often governed by shear fracturing, along one or more shear fractures extending from the borehole wall into the rock [Guenot, 1989; Zoback *et al.*, 1985]. The shear fractures can cause breakouts as they intersect [Shen *et al.*, 2002]. This creates a breakout with a wider area at the borehole wall and a pointy end in the formation. We intend to use the results of the CDM modeling in order to explain the failure processes involve in the breakout development that are typically observed in sedimentary rock.

Based on the numerical modeling results, the very first stage of breakout development is the development of the small plastic strain area very close to the borehole wall in  $S_{hmin}$  direction. This is similar with the initiation of small intergranular cracks at the highest stress-strength ratio area at a low applied stress observed in the laboratory experiments e.g. Haimson [2007], Ewy and Cook [1990]. The damage area cannot penetrate deeper because the overstressed area in the vicinity of the borehole wall does not extend very deep into the rock and the stress level remains below the rock strength.



A set of simulations with applied  $S_{Hmax}$  varying from 45 MPa to 55 MPa is performed in order to understand this low damage stage better. It is found that with increasing applied  $S_{Hmax}$  the plastic strain is also growing but does not enter the softening phase if the magnitude of  $S_{Hmax}$  remains less than 52 MPa. After this critical stress the elements enter the softening strain phase, and the damage propagates further. This softening phase might represent the initiation of fracturing through the matrix that is observed in experiments at high applied stress. The fracture toughness of the matrix is typically weaker, thus cracks will continue to extend following the path of least resistance that takes them into the formation.

It is interesting to note that the breakout grows wider and deeper at the beginning but after time  $t=0.04$  s the damage area only grows deeper. It is in agreement with the hypothesis from the early work of *Zoback et al.* [1985] and *Zheng et al.* [1989] which showed that the redistribution of stress around a broken out borehole deepens the failed zone but does not widen it. The microscopic observation of borehole breakouts in sandstone by *Ewy and Cook* [1990] also revealed the growth of splitting cracks oriented tangential to the borehole wall, starting with a long splitting crack very close to the borehole wall and deepening with a short crack towards the rock formation. *Haimson* [2007] showed (figure 19 in his paper) the spallation zone which develops wider initially before it is deepening during the later stages of breakout formation. We conclude that, at least for sandstone, the CDM model is able to reproduce similar failure features as observed in laboratory experiments.

#### 6.4.1 The effect of far field stress

The results presented in the previous chapter need to be compared with data from field measurements and laboratory tests to assess the reliability of the numerical model developed in this study with the aim to predict the breakout geometry. A direct comparison in the same rock material could not be made. However, *Haimson and Lee* [2004] performed a series of laboratory drilling simulations in Tablerock sandstone samples under varying stress conditions. Both Tablerock and Berea sandstones are arkosic sandstones which have similar characteristics such as porosity around 15%, they contain 50–80% of sub-angular quartz grains, complemented primarily by feldspar, and some clay. They are well cemented with micro-crystalline quartz and clay minerals. Although the mechanical properties of the two sandstones are slightly different (**Table 6.3**), the failure mechanisms that lead to breakout development are similar, i.e. fracturing through the matrix and the development of the episodic spallation zone, while the final shape of both breakouts is also comparable [*Haimson*, 2007]. Therefore, the Buseti plastic law [*Buseti et al.*, 2012b] can still be used for breakout simulation in Tablerock sandstone. A lower value of 18.5 GPa and a higher value of 0.23 were used for Young's modulus and Poisson's ration, respectively, to represent the elastic properties of Tablerock sandstone (**Table 6.3**). A set of simulations with the same applied stress levels as the one applied in *Haimson and Lee* [2004] is performed. This test can be used to find a correlation, between the applied stress and the breakout geometry.

**Table 6.3:** Mechanical properties of Tablerock sandstone and Berea sandstone

Rock property	Tablerock sandstone	Berea sandstone
Elastic modulus	$18.3 \pm 0.14$ GPa	$25.25 \pm 2.14$ GPa
Poisson's ratio	$0.23 \pm 0.07$	$0.25 \pm 0.08$
Uniaxial compressive strength (UCS)	$39.5 \pm 4.8$ MPa	$49 \pm 8.2$ MPa
Tensile strength	$4.4 \pm 0.2$ MPa	$6.8 \pm 3$ MPa

The width and the depth of the breakout for each simulation are plotted in **Figure 6.6**, together with the results from *Haimson and Lee* [2004]. The depth of the breakout is normalized by the radius of the borehole. For most stress conditions the breakout dimensions and specifically its trend with increasing  $S_{Hmax}/S_{Hmin}$  ratio is reproduced very well by our CDM model. A significant deviation of the breakout width is observed for the  $S_{Hmin} = 40$  MPa,  $S_v = 50$  MPa set with a lot wider observed breakouts in the laboratory experiment. The trend with increasing  $S_{Hmax}/S_{Hmin}$  ratio is captured however. For this stress setting the variation of the hoop stress along the borehole wall is relatively weak and hence the breakout zone is weakly localized. The breakout depth however, is matched very well by the simulation. The deviation of breakout depth for the  $S_{Hmax} = 70$  MPa,  $S_{Hmin} = 25$  MPa and  $S_v = 40$  MPa set appears to be caused by an outlier in the laboratory experiments. This demonstrates that there is a considerable uncertainty due to the microdefect of the sample at a granular scale that might affect the experiment results. For the  $S_{Hmin}=20$  MPa,  $S_v=40$  MPa set we do not achieve a satisfactory fit of the trend of breakout depth with increasing  $S_{Hmax}/S_{Hmin}$  ratio. We could only speculate about the reasons but clarification would require a more extensive testing program on Tablerock or Berea sandstones. All other breakout dimensions obtained from our simulations fall within 15% of the corresponding experimental one.

For the set  $S_{Hmax} = 40$  MPa,  $S_{Hmin} = 15$  MPa and  $S_v = 30$  MPa, the borehole wall stays in the hardening phase, hence only small deformation is observed in the vicinity of the borehole wall. This is expected since Berea sandstone has a higher compressional strength compared to Tablerock sandstone (**Table 6.3**). Thus a higher differential stress is required to cause damage in the material. One experiment with a rather extreme horizontal stress ratio of 4.67 could not be simulated (marked with black cross sign). In this extremely high stress ratio the well is squeezed, a rapid deformation towards the  $S_{Hmin}$  direction will occur at a very high strain rate and the numerical calculation did not converge.

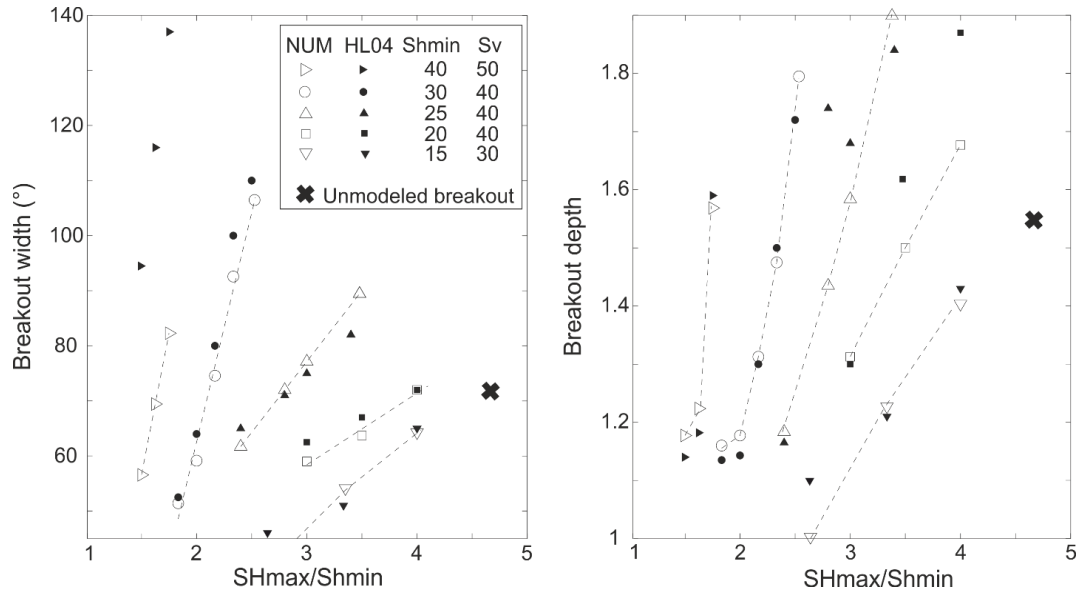


**Figure 6.6:** Variation of the breakout width (a) and the breakout depth normalized with the borehole radius (b) as a function of the far-field horizontal principal stress ratio  $S_{Hmax}/S_{Hmin}$ . Blank and filled marks are for numerical (NUM) and laboratory (HL04) results [20], respectively

In general it can be seen that the numerical and experimental results match quite well. The differences between the numerical and experimental results can be partially explained by the inherent variation of material properties. The CDM concept implemented in this simulation allows us to reproduce breakout geometries obtained through laboratory experiments. Simulation allows furthermore to perform variation of the conditions that could not be achieved in the laboratory experiments, e.g. high temperature and pressure condition, at a greater scale comparable to the reservoir.

It can be seen in **Figure 6.6** that the breakout depth shows a nonlinear trend with increasing applied  $S_{Hmax}$  at fixed  $S_{Hmin}$  and  $S_v$ . At a lower  $S_{Hmax}/S_{Hmin}$  ratio a small increase of breakout depth is observed, but the increase is much stronger towards a higher horizontal stress ratio. This nonlinear pattern is obvious in the high far field stress regime (left side of the **Figure 6.6.b**). A more linear trend is observed between the breakout width and the horizontal stress ratio. However, the gradient of the trend tends to decrease from left to the right, indicating that the width changes are bigger in the higher stress regime. There is a correlation between the depth and the width of breakouts, with both growing with the applied  $S_{Hmax}$  with the constant  $S_v$  and  $S_{Hmin}$ . The implication here is that the two breakout characteristics are not independent of each other and therefore only one far field principal stress can be estimated from breakout geometry information if the other two principal stresses were known in advance.

## 6.5 Discussion and conclusion

The CDM concept can model the onset, evolution and stabilization of failure in borehole breakout. This approach takes into account the changes of the elastic material as a result of the damaging process. Previous experimental studies on

damage mechanics have shown that increasing crack damage within rock alters the elastic moduli in rocks significantly ( *Katz and Reches [2004]*, *Faulkner et al. [2006]*). *Heap et al. [2010]* have conducted experimental measurements of changes in elastic moduli with increasing applied stress on a range of different rock types. They show that the trend in elastic moduli evolution with increasing damage was different for each rock type with Young's modulus decreasing by 11%-32% and Poisson's ratio increasing by up to 600%. The simulation results obtained in this study have shown that already a 10% variation in the elastic properties can significantly affect the geometry of the damaged area. Given the variation of the two elastic parameters obtained in the laboratory, it can be concluded that the geometry of the damaged area formed will vary strongly for different rock types.

Changes of the plastic law do not only affect the geometry of the damaged area, but also the failure mechanism involved in the breakout development. In this study, the damage process is dominated by compression, hence only shear fracturing is observed. *Busetti et al. [2012a]* showed that for Berea sandstone reservoirs, tensile damage starts to develop after the material suffered high plastic damage. In our borehole breakout modeling, the high compressive stress in the vicinity of the borehole prevents the material from having such a high plastic deformation, hence only compressive damage is observed. Failure mechanisms might be different for other rocks. For instance, in crystalline rock a limited degree of plastic deformation occurs on a much shorter time-scale than in Berea sandstone before brittle failure starts [*Borg and Handin, 1966*].

Using CDM we are able to match the key characteristics of the failure process during the breakout development as observed in experimental tests. The development of the damage area is shown to be governed by the stress concentration at the damage front until it dissipates and finally reaches a stable condition. Even with limited experimental data and constitutive plastic laws available, CDM could be successfully applied yielding a good agreement between experimental laboratory and simulation data. We successfully transferred the constitutive relations derived for Berea sandstone and applied it to Tablerock sandstone. This demonstrates the wide applicability of the CDM approach to these kinds of problems.

It has been shown that width and depth of borehole breakouts are not independent of each other and the relation between the geometry of breakouts and the magnitude of the principal stress is non-linear. Our simulations support the hypothesis of *Haimson and Lee [2004]* that only one far-field principal stress components, i.e.  $S_{Hmax}$  in a vertical well, can be estimated from breakout geometry. This requires, however, that the other two principal stresses are known and sufficient appraisal of the constitutive plastic laws exist.

Our effort presented here is in line with the recent focus on plastic deformation in tunneling and drilling. Describing failure is critically dependent on the constitutive plastic law. Hence, additional laboratory testing to determine constitutive plastic laws as well as the strength and yield criteria need to be conducted in order to better understand breakout formation in various types of rock. This modeling scheme could

be developed further by accounting for a poroelastic medium to better represent the in-situ rock condition. A more sophisticated numerical scheme needs to be used to be able to model the localized damage pattern which might represent the spallation processes at the borehole wall. Nevertheless, it was shown that by using elements with aspect ratios close to one, we can explain the complex fracturing process that leads to breakout formation through the continuum damage mechanics concept.

---

## Conclusions and outlook

Analyzing the mechanical properties and the in-situ stress field in a deep EGS field is very challenging, in particular because of the rock experiences different phases of deformation, alteration, weathering and other geological processes which might alter its strength. In a crystalline rock, fractures and hydrothermal alteration are weak links inside rock masses, affecting both its geomechanical and hydraulic properties. In addition, the petrographical characteristic is often an effective indicator for the variation of the rock strength. It has been long assumed that those parameters play an essential role in the reservoir mechanics and hydraulics, particularly in Soultz-sous-Forêts geothermal field. However, sound studies on the mechanical significance of those rock parameters were missing. With this thesis, I demonstrated the mechanical significance of lithological and structural characteristics and their impact on wellbore failures and hydraulic stimulation.

On the basis of field observations and numerical modeling, I show that the approaches developed in this thesis can be used for assessing the variation of stress and mechanical properties within the reservoir. These provide key information for reservoir engineering as the reservoir response to the drilling and fluid injection according to its mechanical properties. A comprehensive study of rock mechanics, from the development of a static geomechanical model to the dynamic response of the reservoir to the fluid injection, in a geothermal field, is presented for the first time in this study.

Field observation was performed to analyze the wellbore failure patterns and to infer parameters that might affect their development. It is a challenging task, in particular because of lacking information on in-situ material properties of the fractured rock. While the mean direction of  $S_{\text{hmin}}$  obtained in this study agrees well with previous studies [e.g. Cornet et al., 2007], careful analysis shows that breakout orientations are systematically affected by the occurrence of fractures.

Detailed analysis of breakout pattern in the vicinity of small fractures shows a direct correlation between the direction of fractures dip and breakouts orientation. This correlation is highest for sections with only one fracture family present and is less in heterogeneous zones with high fracture density and several fracture families. Such correlation suggests that weak zones surrounding the fractures are causing the breakouts to form along the fracture dip directions. With the help of the sonic and petrographic log, the impact of fractures and alteration on mechanical properties of rock in the upper part of the crystalline section is estimated; they affected the compressional strength of the crystalline rock by up to 60%. Due to such a high contrast, wellbore failures might be initiated and formed in the vicinity of such weak zones.

From the stress profile obtained in the GPK4 well, two different mechanisms for the stress heterogeneities are observed: creep-controlled and dip-controlled stress heterogeneities. In this study, I showed the possibility to infer the failure mechanism of fault the pattern of wellbore failures, i.e. occurrence and orientation. Creeping processes cause the reduction of the differential stress with little brittle deformation, thus, prevent the borehole wall from failing in brittle mode. As a result, no wellbore failures were observed. For dip-controlled breakouts, examples of systematic sinusoidal perturbations to breakout orientation were presented. Both patterns reflect the large-scale stress heterogeneity caused by the fracture zones.

The mechanical properties of the fractured rock in the open-hole section of GPK4 well was analyzed further with the help of the magnetic susceptibility, fracture and clay content log. I presented a novel approach of integrating various borehole data represented the main parameters affecting mechanical properties of the rock. Neural network clustering technique was performed to estimate the variation of the mechanical properties in the reservoir. The mechanical zonation of the reservoir is highly controlled by the lithology, fracture, and breakout information. While the clay content values indicate the failure mechanism that might occur during stimulation. Three zones in the deep reservoir intersected by the GPK4 well are proposed. The porphyritic granite, which is less fractured and altered, is interpreted stiffer than the two-mica granite observed in the bottom of the open-hole section. In between, the transition zone is characterized by its high clay content.

After achieving satisfactory results on the characterization of stress and mechanical heterogeneities of the deep Soultz-sous-Forêts reservoir, I use this information to explain the wellbore stability in the GPK4 well. Using the mechanical properties, i.e. Young modulus, Poisson's ratio, and compressional strength, estimated from the integrated borehole data analysis, I am able to model the distribution of the wellbore failures in the GPK4 well. Assuming the dominant faulting regime in the deep Soultz reservoir is strike-slip, the impact of mechanical heterogeneities on wellbore stability is less pronounced in the deviated section of the GPK4 well. The inclination of the well affects the stress distribution by a few MPa which is found to have a significant effect on the development of wellbore, i.e. the pervasive development of compressional and tensile failures in part of the well inclined by less than 10°, and

the delay of compressional failures occurrence by about 700 m in an 25° inclined well. As the dominant fracture families in Soultz is vertical, the advantage of a deviated well is two-fold: it reduces the risk of the wellbore instability and increases the productivity index of the well. The procedure of the mechanical properties assessment and the wellbore failures modeling developed in this study can also be applied in the other fields to better manage the drilling strategy.

In a broader scale, the variation of the mechanical properties in the reservoir also has a profound effect on the induced seismicity due to injection. The sharp mechanical contrast between porphyritic and two-mica granites significantly affect the pattern of the microseismic events; 85% of events are located in the two-mica granite. Furthermore, the microseismic in the two-mica occurred much earlier, when the increase of borehole pressure is still around 3 MPa while fractures in porphyritic granite are reactivated 15 hours later when the borehole pressure stabilized at 15 MPa. Anti-correlation between clay content and microseismic density is also observed. It might be because of the high content of clay mineral in the fracture core. Hence, the rock might be deformed plastically by creeping mechanism. This result provide a field observation evidence of the creep deformation in Soultz proposed in the previous studies, e.g. *Schoenball et al.* [2014a], *Cornet et al.* [1998a]. These findings highlight the lithological and structural controls on induced seismicity due to stimulation.

The dynamic behavior of the deep Soultz reservoir is also captured. During the low injection rate, microseismic events are only concentrated in the highly fractured two-mica granite. This is evidence at the 2004 stimulation, which the injection rate was kept constant at 30 l/s. Subsequently, when the injection rate was increased to 50 l/s during the 2002 and 2003 stimulation, the fracture networks in the porphyritic started to be reactivated. Despite its later occurrence, the injection caused a larger damaged zone in the porphyritic granite. The correlation between the injection scheme and the damaged area observed in this study suggest that an adapted injection strategy might be developed according to the geomechanical model of the reservoir.

On the top of the field observation of the failures in the reservoir, a numerical modeling of the evolution damaging processes during the development of borehole breakouts is presented to gain a better insight into the geomechanical processes in a complex medium. The issue of plastic failure in the development of borehole breakout was only recently investigated. Using CDM, as standard in mechanical damage analysis, I am able to match the key characteristics of the failure process during the breakout development as observed in experimental tests. To our knowledge, the transient processes of plastic deformation during the development of borehole breakout were quantified for the first time using a numerical simulator, especially widening process of a breakout at the early stage and subsequent growth leading to a typical pointy shape. The development of the damaged area is shown to be governed by the stress concentration at the damage front until it dissipates and finally reaches a stable condition. Given the limited experimental data and constitutive plastic laws, CDM applied was successfully yielding a good agreement



between experimental laboratory and simulation data. I demonstrate the broad applicability of the CDM approach to wellbore stability problem. Changes of the plastic law affect not only the geometry of the damaged area but also the failure mechanism involved in the breakout development.

I showed that the width and depth of borehole breakouts are not independent of each other, and the relation between the geometry of breakouts and the magnitude of the principal stress is non-linear. This simulation supports the hypothesis of Haimson and Lee [2004] that only one far-field principal stress component, i.e.  $S_{Hmax}$  on a vertical well, can be estimated from breakout geometry. This requires, however, that the other two principal stresses are known, and sufficient appraisal of the constitutive plastic laws exist. Although comparison with field data is missing in this study, however, we can deduce an indirect confirmation of our approach since the simulation is able to produce the same pointy shape as frequently observed from the log data.

The numerical model was expanded to incorporate the material inhomogeneities as a result of fractures. It improves the analytical formulation of the stress distributions which developed under the homogeneous material assumption, i.e. Kirsch solution (Kirsch, 1898). The stresses distribution around the borehole is governed by the variation of the elastic properties of the rock. Consequently, I present the impact of material inhomogeneity on wellbore failures development as a function of its mechanical contrast and position from the  $S_{hmin}$  direction. The numerical results presented in this study might give us the insight to infer the mechanical properties of fractures and their immediate surroundings from the detailed breakout observation.

I concluded that the comprehensive geomechanical studies performed in this thesis could improve our knowledge in managing the stability of wellbore and engineering a volume of rock consisting of a network of natural and hydraulic-induced fractures that provides sufficient fluid flow pathways. Lithological and structural controls on wellbore failure and induced seismicity is very pronounced in the Soultz geothermal field. Careful analysis of log data can help us learn about the mechanical properties of the fractured granite. The impact of the fracture network on mechanical heterogeneities is very pronounced in crystalline rock, which is mechanically isotropic. This is why we could attribute the variation of the mechanical properties to the occurrence of fractures and accompanying alteration of mechanical properties only. As most of the EGS target the crystalline rock, the understanding of the lithological controls on seismicity in granitic rock is crucial for the future development of the EGS.

Back to the case of Indonesian Geothermal, recent studies, e.g. *Stimac et al.* [2004], *Hochstein and Sudarman* [2008], and [*Carranza et al.*, 2008], show that the permeability of some geothermal reservoirs in a volcanic system is low and, hence, hydraulic stimulation needs to be performed to enhance the permeability. The hydraulic stimulation campaign is recently applied in the Salak geothermal field *Stimac et al.* [2008] and other fields to follow. Due to the high temperature and pressure in a volcanic area, the fluid viscosity and density is significantly reduced. This fluid is

highly dynamic and very reactive to a slight permeability changing in the reservoir. In this case, the concept of the geomechanical model and fracture characteristics obtained in this study need to be applied and developed further to better manage the hydraulic campaign.

The concept of the EGS could suit very well with the plan of Indonesian Government to harvest of the geothermal potential in the eastern part of Indonesia. According to Asian Development Bank report (ADB, 2015), this area has the lowest electrification ratios in Indonesia (less than 60%) with most of the electricity are generated from diesel power plant, which is very expensive. The geothermal potential is not well developed partly because the prospects are dominated by mid enthalpy and the current technique of producing geothermal energy in Indonesia is developed for high-enthalpy system. The development of geothermal technology suit this remote area will boost great social impacts to both the government and society.

Furthermore, the results obtained in this study could also be applied on more general cases. The concept of geomechanical modeling presented here is developed based on standard geological, and geophysical data run in the exploration well and typical geological features that occurred in many areas. Furthermore, the impact of fractures and alterations on mechanical properties is also observed in the sedimentary rock. Hence, they are supposed to be applicable to other geo-reservoir fields. The numerical approach presented here is in agreement with the recently increasing number of the implementation of the plastic deformation assumption used for the modeling in tunneling or earth science. Describing failure is critically dependent on the constitutive plastic law. Hence, additional laboratory testing to determine constitutive plastic laws, as well as the strength and yield criteria, need to be conducted in order to better understand breakout formation in various types of rock. This modeling scheme could be developed further by accounting for a poroelastic medium to better represent the in-situ rock condition.

## References

- AGRCC (2010), Australian code for reporting of exploration results, geothermal resources and geothermal reserves, The geothermal reporting code, The Australian Geothermal Energy Group (AGEG), Adelaide, Australia, <http://www.pir.sa.gov.au>.
- Alm, O., L.-L. Jaktlund, and K. Shaoquan (1985), The influence of microcrack density on the elastic and fracture mechanical properties of Stripa granite, *Physics of the Earth and Planetary Interiors* 40, 161–179.
- Amadei, B. (1996), Importance of Anisotropy when estimating and measuring in situ stresses in rock, *Int. J. Rock Mech. Min. Sci.* 33, 293–325.
- Anderson, E. M. (1951), *The dynamics of faulting and dyke formation: with applications to Britain*, Oliver and Boyd.
- André, L., V. Rabemanana, and F.-D. Vuataz (2006), Influence of water-rock interactions on fracture permeability of the deep reservoir at Soultz-sous-Forêts, France, The deep EGS (Enhanced Geothermal System) project at Soultz-sous-Forêts, Alsace, France, *Geothermics* 35(5–6), 507–531.
- Baillieux, P., E. Schill, L. Moresi, Y. Abdelfattah, and C. Dezayes (2012), Investigation of natural permeability in graben systems, Soultz EGS site (France), in *37th Workshop on geothermal reservoir engineering Stanford University*, pp. SGP-TR-194.
- Baisch, S., R. Weidler, R. Vörös, D. Wyborn, and L. de Graaf (2006), Induced Seismicity during the Stimulation of a Geothermal hfr Reservoir in the Cooper Basin, Australia, *Bulletin of the Seismological Society of America* 96(6), 2242–2256.
- Barbier, E. (2002), Geothermal energy technology and current status: an overview, *Renewable and Sustainable Energy Reviews* 6(1–2), 3–65.
- Baria, R., J. Baumgärtner, A. Gérard, R. Jung, and J. Garnish (1999), European HDR research programme at Soultz-sous-Forêts (France) 1987–1996, *Geothermics* 28(4–5), 655–669.

- Barton, C. A., D. Moos, P. Peska, and M. D. Zoback (1997), Utilizing wellbore image data to determine the complete stress tensor, Application to permeability anisotropy and wellbore stability, *The Log Analyst*, 21–33.
- Barton, C. A., and M. D. Zoback (1994), Stress perturbations associated with active faults penetrated by boreholes, Possible evidence for near-complete stress drop and a new technique for stress magnitude measurement, *Journal of Geophysical Research* 99, 9373–9390.
- Barton, C. A., M. D. Zoback, and D. Moos (1995), Fluid flow along potentially active faults in crystalline rock, *Geology* 23.
- Baujard, C., and D. Bruel (2006), Numerical study of the impact of fluid density on the pressure distribution and stimulated volume in the Soultz HDR reservoir, The deep EGS (Enhanced Geothermal System) project at Soultz-sous-Forêts, Alsace, France, *Geothermics* 35(5–6), 607–621.
- Bazant, Z., T. Belytschko, and T. Chang (1984), Continuum Theory for Strain-Softening, *Journal of Engineering Mechanics* 110(12), 1666–1692.
- Bell, J. S., and D. I. Gough (1979), Northeast-southwest compressive stress in Alberta, evidence from oil wells, *Earth and planetary science letters* 45, 475–482.
- Belytschko, T., and T. Black (1999), Elastic crack growth in finite elements with minimal remeshing, *Int. J. Numer. Meth. Engng.* 45(5), 601–620.
- Borg, I., and J. Handin (1966), Experimental deformation of crystalline rocks, *Tectonophysics* 3(4), 249–367.
- Bott, M. H. P. (1959), The mechanics of oblique slip faulting, *Geological Magazine* 96(2), 109–117.
- Bourouis, S., and P. Bernard (2007), Evidence for coupled seismic and aseismic fault slip during water injection in the geothermal site of Soultz (France), and implications for seismogenic transients, *Geophysical Journal International* 169(2), 723–732.
- Brace, W. F., B. W. Paulding, and C. Scholz (1966), Dilatancy in the fracture of crystalline rocks, *J. Geophys. Res.* 71(16), 3939–3953.
- Brady, B., and E. T. Brown (2005), *Rock mechanics for underground mining*, Springer, New York.
- Brocher, T. M. (2005), Empirical Relations between Elastic Wavespeeds and Density in the Earth's Crust, *Bulletin of the Seismological Society of America* 95(6), 2081–2092.
- Brown, E. T. (1981), *Rock Characterization, Testing and Monitoring. ISRM Suggested Methods* Pergamon press, Oxford.
- Brudy, M., and M. Zoback (1999), Drilling-induced tensile wall-fractures: implications for determination of in-situ stress orientation and magnitude, *International Journal of Rock Mechanics and Mining Sciences* 36(2), 191–215.

- Busetti, S., K. Mish, P. Hennings, and Z. Reches (2012a), Damage and plastic deformation of reservoir rocks, Part 2. Propagation of a hydraulic fracture, *AAPG Bulletin* 96(9), 1711–1732.
- Busetti, S., K. Mish, and Z. Reches (2012b), Damage and plastic deformation of reservoir rock, Part 1. Damage fracturing, *AAPG Bulletin* 96(9), 1687–1709.
- Byerlee, J. (1978), Friction of rocks, *PAGEOPH* 116(4-5), 615–626.
- Cardozo, G. L., and J. H. Behrmann (2006), Kinematic analysis of the Upper Rhine Graben boundary fault system, *Journal of Structural Geology* 28, 1028–1039.
- Carranza, E. J. M., H. Wibowo, S. D. Barritt, and P. Sumintadireja (2008), Spatial data analysis and integration for regional-scale geothermal potential mapping, West Java, Indonesia, *Indonesian geothermal prospects and developments* 37(3), 267–299.
- Chaboche, J. L. (1988), Continuum Damage Mechanics, Part I—General Concepts, *Journal of Applied Mechanics* 55(1), 59–64.
- Chaboche, J.-L. (1981), Continuous damage mechanics — A tool to describe phenomena before crack initiation, *Nuclear Engineering and Design* 64(2), 233–247.
- Chang, C., and B. Haimson (2006), Effect of fluid pressure on rock compressive failure in a nearly impermeable crystalline rock, Implication on mechanism of borehole breakouts, *Engineering Geology* 89, 230–242.
- Cheatham Jr, J. B. (1993), A new hypothesis to explain stability of borehole breakouts, *International Journal of Rock Mechanics and Mining Sciences & Geomechanics Abstracts* 30(7), 1095–1101.
- Collins, D. S., and R. P. Young (2000), Lithological Controls on Seismicity in Granitic Rocks, *Bulletin of the Seismological Society of America* 90(3), 709–723.
- Copeland, P., T. Mark Harrison, and P. Le Fort (1990), Age and cooling history of the Manaslu granite: implications for Himalayan tectonics, *Journal of volcanology and geothermal research* 44(1–2), 33–50.
- Cornet, F. H., T. Berard, and S. Bourouis (2007), How close to failure is a granite rock mass at a 5 km depth?, *Int. J. Rock Mech. Min. Sci.* 44, 47–66.
- Cornet, F. H., J. Helm, H. Poitrenaud, and A. Etchecopar (1998a), Seismic and Aseismic Slips Induced by Large-scale Fluid Injections, in *Seismicity Associated with Mines, Reservoirs and Fluid Injections*, edited by S. Talebi, pp. 563–583, Birkhäuser Basel, Basel.
- Cornet, F. H., J. Helm, H. Poitrenaud, and A. Etchecopar (1998b), Seismic and Aseismic Slips Induced by Large-scale Fluid Injections, in *Seismicity Associated with Mines, Reservoirs and Fluid Injections, Pageoph Topical Volumes*, edited by S. Talebi, pp. 563–583, Birkhäuser Basel.
- Cornet, F. H., and T. Röckel (2012), Vertical stress profile and the significance of stress decoupling, *Tectonophysics* 581, 193–205.

- Cuenot, N., J. Charlety, L. Dorbath, and H. Haessler (2006), Faulting mechanisms and stress regime at the European HDR site of Soultz-sous-Forêt, France, *Geothermics* 35, 561–575.
- D. Goldberg, and B. Zinszner (1989), P-wave attenuation measurements from laboratory resonance and sonic waveform data, *GEOPHYSICS* 54(1), 76–81.
- Deshpande, V. S., and A. G. Evans (2008), Inelastic deformation and energy dissipation in ceramics, A mechanism-based constitutive model, *Journal of the Mechanics and Physics of Solids* 56(10), 3077–3100.
- Detournay, E., and A. H. D. Cheng (1988), Poroelastic response of a borehole in a non-hydrostatic stress field, *International Journal of Rock Mechanics and Mining Sciences & Geomechanics Abstracts* 25(3), 171–182.
- Detournay, E., and C. Fairhurst (1987), Two-dimensional elastoplastic analysis of a long, cylindrical cavity under non-hydrostatic loading, *International Journal of Rock Mechanics and Mining Sciences & Geomechanics Abstracts* 24(4), 197–211.
- Dezayes, C., P. Chevremont, B. Tourliere, G. Homeier, and A. Genter (2005), Geological study of the GPK4 HFR borehole and correlation with the GPK3 borehole (Soultz-sous-Forets, France) *RP-53697-FR*, pp. 94, BRGM.
- Dezayes, C., A. Genter, G. Homeier, M. Degouy, and G. Stein (2003), Geological study of GPK3 HFR borehole (Soultz-sous-Forêts, France), pp. 130, BRGM.
- Dezayes, C., A. Genter, and B. C. Valley (2010), Structure of the low permeable naturally fractured geothermal reservoir at Soultz, *Comptes Rendus Geoscience* 342, 517–530.
- Dyer, B. C. (2005), Soultz GPK4 stimulation September 2004 to April 2005. Seismic monitoring report., GEIE, Soultz-sous-Forets.
- Dyson, B. F., and D. Mclean (1977), Creep of Nimonic 80A in torsion and tension, *Metal Science* 11(2), 37–45.
- Eissa, E. A., and A. Kazi (1988), Relation between static and dynamic Young's moduli of rocks, *International Journal of Rock Mechanics and Mining Sciences & Geomechanics Abstracts* 25(6), 479–482.
- Erdogan, F. (2000), Fracture mechanics, *International Journal of Solids and Structures* 37(1–2), 171–183.
- Evans, K. F. (2005), Permeability creation and damage due to massive fluid injections into granite at 3.5 km at Soultz, 2. Critical stress and fracture strength, *Journal of Geophysical Research* 110, B04204.
- Evans, K. F., A. Genter, and J. Sausse (2005), Permeability creation and damage due to massive fluid injections into granite at 3.5 km at Soultz: 1. Borehole observations, *J. Geophys. Res.* 110(B4), n/a–n/a.
- Ewy, R. T., and N. G. W. Cook (1990), Deformation and fracture around cylindrical openings in rock – II. Initiation, growth and interaction of fractures, *International*

- Journal of Rock Mechanics and Mining Sciences & Geomechanics Abstracts* 27(5), 409–427.
- Faulkner, D. R., T. M. Mitchell, D. Healy, and M. J. Heap (2006), Slip on 'weak' faults by the rotation of regional stress in the fracture damage zone, *Nature* 444, 922–925.
- Fjaer, E., R. M. Holt, P. Horsrud, A. M. Raaen, and R. Risnes (2008), *Petroleum related rock mechanics*, Elsevier, Amsterdam.
- Ford, M., C. Veslud, and O. Bourgeois (2007), Kinematic and geometric analysis of fault-related folds in a rift setting, The Dannemarie basin, Upper Rhine Graben, France, *Journal of Structural Geology* 29.
- Gaede, O., A. Karrech, and K. Regenauer-Lieb (2013), Anisotropic damage mechanics as a novel approach to improve pre- and post-failure borehole stability analysis, *Geophysical Journal International* 193, 1095–1109.
- Gaucher, E., M. Schoenball, O. Heidbach, A. Zang, P. A. Fokker, J.-D. van Wees, and T. Kohl (2015), Induced seismicity in geothermal reservoirs: A review of forecasting approaches, *Renewable and Sustainable Energy Reviews* 52, 1473–1490.
- Genter, A., K. Evans, N. Cuenot, D. Fritsch, and B. Sanjuan (2010), Contribution of the exploration of deep crystalline fractured reservoir of Soultz to the knowledge of enhanced geothermal systems (EGS), *Vers l'exploitation des ressources géothermiques profondes des systèmes hydrothermaux convectifs en milieux naturellement fracturés* On the way to the exploitation of deep geothermal resources in naturally fractured environments 342(7–8), 502–516.
- Genter, A., G. Homeier, P. Chevremont, and H. Tenzer (1999), Deepening of GPK2 HDR borehole, 3880-5090m (Soultz-sous-Forêts, France). Geological Monitoring, pp. 44, BRGM open file report R40685.
- Genter, A., and H. Tenzer (1995), Geological monitoring of GPK2-HDR borehole, 1420-3880 m (Soultz-sous-Forets, France), pp. 46, R38Orleans, BRGM report, France.
- Genter, A., and H. Traineau (1996), Analysis of macroscopic fractures in granite in the HDR geothermal well EPS-1, Soultz-sous-Foretz, France, *Journal of volcanology and geothermal research* 72, 121–141.
- Gérard, A., A. Genter, T. Kohl, P. Lutz, P. Rose, and F. Rummel (2006), The deep EGS (Enhanced Geothermal System) project at Soultz-sous-Forêts (Alsace, France), *Geothermics* 35, 473–483.
- Giardini, D. (2009), Geothermal quake risks must be faced, *Nature* 462(7275), 848–849.
- Griffith, A. A. (1921), The Phenomena of Rupture and Flow in Solids, *Philosophical Transactions of the Royal Society of London A: Mathematical, Physical and Engineering Sciences* 221(582-593), 163–198.
- Guenot, A. (1989), Borehole breakouts and stress fields, *International Journal of Rock Mechanics and Mining Science* 26, 185–195.

- Haimson, B. (2007), Micromechanisms of borehole instability leading to breakouts in rocks, *Int. J. Rock Mech. Min. Sci.* 44, 157–173.
- Haimson, B., and C. Chang (2000), A new true triaxial cell for testing mechanical properties of rock, and its use to determine rock strength and deformability of Westerly granite, *Int. J. Rock Mech. Min. Sci.* 37(1–2), 285–296.
- Haimson, B., and H. Lee (2004), Borehole breakouts and compaction bands in two high-porosity sandstones, *Int. J. Rock Mech. Min. Sci.* 41(2), 287–301.
- Haimson, B., W. Lin, H. Oku, J.-H. Hung, and S.-R. Song (2010), Integrating borehole-breakout dimensions, strength criteria, and leak-off test results, to constrain the state of stress across the Chelungpu Fault, taiwan, *Tectonophysics* 482, 65–72.
- Haimson, B. C. (1978), The hydrofracturing stress measuring method and recent field results, *International Journal of Rock Mechanics and Mining Sciences & Geomechanics Abstracts* 15(4), 167–178.
- Hasan, A. R., and C. S. Kabir (2010), Modeling two-phase fluid and heat flows in geothermal wells, *Journal of Petroleum Science and Engineering* 71(1–2), 77–86.
- Heap, M. J., and D. R. Faulkner (2008), Quantifying the evolution of static elastic properties as crystalline rock approaches failure, *Int. J. Rock Mech. Min. Sci.* 45, 564–573.
- Heap, M. J., D. R. Faulkner, P. G. Meredith, and S. Vinciguerra (2010), Elastic moduli evolution and accompanying stress changes with increasing crack damage, implication for stress change around fault zones and volcanoes during deformation, *Geophysical Journal International* 183, 225–236.
- Heidbach, O., M. Tingay, A. Barth, J. Reinecker, D. Kurfeß, and B. Müller (2008), The world stress map database release 2008 doi, 10.1594/GFZ.WSM.Rel2008.
- Held, S., A. Genter, T. Kohl, T. Kölbel, J. Sausse, and M. Schoenball (2014), Economic evaluation of geothermal reservoir performance through modeling the complexity of the operating EGS in Soultz-sous-Forêts, *Geothermics* 51, 270–280.
- Hillerborg, A., M. Modéer, and P. E. Petersson (1976), Analysis of crack formation and crack growth in concrete by means of fracture mechanics and finite elements, *Cement and Concrete Research* 6(6), 773–781.
- Hochstein, M. P., and S. Sudarman (2008), History of geothermal exploration in Indonesia from 1970 to 2000, *Indonesian geothermal prospects and developments* 37(3), 220–266.
- Hooijkaas, G. R., A. Genter, and C. Dezayes (2006), Deep-seated geology of the granite intrusions at the Soultz EGS site based on data from 5 km-deep boreholes, *Geothermics*, 484–506.
- Hornby, B. E., D. L. Johnson, K. W. Winkler, and R. A. Plumb (1989), Fracture evaluation using reflected Stoneley-wave arrivals, *GEOPHYSICS* 54(10), 1274–1288.



- Hurd, O., and M. D. Zoback (2012), Intraplate earthquakes, regional stress and fault mechanics in the Central and Eastern U.S. and Southeastern Canada, *Tectonophysics* 581, 182–192.
- IEA (2013), Technology roadmap, Geothermal heat and power, pp. 52, International Energy Agency, Paris.
- Irwin, G. R. (1957), Analysis of stresses and strains near the end of a crack, *Journal of Applied Mechanics* 24, 361–364.
- Jaeger, J. C., N. Cook, and R. W. Zimmerman (2007), *Fundamentals of Rock Mechanics*, Blackwell publishing.
- Janssen, C., F. C. Wagner, A. Zang, and G. Dresen (2001), Fracture process zone in granite, a microstructural analysis, *International Journal Earth Sciences (Geol Rundsch)* 90, 46–59.
- Jing, L. (2003), A review of techniques, advances and outstanding issues in numerical modelling for rock mechanics and rock engineering, *Int. J. Rock Mech. Min. Sci.* 40(3), 283–353.
- Jing, L., and J. A. Hudson (2002), Numerical methods in rock mechanics, *Int. J. Rock Mech. Min. Sci.* 39(4), 409–427.
- Jonas, J. J., and B. Baudelet (1977), Effect of crack and cavity generation on tensile stability, *Acta Metallurgica* 25(1), 43–50.
- Julia, F., L. Vladimir, R. Sergey, and Z. David (2014), Effects of hydrothermal alterations on physical and mechanical properties of rocks in the Kuril–Kamchatka island arc, *Engineering Geology* 183, 80–95.
- Kachanov, L. M. (1958), Time of the rupture process under creep conditions, *Izv. Akad. Nauk. {S.S.R.} Otd. Tech. Nauk.* 8, 26–31.
- Kachanov, M., E. L. E. Montagut, and J. P. Laures (1990), Mechanics of crack – microcrack interactions, *Mechanics of Materials* 10(1-2), 59–71.
- Kaiser, P. K., A. Guenot, and N. R. Morgenstern (1985), Deformation of small tunnels –IV. Behaviour during failure, *International Journal of Rock Mechanics and Mining Sciences & Geomechanics Abstracts* 22(3), 141–152.
- Katz, O., and Z. Reches (2004), Microfracturing, damage, and failure of brittle granites, *Journal of Geophysical Research: Solid Earth* 109(B1), B01206.
- King, M. S. (1983), Static and dynamic elastic properties of rocks from the Canadian shield, *International Journal of Rock Mechanics and Mining Sciences & Geomechanics Abstracts* 20(5), 237–241.
- Kirsch, G. (1898), Die Theorie der Elastizität und die Bedürfnisse der Festigkeitslehre, *Zeitschrift des Vereins Deutscher Ingenieure* 42, 797–807.
- Knipe, R. J. (1992), Faulting processes and fault seal, in *Structural and Tectonic Modelling and its Application to Petroleum Geology : Norwegian Petroleum Society*

- Special Publications*, edited by Talleraas, R.M. Larsen H. Brekke B.T. Larsen E, pp. 325–342, Elsevier, Amsterdam.
- Kohl, T., and T. Mégel (2007), Predictive modeling of reservoir response to hydraulic stimulations at the European EGS site Soultz-sous-Forêts, *International Journal of Rock Mechanics and Mining Sciences* 44(8), 1118–1131.
- Kohli, A. H., and M. D. Zoback (2013), Frictional properties of shale reservoir rocks, *J. Geophys. Res. Solid Earth* 118(9), 5109–5125.
- Kohonen, T. (1984), *Self-organization and associative memory*, Heidelberg.
- Larroque, J. M., A. Etchecopar, and H. Philip (1987), Evidence for the permutation of stresses  $\sigma_1$  and  $\sigma_2$  in the Alpine foreland, the example of the Rhine graben, *Tectonophysics* 144, 315–322.
- Le Fort, P., F. Debon, and J. Sonet (1980), The “Lesser Himalayan” cordierite granite belt, typology and age of the pluton of Manserah (Pakistan), *Geol. Bull. Univ. Peshawar* 13, 51–62.
- Ledesert, B., G. Berger, A. Meunier, A. Genter, and A. Bouchet (1999), Diagenetic-type reactions related to hydrothermal alteration in the Soultz-sous-Forêts Granite, France, *European Journal of Mineralogy* 11(4), 731–741.
- Lee, J., and G. L. Fenves (1998), Plastic-damage model for cyclic loading of concrete structures, *Journal of Engineering Mechanics* 124(8), 892–900.
- Lemaitre, J. (1984), How to use damage mechanics, *Nuclear Engineering and Design* 80, 233–245.
- Lemaitre, J. (1996), *A course on damage mechanics*, Springer, Berlin.
- Lin, W., E.-H. Yeh, J.-H. Hung, B. Haimson, and T. Hirono (2010), Localized rotation of principal stress around faults and fractures determined from borehole breakouts in hole B of the Taiwan Chelungpu-fault Drilling Project (TCDF), *Tectonophysics* 482, 82–91.
- Lockner, D. A., and J. D. Byerlee (1993), How geometrical constraints contribute to the weakness of mature faults, *Nature* 363, 250–252.
- Lublinter, J., J. Oliver, S. Oller, and E. Oñate (1989), A plastic-damage model for concrete, *International Journal of Solids and Structures* 25(3), 299–326.
- Lund, J. W., and T. L. Boyd (2015), Direct utilization of geothermal energy 2015 worldwide review, in *World Geothermal Congress 2015*, pp. 1–31.
- Majer, E. L., R. Baria, M. Stark, S. Oates, J. Bommer, B. Smith, and H. Asanuma (2007), Induced seismicity associated with Enhanced Geothermal Systems, *Geothermics* 36(3), 185–222.
- Majorowicz, J., and S. Wybraniec (2010), New terrestrial heat flow map of Europe after regional paleoclimatic correction application, *International Journal of Earth Sciences* 100(4), 881–887, <http://dx.doi.org/10.1007/s00531-010-0526-1>.

- Mangiameli, P., S. K. Chen, and D. West (1996), A comparison of SOM neural network and hierarchical clustering methods, *Neural Networks and Operations Research/Management Science* 93(2), 402–417.
- Mastin, L. (1988), Effect of borehole deviation on breakout orientations, *Journal of Geophysical Research: Solid Earth* 93(B8), 9187–9195.
- Mastin, L., B. Heinemann, A. Krammer, K. Fuchs, and M. D. Zoback (1991), Stress orientation in the KTB pilot hole determined from wellbore breakouts, *Scientific drilling: geophysics, geochemistry and technology* 2, 1–12.
- Mavko, G., and R. Nolen-Hoeksema (1994), Estimating seismic velocities at ultrasonic frequencies in partially saturated rocks, *GEOPHYSICS* 59(2), 252–258.
- Mazars, J., F. Hamon, and S. Grange (2014), A new 3D damage model for concrete under monotonic, cyclic and dynamic loadings, *Mater Struct*, 1–15.
- Meixner, J., E. Schill, J. C. Grimmer, E. Gaucher, T. Kohl, and P. Klingler (2016), Structural control of geothermal reservoirs in extensional tectonic settings: An example from the Upper Rhine Graben, *Journal of Structural Geology* 82, 1–15.
- Meller, C., A. Genter, and T. Kohl (2014a), The application of a neural network to map clay zones in crystalline rock, *Geophysical Journal International* 196(2), 837–849.
- Meller, C., and T. Kohl (2014), The significance of hydrothermal alteration zones for the mechanical behavior of a geothermal reservoir, *Geotherm Energy* 2(1), 12.
- Meller, C., A. Kontny, and T. Kohl (2014b), Identification and characterization of hydrothermally altered zones in granite by combining synthetic clay content logs with magnetic mineralogical investigations of drilled rock cuttings, *Geophysical Journal International* 199(1), 465–479.
- Moës, N., and T. Belytschko (2002), Extended finite element method for cohesive crack growth, *Engineering Fracture Mechanics* 69(7), 813–833.
- Moore, D. E., and D. A. Lockner (1995), The role of microcracking in shear-fracture propagation in granite, *Journal of Structural Geology* 17.
- Moos, D., P. Peska, T. Finkbeiner, and M. Zoback (2003a), Comprehensive wellbore stability analysis utilizing Quantitative Risk Assessment, Borehole Stability, *Journal of Petroleum Science and Engineering* 38(3–4), 97–109.
- Moos, D., P. Peska, T. Finkbeiner, and M. D. Zoback (2003b), Comprehensive wellbore stability analysis utilizing quantitative risk assesment, *Journal of Petroleum Science and Engineering* 38, 97–109.
- Morris, A., D. A. Ferrill, and D. Henderson (1996), Slip-tendency analysis and fault reactivation, *Geology* 24(3), 275–278.
- Mukuhira, Y., H. Asanuma, H. Niitsuma, and M. O. Häring (2013), Characteristics of large-magnitude microseismic events recorded during and after stimulation of a geothermal reservoir at Basel, Switzerland, *Geothermics* 45, 1–17.

- Murphy, H., D. Brown, R. Jung, I. Matsunaga, and R. Parker (1999), Hydraulics and well testing of engineered geothermal reservoirs, *Geothermics* 28(4-5), 491-506.
- Nawrocki, P. A., and M. B. Dusseault (1995), Modelling of damaged zones around openings using radius-dependent Young's modulus, *Rock Mech Rock Engng* 28(4), 227-239.
- Norbury, D., S. Hencher, J. Cripps, and A. Lumsden (1995), The description and classification of weathered rocks for engineering purposes-Geological Society Engineering Group Working Party Report, *Quarterly Journal of Engineering Geology* 28, 207-242.
- Nur, A., and G. Simmons (1969), Stress-induced velocity anisotropy in rock: An experimental study, *J. Geophys. Res.* 74(27), 6667-6674.
- Paillet, F. L., and K. Kim (1987), Character and Distribution of Borehole Breakouts and Their Relationship to in Situ Stresses in Deep Columbia River Basalts, *Journal of Geophysical Research* 92, 6223-6234.
- Pasqualetti, M. J. (2011), Social barriers to renewable energy landscapes, *Geographical Review* 101(2), 201-223.
- Paterson, M. S., and T.-F. Wong (2005), *Experimental rock deformation. The brittle field*, Springer-Verlag, Heidelberg.
- Peška, P., and M. D. Zoback (1995), Compressive and tensile failure of inclined well bores and determination of in situ stress and rock strength, *Journal of Geophysical Research: Solid Earth* 100(B7), 12791-12811.
- Peters, G. (2007), Active tectonics in the Upper Rhine Graben, Integration of Paleoseismology, Geomorphology and Geomechanical modeling, Amsterdam, University, Amsterdam.
- Plumb, R. A., and S. H. Hickman (1985), Stress-induced borehole elongation, A comparison between the four-arm dipmeter and the borehole televiewer in the Auburn Geothermal Well, *Journal of Geophysical Research* 90, 5513-5521.
- Pollack, H. N., S. J. Hurter, and J. R. Johnson (1993), Heat flow from the Earth's interior: Analysis of the global data set, *Rev. Geophys.* 31(3), 267-280.
- Poernomo, A., Satar, S., Effendi, P., Kusuma, A., Azimudin, T., Sudarwo. (2015), An overview of Indonesia Geothermal Development-Current status and its challenges, in *World Geothermal Congress 2015*, pp. 1-11.
- Rabotnov, Y. N. (1968), Kinetics of Creep and Creep Rupture, in *Irreversible Aspects of Continuum Mechanics and Transfer of Physical Characteristics in Moving Fluids, IUTAM Symposia*, edited by H. Parkus and L. I. Sedov, pp. 326-334, Springer Vienna.
- Reches, Z., and D. A. Lockner (1994), Nucleation and growth of faults in brittle rocks, *Journal of Geophysical Research: Solid Earth* 99(B9), 18159-18173.
- REN21 (2013), Renewables 2013 global status report, pp. 178, Paris.

- Ricketts, T. E., and W. Goldsmith (1970), Dynamic properties of rocks and composite structural materials, *International Journal of Rock Mechanics and Mining Sciences & Geomechanics Abstracts* 7(3), 315–335.
- Rigopoulos, I., B. Tsikouras, P. Pomonis, and K. Hatzipanagiotou (2013), Correlations between petrographic and geometrical properties of ophiolitic aggregates from Greece, *Bulletin of Engineering Geology and the Environment* 73(1), 1–12, <http://dx.doi.org/10.1007/s10064-013-0486-3>.
- Roeber, W. L., J. H. Rosenbaum, and T. F. Vining (1974), Acoustic waves from an impulsive source in a fluid-filled borehole, *The Journal of the Acoustical Society of America* 55(6), 1144–1157, <http://scitation.aip.org/content/asa/journal/jasa/55/6/10.1121/1.1914679>.
- Roth, C. C., and D. Mohr (2014), Effect of strain rate on ductile fracture initiation in advanced high strength steel sheets, Experiments and modeling, *International Journal of Plasticity* 56(0), 19–44.
- Rotstein, Y., and M. Schaming (2011), The Upper Rhine Graben (URG) revisited, Miocene transtension and transpression account for the observed first-order structures, *Tectonics* 30, TC3007.
- Rummel, F., and J. Baumgartner (1991), Hydraulic fracturing stress measurements in the GPK1 borehole, Soultz-sous-Forêts, *Geothermal Science and Technology* 3, 119–148.
- Rutqvist, J., A. P. Rinaldi, F. Cappa, and G. J. Moridis (2015), Modeling of fault activation and seismicity by injection directly into a fault zone associated with hydraulic fracturing of shale-gas reservoirs, *Journal of Petroleum Science and Engineering* 127, 377–386.
- Rybach, L. (2003), Geothermal energy: sustainability and the environment, *Selected Papers from the European Geothermal Conference 2003* 32(4–6), 463–470.
- Sahara, D., M. Schoeball, T. Kohl, and B. Mueller (2014), Impact of fracture networks on borehole breakout heterogeneities in crystalline rock, *International Journal of Rock Mechanics and Mining Science*.
- Sahara, D., M. Schoenball, E. Gerolymatou, and T. Kohl (submitted), Analysis of borehole breakout development using continuum damage mechanics, *International Journal of Rock Mechanics and Mining Sciences*.
- Sahara, D. P., M. Schoenball, E. Gerolymatou, and T. Kohl, Analysis of borehole breakout development using continuum damage mechanics, *submitted*.
- Sajid, M., J. Coggan, M. Arif, J. Andersen, and G. Rollinson (2016), Petrographic features as an effective indicator for the variation in strength of granites, *Engineering Geology* 202, 44–54.
- Sanjuan, B., J.-L. Pinault, P. Rose, A. Gérard, M. Brach, G. Braibant, C. Crouzet, J.-C. Foucher, A. Gautier, and S. Touzelet (2006), Tracer testing of the geothermal heat exchanger at Soultz-sous-Forêts (France) between 2000 and 2005, The deep EGS

- (Enhanced Geothermal System) project at Soultz-sous-Forêts, Alsace, France, *Geothermics* 35(5-6), 622-653.
- Sausse, J. (2002), Hydromechanical properties and alteration of natural fracture surfaces in the Soultz granite (Bas-Rhin, France), *Tectonic Processes and the Flow of Mineralising Fluids*, *Tectonophysics* 348(1-3), 169-185.
- Sausse, J., C. Dezayes, L. Dorbath, A. Genter, and J. Place (2010), 3D model of fracture zones at Soultz-sous-Forêts based on geological data, image logs, induced microseismicity and vertical profiles, *Comptes Rendus Geoscience* 342, 531-545.
- Sausse, J., M. Fourar, and A. Genter (2006), Permeability and alteration within the Soultz granite inferred from geophysical and flow log analysis, The deep EGS (Enhanced Geothermal System) project at Soultz-sous-Forêts, Alsace, France, *Geothermics* 35(5-6), 544-560.
- Sayers, C. M. (1994a), The elastic anisotropy of shales, *J. Geophys. Res.* 99(B1), 767-774.
- Sayers, C. M. (1994b), The elastic anisotropy of shales, *J. Geophys. Res.* 99(B1), 767.
- Schoenball, M., L. Dorbath, E. Gaucher, J. F. Wellmann, and T. Kohl (2014a), Change of stress regime during geothermal reservoir stimulation, *Geophys. Res. Lett.* 41(4), 1163-1170.
- Schoenball, M., D. P. Sahara, and T. Kohl (2014b), Time-dependent brittle creep as a mechanism for time-delayed wellbore failure, *Int. J. Rock Mech. Min. Sci.* 70(0), 400-406.
- Scholz, C. H. (2002), *The mechanics of earthquake and faulting - 2nd edition*, Cambridge University Press, Cambridge.
- Shamir, G. (1990), Crustal stress orientation profile to a depth of 3.5km near the San Andreas fault at Cajon Pass, California, University, Stanford, Stanford.
- Shamir, G., and M. D. Zoback (1992), Stress orientation profile to 3.5 km depth near the San Andreas Fault at Cajon Pass, California, *Journal of Geophysical Research* 97(B4), 5059-5080.
- Shen, B., O. Stephansson, and M. Rinne (2002), Simulation of Borehole Breakouts using FRACOD2d, *Oil and gas Science and Technology* 57, 579-590.
- Shen, B., O. Stephansson, and M. Rinne (Eds.) (2014), *Modelling rock fracturing processes. A fracture mechanics approach using FRACOD*, pp. 171, Springer, Heidelberg.
- Sibson, R. H. (1977), Fault rocks and fault mechanisms, *Journal of the Geological Society* 133, 191-213.
- Simmons, G., and W. F. Brace (1965), Comparison of static and dynamic measurements of compressibility of rocks, *J. Geophys. Res.* 70(22), 5649-5656.
- Simulia (2015), Concrete damaged plasticity, Abaqus, Rode Island.

- Sousa, L. M. O. (2012), The influence of the characteristics of quartz and mineral deterioration on the strength of granitic dimensional stones, *Environmental Earth Sciences* 69(4), 1333–1346, <http://dx.doi.org/10.1007/s12665-012-2036-x>.
- Stimac, J., G. Nordquist, A. Suminar, and L. Sirad-Azwar (2008), An overview of the Awibengkok geothermal system, Indonesia, *Indonesian geothermal prospects and developments* 37(3), 300–331.
- Stimac, J. A., T. S. Powell, and G. U. Golla (2004), Porosity and permeability of the Tiwi geothermal field, Philippines, based on continuous and spot core measurements, *Philippine Geothermal Systems Response to Production* 33(1–2), 87–107.
- Straub, A., U. Krüchel, and Y. Gros (1991), Borehole electrical imaging and structural analysis in a granitic environment, *Geophysical Journal International* 106(3), 635–646.
- Strouboulis, T., K. Copps, and I. Babuška (2001), The generalized finite element method, *Computer Methods in Applied Mechanics and Engineering* 190(32–33), 4081–4193.
- Tembe, S., D. A. Lockner, and T.-F. Wong (2010), Effect of clay content and mineralogy on frictional sliding behavior of simulated gouges: Binary and ternary mixtures of quartz, illite, and montmorillonite, *J. Geophys. Res.* 115(B3), n/a-n/a.
- Terzaghi, K. (1923), Die Berechnung der Durchlässigkeitsziffer des Tonnes aus dem Verlauf der Hydrodynamischen Spannungserscheinungen, *Sitzungsber. Akad. Wiss., Wien Math. Naturwiss. Kl.* 132, 105–124.
- Teufel, L. W. (1991), Influence of lithology and geologic structure on in situ stress: examples of stress heterogeneity in reservoirs, in *Reservoir Characterization II*, edited by Wesson, Larry W. Lake Herbert B. Carroll Thomas C, pp. 565–578, Academic Press.
- Thomsen, L. (1986), Weak elastic anisotropy, *GEOPHYSICS* 51(10), 1954–1966.
- US Department of Energy (2006), The future of geothermal energy, Impact of enhanced geothermal system (EGS) on the United States in the 21st century, *An assesment by an MIT-led interdisciplinary panel*, MIT, Idaho.
- Valley, B. C. (2007), The relation between natural fracturing and stress heterogeneities in deep-seated crystalline rocks at Soultz-sous-Forets (France), Swiss Federal Institute of Technology Zurich, Zurich.
- Vardoulakis, I., J. Sulem, and A. Guenot (1988), Borehole instabilities as bifurcation phenomena, *International Journal of Rock Mechanics and Mining Sciences & Geomechanics Abstracts* 25(3), 159–170.
- Vermilye, J. M., and C. H. Scholz (1998), The process zone, A microstructural view of fault growth, *Journal of Geophysical Research* 103, 12223–12237.

- Zang, A., H. Berckhemer, and M. Lienert (1996), Crack closure pressures inferred from ultrasonic drill-core measurements to 8 km depth in the KTB wells, *Geophysical Journal International* 124(3), 657–674.
- Zang, A., O. Stephansson, and A. Zang (2010), *The stress field of the earth's crust // Stress field of the Earth's crust*, Springer, Heidelberg.
- Zang, A., K. Wolter, and H. Berckhemer (1989), Strain recovery, microcracks and elastic anisotropy of drill cores from KTB deep well, *Scientific drilling: geophysics, geochemistry and technology* 1, 115–126.
- Zemanek, J., E. E. Glenn, L. J. Norton, and R. L. Caldwell (1970), Formation evaluation by inspection with the borehole televiewer, *GEOPHYSICS* 35(2), 254–269.
- Zheng, Z., K. Kemeny, and N. Cook (1989), Analysis of borehole breakouts, *Journal of Geophysical Research* 94(B6), 7171–7182.
- Ziegler, P. A. (1994), Cenozoic rift system of western and central Europe, an overview, *Geologie en Mijnbouw* 73, 99–127.
- Zoback, M. D. (2007), *Reservoir Geomechanics*, Cambridge University Press, New York.
- Zoback, M. D., C. A. Barton, M. Brudy, C. D. A, T. Finkbeiner, B. R. Grollmund, D. Moos, P. Peska, C. D. Ward, and D. J. Wiprut (2003), Determination of stress orientation and magnitude in deep wells, *Int. J. Rock Mech. Min. Sci.* 40, 1049–1076.
- Zoback, M. D., D. Moos, L. Mastin, and R. N. Anderson (1985), Wellbore breakouts and in situ stress, *Journal of Geophysical Research* 90, 5523–5530.



# Declaration of authorship

## **Study 1: Impact of fracture networks on borehole breakout heterogeneities in crystalline rock.**

Citation:

Sahara, D., M. Schoeball, T. Kohl, and B. Mueller (2014), Impact of fracture networks on borehole breakout heterogeneities in crystalline rock, *International Journal of Rock Mechanics and Mining Science*.

This study is funded by the Indonesia Directorate General of Higher Education (DIKTI), the German Academic Exchange Service (DAAD) and Energie Baden-Wuerttemberg (EnBW). In this study, I analyze in detail the stress perturbations associated with all fractures observed from borehole image log data. The purpose of this study was to gain a better understanding of the impact of the natural fracture network on breakout heterogeneities in granite rock. I picked every 20 cm the orientation, width, and depth of the borehole breakouts observed in the Ultrasonic Borehole Imager (UBI) log of GPK4 well. The natural fractures data was provided by the French Geological Agency (BRGM). I conducted all the calculations, interpreted the results and wrote the manuscript.

## **Study 2: Analysis of state of stress in fractured crystalline reservoirs**

Citation:

Sahara, D. P., M. Schoenball, B. Mueller, and T. Kohl (2015), Analysis of Stress Heterogeneities in Fractured Crystalline Reservoirs, in Proceedings World Geothermal Congress 2015, IGA.

This study is funded by the Indonesia Directorate General of Higher Education (DIKTI), the German Academic Exchange Service (DAAD) and Energie Baden-Wuerttemberg (EnBW). In this study, I estimate the in-situ stress of Soultz-sous-Forêts and its heterogeneity. Basis for the analysis were the breakouts data obtained in the previous study [Sahara *et al.*, 2014] and drilling-induced tensile failures data picked in this study. I analyzed the wellbore failures in detail and made the interpretation of the different wellbore failures types observed in this well. The in-situ stress and the resulting wellbore failures are then estimated based on the selected wellbore failures data. Finally, I wrote the manuscript.

### **Study 3: Characterization of the mechanical heterogeneity and their role in induced seismicity in Soultz-sous-Forêts fractured crystalline reservoir**

Citation:

Sahara, D., C. Meller, E. Gaucher, M. Schoenball, Y. Nusiaputra, and T. Kohl (in preparation), Characterization of the mechanical heterogeneity and their role in induced seismicity in Soultz-sous-Forêts fractured crystalline reservoir

The study was carried within the portfolio GEOENERGIE of the Helmholtz Association of German Research Centres and was funded by Energie Baden-Wuerttemberg (EnBW). The purposes of this study were to improve the reservoir characterization from an integrated borehole analysis. The results of the previous works in the same field is used as input data: borehole breakout from *Sahara et al.* [2014], clay content from *Meller et al.* [2014], lithology from *Hooijkaas et al.* [2006] and *Meller et al.* [2014], induced seismicity from *Dyer* [2005]. In this study, I developed the clustering technique based on neural-network concept to identify the reservoir zonation. Finally, I wrote the manuscript

### **Study 4: Analysis of borehole breakout development using continuum damage mechanics**

Citation:

Sahara, D., M. Schoenball, E. Gerolymatou, and T. Kohl (submitted), Analysis of borehole breakout development using continuum damage mechanics, *International Journal of Rock Mechanics and Mining Sciences*.

The study was carried within the portfolio GEOENERGIE of the Helmholtz Association of German Research Centres and was funded by Energie Baden-Wuerttemberg (EnBW). The purposes of this study were to achieve a better understanding of the development of breakouts in a complex material and to be able to reproduce the main features of wellbore failures observed from the laboratory measurement, e.g. *Haimson and Lee* [2004]. In this study, I developed the code for the numerical modeling using the Continuum Damage Mechanics (CDM) concept. The plastic law of Berea sandstone obtained by *Busetti et al.* [2012] was used in this study. I performed the numerical stimulation and interpreted the stages of the breakout development. Finally, I wrote the manuscript.

# Author

## Personal information

Name David Prambudi Sahara  
Nationality Indonesian  
Date of Birth 07.03.1987 in Trenggalek

## Education

12/2012 - 06/2016 PhD at Karlsruhe Institute of Technology (KIT), Germany  
Studies In Div. of Geothermal Research, Institute of Applied Geosciences  
Thesis: Significance of mechanical behavior and stress heterogeneity in a deep geothermal reservoir

01/2010 - 07/2011 Master at Institut Teknologi Bandung (ITB), Indonesia  
Studies in Geophysics with specification in Seismology  
Thesis: Understanding the mechanism of subduction process and its implication to surface seismicity and volcanic activity in Central Java - Indonesia from high resolution tomography

08/2005 - 10/2009 Bachelor at Institut Teknologi Bandung (ITB), Indonesia  
Studies in Geophysics with specification in Applied geophysics  
Thesis: The development of a high-resolution hypocenter relocation software using the double difference technique

## Declaration in lieu of oath

I herewith declare in lieu of oath that I have composed this thesis without any inadmissible help of a third party and without the use of aids other than those listed. The data and concepts that have been taken directly or indirectly from other sources have been acknowledged and referenced.

I further declare that I have followed the rules for ensuring proper scientific practice at the Karlsruhe Institute of Technology (KIT), passed on December 12<sup>th</sup>, 2012 by the executive committee of KIT.

This thesis has not been submitted, wholly or substantially, neither in this country nor abroad for another degree at any university or institute.

I have said nothing but the truth to the best of my knowledge, and I have not withheld any information.

Karlsruhe, April 13<sup>th</sup>, 2016

David Prambudi Sahara